

**NASA
Technical
Paper
2118**

**AVRADCOM
Technical
Report
82-A-15**

January 1983

The Vibration Characteristics of a Coupled Helicopter Rotor-Fuselage by a Finite Element Analysis

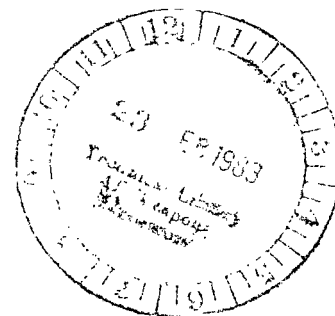
Michael J. Rutkowski

LOAN COPY: RETURN TO
AFWL TECHNICAL LIBRARY
KIRTLAND AFB, N.M.



NASA

NASA
TP
2118
c.1



**NASA
Technical
Paper
2118**

**AVRADCOM
Technical
Report
82-A-15**

1983

TECH LIBRARY KAFB, NM



0134994

The Vibration Characteristics of a Coupled Helicopter Rotor-Fuselage by a Finite Element Analysis

Michael J. Rutkowski
*Aeromechanics Laboratory
AVRADCOM Research and Technology Laboratories
Ames Research Center
Moffett Field, California*



National Aeronautics
and Space Administration

Scientific and Technical
Information Branch

CONTENTS

	<u>Page</u>
SYMBOLS	v
SUMMARY	1
INTRODUCTION	1
MATHEMATICAL MODEL	3
RESULTS AND DISCUSSION	3
Eigenanalyses	4
Coupled Rotor-Fuselage Response	7
Responses at n per Rev	8
Approximate Uncoupled Response	10
CONCLUDING REMARKS	11
APPENDIX A — DERIVATION OF ELEMENT MATRICES	13
APPENDIX B — ELEMENT MATRICES	16
APPENDIX C — EQUATIONS OF MOTION	20
REFERENCES	23

SYMBOLS

a	airfoil lift curve slope, 2π per radian
$[a]$	matrix relating w to $\{q\}$, equation (A2)
B_1, B_2, B_3	collective blade modes
b	number of blades
$[C]$	aerodynamic damping matrix
$[\bar{C}]$	modal aerodynamic damping matrix, equation (C10)
c	blade chord, m
$[c]$	element aerodynamic damping matrix, equations (A20) and (B4)
EI	bending stiffness, equation (A11), $N \cdot m^2$
$(EI)_i$	element bending stiffness polynomial coefficients, $i = 0, 1, 2, 3$, equation (A11), $N \cdot m^2$
$F = F_0 \sin \omega t$	uniformly distributed harmonic load, N
F_R	hub reaction force, N
F_1, F_2, F_3	symmetric fuselage modes
g	structural damping coefficient
$[I]$	identity matrix
i	$(-1)^{1/2}$
$[K]$	stiffness matrix
$[K_C]$	centrifugal stiffness matrix
$[K_E]$	elastic stiffness matrix
k	spring constant, N/m
$[k_C]$	element centrifugal stiffness matrix, equations (A16) and (B3)
$[k_E]$	element elastic stiffness matrix, equations (A8) and (B2)
L	aerodynamic lift per unit length, equation (A17), N/m
ℓ	blade element length, m
$[M]$	mass matrix
m	element mass per unit length, equation (A10), kg/m

$[m]$	element mass matrix, equations (A9) and (B1)
m_i	element mass polynomial coefficients, $i = 0,1,2,3$, equation (A10), kg/m
P	per revolution
$\{P\} = \{P_o\}e^{i\omega t}$	nodal load vector
$\{\bar{P}\} = \{\bar{P}_o\}e^{i\omega t}$	modal load vector, equation (C13)
p	applied load distribution, N/m
$[p]$	element load matrix equations (A23) and (B5)
$\{q\} = \{q_o\}e^{i\omega t}$	nodal displacement vector
$\{\bar{q}\} = \{\bar{q}_o\}e^{i\omega t}$	modal displacement vector, equation (C14)
R	distance from center of rotation to blade tip, m
r	x distance from axis of rotation, m
T, T_o	centrifugal tension, equations (A13) and (A14), N
\mathcal{T}	kinetic energy, equation (A5), $\text{kg}\cdot\text{m}^2/\text{sec}^2$
t	time, sec
\mathcal{U}	bending strain energy, equation (A4), N·m
\mathcal{U}_c	centrifugal stiffness strain energy, equation (A15)
$[U]$	matrix of real orthogonal modes
w	displacement in the y direction, m
x, y	coordinate system, figure 1, m
$\delta\mathcal{W}$	virtual work of the applied aerodynamic load, equation (A18), N·m
$\delta\mathcal{W}_p$	virtual work of the applied sinusoidal load p, equation (A21), N·m
λ	real eigenvalue
ξ	x/ℓ
ρ_∞	air density, kg/m^3
Ω	rotor speed, rad/sec
ω	frequency, rad/sec
ω_A	antiresonant frequency, rad/sec

ω_n	modal frequency, rad/sec
$(\)'$	$\partial/\partial x$
$(\)^\cdot$	$\partial/\partial t$
$(\)_o$	amplitude of excitation or response
$[\]$	matrix
$[\]^T$	transpose of a matrix
$[\]$	diagonal square matrix
$\{ \}$	vector

THE VIBRATION CHARACTERISTICS OF A COUPLED HELICOPTER
ROTOR-FUSELAGE BY A FINITE ELEMENT ANALYSIS

Michael J. Rutkowski

Ames Research Center
and
Aeromechanics Laboratory

AVRADCOM Research and Technology Laboratories

SUMMARY

The dynamic coupling between the rotor system and the fuselage of a simplified helicopter model in hover is analytically investigated. Mass, aerodynamic damping, and elastic and centrifugal stiffness matrices are presented for the analytical model; the model is based on a beam finite element, with polynomial mass and stiffness distributions for both the rotor and fuselage representations. For this analytical model, only symmetric fuselage and collective blade degrees of freedom are treated. Real and complex eigenanalyses are carried out to obtain coupled rotor-fuselage natural modes and frequencies as a function of rotor speed. Vibration response results are obtained for the coupled system subjected to a radially uniform, harmonic blade loading. The coupled response results are compared with response results from an uncoupled analysis in which hub loads for an isolated rotor system subjected to the same sinusoidal blade loading as the coupled system are applied to a free-free fuselage. It is shown that although the fuselage response as a function of forcing frequency and rotor speed is similar in the two cases, the responses resulting from the approximate, uncoupled analysis are significantly greater than those resulting from the coupled analysis. Thus, it is necessary to carry out a coupled rotor-fuselage analysis in order to accurately predict the fuselage vibration response.

INTRODUCTION

Vibration is a serious problem in military and civilian helicopters. It causes structural fatigue and failure, increases maintenance and operational costs, impairs performance, and has important human factor implications. Surprisingly, however, vibration reduction efforts during the original design of most helicopters are not significant. Too often it remains for later and costly flight-test programs to identify vibration problems and to suggest fixes — for example, the addition of vibration absorbers or, if necessary, even structural modifications. In addition to the costs they impose, these ad hoc fixes usually carry with them a weight penalty that reduces either payload or range or both.

There are many sources of vibration excitation in a helicopter — for example, engine and gearbox vibratory forces, tail-rotor excitation, rotor mass imbalance, and rotor wake impingement — but main-rotor excitation is usually the most significant. This excitation results from a combination of phenomena such as hover or forward flight aerodynamics, rotor inflow, hub motion, blade dynamics, and coupled rotor-fuselage dynamics. Unfortunately, the complete helicopter vibration problem is

virtually impossible to predict, as yet, because of its structural, as well as aerodynamic, complexity.

To make the helicopter vibration problem more tractable, simplifying assumptions must be made. Typically, the rotor system and the fuselage are analyzed separately and then attempts are made to account for rotor-fuselage coupling. First, hub forces and moments are obtained for an isolated elastic rotor rigidly supported at the hub and subjected to aerodynamic loads. The hub loads are then applied to a flexible fuselage, such as a NASTRAN finite element model, and responses are then calculated at different points on the fuselage. This procedure is a questionable one, however, because it does not account for rotor-fuselage coupling. In reference 1, it is noted that even introducing an equivalent rotor mass, although it gives a somewhat better approximation, still does not adequately represent the coupled rotor-fuselage system. Thus, there appears to be no viable alternative to carrying out a coupled rotor-fuselage analysis when one is investigating fuselage response to rotor excitation.

Recently, several coupled rotor-fuselage analyses were carried out using simple mathematical models in order to gain insight into the physics of the coupled vibration problem (refs. 1-4). In reference 1, a coupled rotor-airframe analysis based on an impedance matching method is described. This analysis is then applied to a simple, single-rotor example and to predicting vibration in the Model 347 helicopter. The role of rotor impedance in rotorcraft vibration is assessed in reference 2 by Hohenemser and Yin. In particular, they show that the usual approximation whereby dynamic forces and moments for a rigidly supported isolated rotor are applied to a flexible airframe can lead to large errors in vibration predictions. In their improved method, Hohenemser and Yin use the rotor impedance to correct the dynamic rotor force and moment inputs to the airframe. This work was extended by Hsu and Peters (ref. 3) who performed a coupled rotor-airframe analysis using harmonic balance by matching fuselage impedance with rotor impedances (flapping only) calculated for a wide range of rotor parameters. The results of these analyses show that hub motions have their greatest effect on the hub loads of relatively stiff rotors. A harmonic balance solution was also used by Kunz (ref. 4) in a fully coupled rotorcraft vibration analysis which showed the significant effects of rotor-body coupling upon hub pitching moment.

The objective of the present work is to extend the previous analyses (refs. 1-4) by carrying out a qualitative examination of both the basic rotor-fuselage coupling mechanism and the effect of this dynamic coupling on fuselage response. This report presents the results of an investigation into the dynamic coupling between the rotor system and the fuselage of a simplified beam-model helicopter. The rotor-fuselage model used in this analysis is based on a two-degree-of-freedom (transverse deflection and rotation) beam finite element with polynomial mass and stiffness properties. Both real and complex eigenanalyses are carried out to obtain the symmetric fuselage modes and the blade collective modes as a function of rotor speed. Mode shapes, as well as modal frequencies, are obtained in both the real and complex analyses. In the complex eigenanalyses, damping for the rotor in hover is introduced using quasi-steady strip-theory aerodynamics. In addition to these eigenanalyses, this report also describes forced response vibration results for the case of a radially uniform, harmonic load applied to the rotor. Results from coupled, as well as uncoupled, rotor-fuselage response analyses are presented and compared to demonstrate the importance of dynamic coupling. These results are presented in several different formats including two- and three-dimensional plots and contour plots.

Because of the relative simplicity of the model used in these analyses, the present work considers only symmetric motion of the rotor and fuselage. Nonetheless, there is still a great deal that can be learned from the results of these analyses. The model's simplicity allows one to easily generate responses at any node point for a large number of forcing frequencies at many rotor speeds.

MATHEMATICAL MODEL

The basic structural element used to model the rotor and the fuselage in this analysis is the beam-bending finite element, as described in reference 5. For simplicity, this element (fig. 1), which is based on a cubic polynomial displacement function, includes transverse displacements and rotations in one plane only. The element mass, damping, and stiffness matrices used in this analysis are derived in appendix A and presented in appendix B. The usual uniform elastic stiffness and consistent mass matrices have been extended to allow for up to a cubic polynomial variation in both the element mass and stiffness properties. In addition, the rotor-blade elements also include centrifugal stiffness matrices and aerodynamic damping matrices based on quasi-steady strip theory. Both of these blade element matrices vary with rotor speed. Structural damping is included in both the rotor and the fuselage elements.

Because of the relative simplicity of the beam finite element used to model the rotor and fuselage, the present investigation considers only the rotor-induced vertical shear loads that are transmitted to the fuselage. The longitudinal and lateral forces, which cause pitching and rolling in an actual helicopter, are not included here. Therefore, this coupled analysis is restricted to symmetric loadings and model configurations so that only the collective rotor modes and symmetric fuselage bending modes are excited.

The equations of motion for the real and complex eigenanalyses and the forced-response analyses are given in appendix C. In the forced-response analyses, in addition to the aerodynamic loading, the rotor system is subjected to a distributed harmonic load. Although in the present analysis a radially uniform load was considered, a load distribution that varies linearly or quadratically with blade span, as well as one or more point-loads applied to the rotor or the fuselage or both, could be considered. The present investigation can readily be extended to a study of the sensitivity of coupled rotor-fuselage vibrations to small variations in geometric, inertial, and stiffness parameters. In addition, natural antiresonances, as well as the effect of introducing an isolator between the rotor and the fuselage, could also be investigated.

The rotating beam mathematical model used in this analysis has been validated for an isolated rotor blade in reference 6. Real eigenvalue and eigenvector results obtained using the beam element and a cubic polynomial displacement function were compared with the nearly exact results obtained using a higher-order finite element for several rotating beam examples.

RESULTS AND DISCUSSION

The beam model representation of the basic configuration used in this coupled rotor-fuselage analysis is shown in figure 2. This model consists of a hingeless

rotor — made up of two 5-element rotating beams cantilevered in bending to a lumped mass hub — connected by a linear spring to the midpoint of a 10-element fuselage. A 5-element representation of the blades was chosen because it has been shown to give frequencies within 1% of the exact values for the first three rotating modes (ref. 6). Figure 2 also shows the location of the rotor and fuselage node points for the present configuration. The blades are each 7.62 m (25.0 ft) long with uniform mass and stiffness distributions of 14.17 kg/m (0.30 slugs/ft) and $82,600 \text{ N}\cdot\text{m}^2$ ($200,000 \text{ lb}\cdot\text{ft}^2$), respectively, and the concentrated hub has a mass of 233.5 kg (16.0 slugs). In the present configuration the connection between the rotor and the fuselage is assumed to be essentially rigid, and, therefore, the connecting spring has a relatively high spring constant, k , of $1.46 \times 10^{11} \text{ N/m}$ ($1.00 \times 10^{10} \text{ lb/ft}$). The flexible fuselage is 12.2 m (40.0 ft) long with the nonuniform, but symmetric, mass and stiffness distributions shown in figures 3 and 4, respectively. These mass, stiffness, and geometric properties were chosen to demonstrate some of the dynamic coupling characteristics of coupled rotor-fuselage systems and still to give frequency placements that are representative of typical helicopters having a nominal operating rotor speed of $\Omega = 30 \text{ rad/sec}$. In addition, a reasonably typical rotor-plus-hub mass to fuselage mass ratio of 0.11 was chosen. Finally, in the response analyses, in addition to the aerodynamic damping in the blades, structural damping of 6% has been assumed throughout the rotor-fuselage in order to reduce the magnitudes of the resonance peaks in the response plots.

Eigenanalyses

Natural frequencies— The uncoupled and coupled modal frequencies as a function of rotor speed are presented in figure 5(a) for the rotor and fuselage without structural or aerodynamic damping. Also shown in the figure are the (dotted) nP lines ($n = 1, 2, 3, 4$) where the modal frequency is equal to the rotor speed or one of its harmonics. The boundary conditions for the uncoupled systems were taken to be free-free for the fuselage and hub-fixed for the rotor, since these boundary conditions most closely approximate the actual boundary conditions of each component in the coupled system for the typical rotor-mass/fuselage-mass ratio considered. For the uncoupled free-free fuselage, figure 5(a) shows the two symmetric bending frequencies (F_1 and F_2) to be independent of rotor speed. The uncoupled, collective flap rotor modes (B_1 , B_2 , and B_3), on the other hand, increases in frequency as rotor speed is increased and, consequently, as centrifugal stiffening is increased. Furthermore, when the fuselage and rotor are uncoupled, the curves of rotor flap and fuselage bending frequencies are seen to cross as the flap stiffness increases. Similar frequencies are obtained for the coupled rotor-fuselage system except where the rotor and fuselage couple. When the fuselage and rotor are elastically coupled, the frequencies are close to their uncoupled values only when the frequencies are widely separated. When a region where the uncoupled frequencies cross is approached, the frequency curves for the coupled modes begin to diverge and approach the frequency curves of the companion modes. In the present paper this region of modal coupling is referred to as a region of modal coalescence. Here, for the *in vacuo* case, figure 5(a) shows that the uncoupled frequencies are poor approximations to the actual coupled frequencies, especially near where the second fuselage-bending mode couples with the second rotor flap mode.

The effect of rotor aerodynamic damping on the uncoupled rotor and the coupled rotor-fuselage system frequencies is shown in figure 5(b). Except for the reduction of the first rotor-flap-mode frequency from above 1P to below 1P, rotor aerodynamic damping does not have an appreciable effect on the uncoupled rotor modes. For the coupled rotor-fuselage system, however, the addition of aerodynamic damping results

in a significant change in the shape of the curves in the region of the rotor-fuselage mode frequency crossings. Figure 5(c) shows that in the presence of aerodynamics, the effect of rotor-fuselage coupling is less than it is in the *in vacuo* case. Therefore, with rotor aerodynamic damping included, the uncoupled rotor and fuselage frequencies are a somewhat better approximation to the coupled system frequencies.

Mode shapes— Mode-shape plots are presented to better illustrate the phenomenon of modal coupling and, in particular, to show what happens when rotor and fuselage modes couple. In addition, mode-shape plots are useful in showing the often overlooked effects of aerodynamic damping and out-of-phase modal content on coupling.

In any discussion of mode shapes one inevitably faces the problem of how to name or label different modes that couple and "cross" on the frequency-versus-rotor-speed plot. Some liberties must be taken at times, since at modal crossings individual mode identities may become lost or ambiguous. For example, modes could be labeled to represent the order of value of mode natural frequencies, that is, mode 1, mode 2, etc. For a given "physical mode," however, such a mode number changes at frequency coalescences; for example, the "first rotor-flap mode" starts off as mode 1 at low rotor speed and switches to mode 2 at high rotor speed. In this report, modes will be referred to by their dominant physical characteristic.

The eigenvectors for the first two rotor collective flap modes are shown in figures 6(a) and 6(b), and the first two fuselage symmetric bending modes are shown in figures 6(c) and 6(d). The mode shapes for these four modes are presented for each of three conditions: (1) either an uncoupled hub-fixed rotor *in vacuo* or an uncoupled free-free fuselage; (2) coupled rotor-fuselage *in vacuo*; and (3) coupled rotor-fuselage with rotor aerodynamic damping included. The mode shapes for each case, except the two uncoupled fuselage modes, which are independent of rotor speed, are presented for a range of rotor speeds. For the coupled rotor-fuselage system with aerodynamic damping included, both the real and imaginary parts of the complex mode shapes are plotted for rotor speeds from 0 to 60 rad/sec. In most cases the imaginary parts of the mode shapes, which come entirely from aerodynamic and structural damping, are small; as a result, the mode shapes are essentially real and differ only slightly from the mode shapes that were obtained from a real eigenanalysis with damping neglected.

Consider first the modes of the isolated rotor blade that are shown in figures 6(a) and 6(b). Of these two uncoupled modes, which change somewhat with rotor speed, the change in the first rotor mode shape as rotor speed increases is most apparent (fig. 6(a)). Initially, at zero rotor speed, the mode shape of each blade is that of a uniform cantilever beam. Then, as rotor speed increases, the rotor-blade stiffness increases because of increased centrifugal forces, and the blade mode shape approaches a straight line. Similarly, the second uncoupled rotor mode also tends to flatten out as rotor speed is increased (fig. 6(b)).

The first two symmetric bending modes for the uncoupled free-free fuselage are shown in figures 6(c) and 6(d). These modes do not change shape as rotor speed increases, since the uncoupled fuselage modes are independent of rotor speed.

Now we will trace the changes in these four basic modes (first rotor-flap, second rotor-flap, first fuselage-bending, and second fuselage-bending) as they are manifested in the coupled system. Usually their identity is evident, but when modes coalesce their separate identities are often lost. The effect of rotor-fuselage coupling on the rotor-flap mode shapes is small. For the coupled rotor-fuselage

configuration in figures 6(a) and 6(b), both with and without aerodynamic damping included, the rotor deflections are nearly the same as for the uncoupled rotor-blade modes. At the same time, the fuselage deflections for these rotor modes are very small, except at rotor speeds at which there is a coalescence of a rotor mode with a fuselage mode. The rotor modes do not exhibit much fuselage motion, because the mass of the fuselage plus the concentrated hub mass is much larger than the mass of the rotor blades. (In this case the mass ratio is 20:1.) In addition, the hub motion is usually negligible; this justifies the conventional uncoupled approximation to the coupled rotor-fuselage system whereby hub forces and moments, which are obtained for an isolated elastic rotor rigidly supported at the hub, are applied to a flexible fuselage. In contrast, the fuselage modes (figs. 6(c) and 6(d)) generally produce a large hub motion which in turn "excites" large rotor deflections in fuselage modes.

Of particular interest is the behavior of the coupled rotor-fuselage configuration near $\Omega = 30$ rad/sec, where the second fuselage bending mode is highly coupled with the second rotor-flapping mode. The *in vacuo* mode shapes at $\Omega = 30$ rad/sec for these two modes (figs. 6(b) and 6(d)) look very similar except that the fuselage deflections are 180° out of phase. Both of these real modes contain fuselage-bending and rotor-flapping deflections. The mode shapes in air for these two modes, on the other hand, are very different from each other. This difference shows up in the complex eigenvectors. In figure 6(b), for second rotor-flap mode in air, the real part of the modal deflections contains only second rotor-flapping, and the imaginary mode shape contains a very small amount of both rotor and fuselage deflections. In figure 6(d), for the second symmetric fuselage-bending mode in air, however, the real part of the complex mode shape is predominantly second fuselage-bending, and the imaginary mode shape shows a very significant amount of second rotor-flapping.

To better focus on the details in the $\Omega = 30$ rad/sec region of high rotor-fuselage coupling previously seen in the frequency plot of figure 5(c), mode shapes for rotor speeds of 24-36 rad/sec are presented in figures 7(a) and 7(b). These figures show the changes that occur in the coupled rotor-fuselage second rotor- and second fuselage-mode shapes, respectively, in the vicinity of their coalescence. In figure 7(a), the fuselage deflections for the second rotor mode *in vacuo* are seen to first increase as the rotor speed is increased to 30 rad/sec and then to decrease with opposite phase as the rotor speed is increased further. In air, both the real fuselage deflections and all of the imaginary deflections are small. This implies that for the rotor-flapping and fuselage-bending modes considered here, rotor aerodynamic damping suppresses the effects of rotor-body dynamic coupling. In figure 7(b), however, for the second fuselage mode *in vacuo*, the rotor deflections first increase and the fuselage deflections decrease as rotor speed is increased to approximately 30 rad/sec. Then the rotor deflections change phase and decrease with further increase in rotor speed while the fuselage deflections increase. Again, the in-air deflections are considerably different. They show a gradual change in the real part of the rotor mode shape from second mode to first mode of opposite phase, while the imaginary part of the rotor deflections first increases and then decreases. A similar type of behavior occurs for the coalescence of the first rotor-blade flap mode with the first fuselage-bending mode. The *in vacuo* and in-air mode shapes for these two modes are shown in figures 7(c) and 7(d). Again, as in the previous instance, the *in vacuo* and in-air shapes are considerably different near the coalescence.

As has just been seen, in following a mode for increasing rotor speed there can be a significant difference in behavior between the *in vacuo* and the in-air cases, especially near a coalescence. In figure 8 are shown the uncoupled, coupled *in vacuo*, and coupled in-air eigenvalues as a function of rotor speed for the two modes presented in figures 7(a) and 7(b). The second fuselage-mode eigenvalues for the coupled

in-air case are seen to fall roughly midway between those for the free-free fuselage alone and for a free-free fuselage with an effective rotor mass that is an approximation sometimes used to account for rotor-airframe interaction (ref. 1). Similarly, the second rotor-mode eigenvalues for the coupled in-air case roughly agree with those for an isolated rotor both with and without aerodynamic damping included. The two *in vacuo* modes, however, behave quite differently. Initially, the lower frequency mode is a predominantly second rotor-flap mode and the higher-frequency mode is mostly a second fuselage bending along with a little second blade-flap mode. Then, above a rotor speed of about 30 rad/sec, the two modes exchange behavior so that the first becomes fuselage bending and the second becomes blade flapping. In contrast, for the coupled rotor-fuselage in-air modes (as for the uncoupled modes), a mode that begins as a fuselage-bending mode or as a blade-flapping mode retains its basic character as rotor speed is increased, even through a coalescence.

Coupled Rotor-Fuselage Response

The vibration response of the coupled rotor-fuselage system in air was investigated by introducing an arbitrary, uniformly distributed harmonic load along the blades (fig. 9) and then determining the response at selected node points on the fuselage. It should be noted that the frequency of this loading is not an integer multiple of $b\Omega$ as it is for a b -bladed rotor rotating at Ω . Rather, in order to study the dynamic coupling between the rotor and fuselage, all frequencies from 0 to 120 rad/sec for all rotor speeds from 0 to 60 rad/sec have been considered. The absolute magnitude of the acceleration response, in g's, at the center of the fuselage (node 17) owing to a 4,448-N (1,000-lb) harmonic load uniformly distributed along the rotor blades is presented as a function of both forcing frequency and rotor speed in the 3-D plot of figure 10(a). These same responses are also presented in figure 10(b) as a contour map of constant vibration amplitude superimposed on the coupled rotor-fuselage eigenvalues and nP excitation frequency lines from figure 5(c). Figures 10(a) and 10(b) show that the system has resonant responses at the two lightly damped fuselage-bending-mode frequencies (at about 25 and 80 Hz). Of particular interest is the sensitivity of this vibration response to rotor speed near the first and second fuselage-bending-mode frequencies. The dynamic coupling between the rotor and fuselage modes produces "valleys" in the response topography. The acceleration response at the rotor modal frequencies, however, is only significant at low rotor speeds, since aerodynamic damping, which increases with rotor speed, suppresses the response of the blades and, hence, the fuselage. On the other hand, if aerodynamic damping were to be neglected, a considerably different 3-D response plot from that of figure 10(a) would be obtained (fig. 11). In this case, the system response at the rotor-mode frequencies is not attenuated with increased rotor speed as it is in the aerodynamically damped case. The effects of coupled rotor-fuselage dynamics, however, are still very much evident.

The maximum system responses shown in figure 10(a) can be confirmed to coincide closely with the coupling of the fuselage- and rotor-mode frequencies by referring to the contour-eigenvalue plot in figure 10(b). The minimum response of the second fuselage mode occurs at a rotor speed that is roughly equidistant from the rotor speeds at which the second and third flap modes coalesce with the second fuselage mode.

If the dynamic coupling between the rotor and fuselage modes were neglected, the response would differ greatly from that shown in figure 10(a). Figure 12 shows the acceleration response at node 17 for a 4,448-N (1,000-lb) oscillating point-load applied at the midpoint of an isolated free-free fuselage. Here the response is seen

to vary with forcing frequency ω but, of course, it does not vary with rotor speed. In figure 13, the peak responses of this uncoupled fuselage are seen to occur at the two uncoupled fuselage symmetric bending-mode frequencies, 25.8 and 83.4 rad/sec. Besides these two frequencies at which resonance occurs, there are two other frequencies worth noting in figure 13: 22.3 and 61.0 rad/sec. At these two frequencies the response at node 17 is nearly zero. (If structural damping had not been introduced into the problem the response would be exactly zero.) These frequencies are the first two natural antiresonant frequencies for node 17 for forcing at node 17. Natural antiresonances, which occur in structures much as resonances do (ref. 7), are a function of fuselage location, as well as frequency (fig. 14). It is interesting to note that the fuselage antiresonant lines in figure 14 represent both the uncoupled fuselage forced at its center (node 17) and the coupled rotor-fuselage with forces applied to the rotor which is connected to the fuselage at node 17. Although antiresonant theory is not considered directly in the present paper, it is important as a possible means of reducing forced vibratory response in helicopters.

The fuselage nodal responses presented herein represent the absolute magnitude of what is a complex response. For completeness, the real and imaginary parts of the complex response at nodes 14 and 17 are presented in figures 15(a)-15(d) for the coupled rotor-fuselage in air.

The response plots presented above are for only one particular fuselage node point. Since the fuselage is a flexible structure, the response at other fuselage node points can be expected to be different. Figures 16(a)-16(f) are included to show the variation of the fuselage vibration response from the fuselage tip (node 12) to the center of the fuselage (node 17) for the coupled rotor-fuselage system subjected to a 4,448-N (1,000-lb), radially uniform, harmonic load applied to the rotor. The response is seen to be strongly dependent on the fuselage nodal location. Nodes 12, 14, and 17 are responsive in decreasing magnitude in both fuselage bending modes, and nodes 13 and 15 are only responsive in the first and second fuselage-bending modes, respectively; node 16 is not very responsive in either mode. These modal response results coincide directly with the nodal displacements of the first two fuselage mode shapes (figs. 6(c) and 6(d)).

Responses at n per Rev

It is recognized that in an actual rotorcraft the periodic aerodynamic forces generated in forward flight by a rotor with b blades produce fuselage vibratory responses only at $nb\Omega$ (where $n = 1, 2, 3, \dots$) since only $nb\Omega$ shears are transmitted from the rotor to the fuselage for a b -bladed rotor. Although response calculations have been carried out for all combinations of forcing frequency and rotor speed, the resonant responses of the system can only occur along the $nP = nb\Omega$ "per-rev" lines on the eigenvalue plots of figures 5(a)-5(c). Thus, for a two-bladed rotor only the response along the $2P$ and $4P$ lines are meaningful, while for a three- or four-bladed rotor only the $3P$ and $4P$ lines, respectively, have meaning. The higher values of nP are not included here, because the responses diminish rapidly as P increases.

The nP response plot for the coupled rotor-fuselage response at node 17 presented previously (fig. 10(b)) is shown in figure 17. In general, the nP response peaks occur when the nP lines in figure 10(b) cross a fuselage or blade modal frequency. In figure 17, the rotor speeds at which the nP lines cross the first and second blade-mode frequencies and the first, second, and third fuselage-mode frequencies are labeled B_1 , B_2 , F_1 , F_2 , and F_3 , respectively. The largest $2P$ response

peak is seen to occur at a rotor speed of about 40 rad/sec where the 2P excitation frequency coincides with the second fuselage-bending-mode frequency (F_2) of 80.7 rad/sec. There are instances, however, where there is no resonant response peak, even though an nP line crosses a natural frequency of the system. For example, the 3P line crosses the second blade-mode frequency (B_2) at approximately 18 rad/sec (fig. 10(b)), but figure 17 shows no 3P response peak at this rotor speed. In fact, the 3P response is very low at this rotor speed. This is due in part to rotor aerodynamic damping but is mostly a result of the fact that the B_2 mode frequency is well separated from the F_1 and F_2 mode frequencies at this rotor speed (see fig. 9(b)). The same is also true where the 1P line crosses the first blade-mode frequency (B_1).

Figure 17 also shows how the proximity to a coalescence affects the nP response. The 2P and 3P resonant responses at the second fuselage frequency (F_2), which are near the F_2 mode frequency's coalescence with the second blade mode, are considerably larger than the 4P response at the F_2 mode frequency, which is well separated from the coalescences of the F_2 mode with the second and third blade modes, respectively. In fact, referring back to the contour plots of figure 10(b), the 4P line is seen to intersect the second fuselage-bending mode right in a "valley" between the two response peaks. The 2P and 3P lines, on the other hand, intersect the second fuselage mode line high up on the sides of the response "mountain."

All of the response analyses presented in this paper are for an assumed 6% structural damping which was introduced to reduce the magnitude of the resonant peaks of the response plots. In order to assess the effect of structural damping on the coupled rotor-fuselage response, additional response analyses were carried out with 2% and 10% structural damping. Figure 18 presents direct comparisons of the coupled nP responses at node 17 for 2%, 6% (fig. 17), and 10% structural damping. The figure shows the significant effect structural damping has on the resonant response peaks that occur at the fuselage natural frequencies.

In summary, although conventional wisdom says that one should avoid all situations in which any system natural frequency is near to or coalesces with an excitation frequency (because very high resonant responses can occur), the present results show that sometimes these situations may not be a problem at all. Figure 19 presents a qualitative representation of regions of low, high, and very high coupled rotor-fuselage response at system natural frequencies for node 17. As indicated in the figure, an excitation at a point where two system frequencies (i.e., fuselage and rotor) coalesce will produce very high vibration response, but if a rotor (or fuselage) mode frequency lies between two fuselage (or rotor) mode frequencies, then the effect of an excitation at that point may be substantially attenuated. Furthermore, whereas resonant excitation at fuselage-mode natural frequencies has, in general, a large effect on fuselage vibration response, the opposite is seen to be true for resonant excitation at blade-mode natural frequencies. Except for low rotor speeds, where there is little aerodynamic damping, and near the coalescence of two modes, resonant excitation at blade-mode natural frequencies does not lead to large fuselage responses.

Since the coupled rotor-fuselage vibration responses were seen to vary from one fuselage node to another (figs. 16(a)-16(f)), it is to be expected that the nP responses at these nodes would also vary between nodes. Figure 20 presents the nP responses at node 14. The resonant nP response peaks for this node are seen to occur at the same frequencies as for node 17 (fig. 17), but the amplitudes of these responses vary considerably. In addition, the antiresonances, which, as noted earlier, vary from one node to another, occur at different frequencies.

The variation of the nP responses with fuselage location and rotor speed is shown in the 3-D plots of figures 21(a)-21(d). In each case, the largest response is at the ends of the fuselage, although the rotor speeds at which the maximum responses occur are different. It should be noted that these 3-D nP plots appear somewhat distorted because some of the data points in these figures have been obtained by linear interpolation and are plotted using straight lines. Also, these plots are of magnitudes only and do not correctly show the node points on the fuselage at which the response is zero.

Approximate Uncoupled Response

In the preceding discussion, the forced-response behavior of the coupled rotor-fuselage system, in hover, was obtained for a uniformly distributed harmonic load applied along the rotor blades. In practice, however, coupled rotor-fuselage systems have only recently begun to be considered in vibration analyses. Such systems have historically been approximated by separate uncoupled systems. Therefore, in order to explore the accuracy and influence of this approximation and to investigate the effect of dynamic coupling between the fuselage and rotor, response calculations were also carried out using the conventional uncoupled approximation for the coupled system. The physical elements of the exact and the approximate calculations are illustrated in figure 22. To clarify the process for the reader, figure 22 traces the analyses from applied force to hub shear to fuselage transfer function to vibration response. For the uncoupled case, the same uniform 4,448-N (1,000-lb) harmonic load previously applied to the rotor of the coupled system was applied to an isolated, hub-fixed rotor, and the resulting hub reaction forces (F_R) were calculated. Then in additional separate analyses, these rotor hub reactions were applied to the uncoupled, free-free fuselage, both with and without an effective rotor mass included. The effective rotor mass in these analyses was taken to be equal to the full rotor mass. The uncoupled case with an effective rotor mass is typical of the procedure that has been followed by the helicopter industry in an attempt to obtain a better approximation of the interaction between the rotor and fuselage (ref. 1).

In figure 22, the fuselage vibration response at node 17 for the coupled system is compared with the response obtained for the uncoupled system, both with and without rotor mass. The figure shows that although the qualitative behavior of the responses appears to be similar, the magnitude of the approximate, uncoupled results, both with and without rotor mass, are considerably larger than the "exact" fully coupled results. The addition of the rotor mass does, however, result in an improvement in both the magnitude of the response and the frequency at which the response occurs. This improvement occurs even though the transfer function for the uncoupled fuselage without rotor mass is identical to the "exact" transfer function for the coupled system; the approximate transfer function for the uncoupled fuselage with rotor mass is somewhat lower in both magnitude and frequency because of the increased mass.

The cause of the disparity between the coupled and the uncoupled responses is apparent when the hub reaction force for the isolated, hub-fixed rotor is compared with the hub shear for the coupled rotor-fuselage. Figure 22 shows that in the coupled case the presence of the fuselage results in a reduction of the hub shear at the forcing frequencies of the fuselage bending modes. For the uncoupled case, however, the fuselage modes do not contribute to the hub reaction force.

A direct comparison of the coupled and uncoupled responses at node 17 is shown in the nP response plots of figures 23(a)-23(d). Except for the 1P plot where the coupled response is the largest, the uncoupled cases consistently overpredict the

response of the system. For 2P, 3P, and 4P the uncoupled response without rotor mass is seen to be considerably greater than the uncoupled response with rotor mass which in turn is considerably greater than the coupled response.

This underprediction of the 1P response and overprediction of the 2P, 3P, and 4P responses for the uncoupled cases is shown directly in figures 24(a)-24(d) where the ratio of the approximate, uncoupled nP response to the exact, coupled nP response is plotted. It should be noted that since figures 24(a)-24(d) represent ratios of responses and not actual responses, they are applicable for any node point on the fuselage. These figures show, for example, that the peak 4P responses for the uncoupled system without rotor mass is almost 6 times greater than the 4P response for the coupled system.

In figures 25(a)-25(d), nP plots of the hub reaction force for the isolated, hub-fixed rotor and the hub shear for the coupled rotor-fuselage are presented. Except for the 1P hub shear, the isolated hub-fixed rotor nP reaction forces are seen to be in general considerably greater than the coupled rotor-fuselage nP hub shears. As noted above, the influence of the fuselage modes, although clearly evident for the coupled case, is absent in the uncoupled case. Finally, these approximate and exact nP hub shears are compared directly in figures 26(a)-26(d) where the ratio of the isolated hub-fixed rotor reaction force to the coupled rotor-fuselage hub shear is plotted.

CONCLUDING REMARKS

In this report the dynamic coupling between the rotor and the fuselage of an analytical helicopter model in hover was investigated using a simplified beam finite element model. Eigenanalyses, as well as forced-response analyses, were carried out for both coupled and uncoupled rotor-fuselage configurations. The results for a particular beam-model representation of a rotorcraft may be summarized as follows:

1. The uncoupled rotor-fuselage frequencies *in vacuo* are poor approximations to the actual coupled frequencies near rotor-fuselage frequency coalescences. With rotor aerodynamic damping included, the uncoupled rotor-fuselage modes are better, but still not good, approximations to the coupled system complex modes.
2. The magnitude of the resonant response at the fuselage-mode frequencies is highly dependent on their proximity to the blade modal frequencies. When the rotor blade and fuselage frequencies coalesce, vibration is greatly increased (relatively), whereas away from such coalescences resonant response at the fuselage-mode frequencies may be of significantly lower magnitude.
3. Away from fuselage-mode frequencies, resonant excitation at blade-mode natural frequencies has a fairly small and often negligible effect on fuselage vibration response because of both dynamics and aerodynamic damping. Thus, it is not always necessary to avoid the coalescence of a system natural frequency with an excitation frequency.

4. For a radially uniform, harmonic blade loading, the approximate vibration responses obtained from applying the isolated blade hub shears to a free-free fuselage are considerably greater than those obtained when the coupled system is analyzed for the same blade loading.

Ames Research Center

National Aeronautics and Space Administration
and

Aeromechanics Laboratory

AVRADCOM Research and Technology Laboratories

Moffett Field, California 94035, August 27, 1982

APPENDIX A

DERIVATION OF ELEMENT MATRICES

For a beam finite element of length ℓ (fig. 1), the transverse displacement w is related to the modal displacements $\{q\}$ by

$$w = [a]\{q\} \quad (A1)$$

where

$$[a]^T = \begin{bmatrix} 1 - 3\xi^2 + 2\xi^3 \\ (\xi - 2\xi^2 + \xi^3)\ell \\ 3\xi^2 - 2\xi^3 \\ (-\xi^2 + \xi^3)\ell \end{bmatrix} \quad (A2)$$

and

$$\{q\} = \begin{Bmatrix} q_1 \\ q_2 \\ q_3 \\ q_4 \end{Bmatrix} \quad (A3)$$

For a nonrotating beam element undergoing transverse vibrations, the strain energy and kinetic energy are

$$\mathcal{U} = \int_0^\ell \frac{EI}{2} \left(\frac{\partial^2 w}{\partial x^2} \right)^2 dx \quad (A4)$$

$$\mathcal{F} = \int_0^\ell \frac{m}{2} (\dot{w})^2 dx \quad (A5)$$

Substituting equation (A1) into the total potential energy $\mathcal{U} - \mathcal{F}$ one obtains

$$\mathcal{U} - \mathcal{F} = \int_0^\ell \frac{EI}{2} \{q\}^T [a'']^T [a''] \{q\} dx - \int_0^\ell \frac{m}{2} \{\dot{q}\}^T [a]^T [a] \{\dot{q}\} dx \quad (A6)$$

$$= \frac{1}{2} \{q\}^T [k_E] \{q\} - \frac{1}{2} \{\dot{q}\}^T [m] \{\dot{q}\} \quad (A7)$$

where the element elastic stiffness matrix $[k_E]$ and the element mass matrix $[m]$ are given by

$$[k_E] = \int_0^\ell EI[a'']^T[a'']dx \quad (A8)$$

$$[m] = \int_0^\ell m[a]^T[a]dx \quad (A9)$$

In order to consider beams with nonuniform mass and stiffness properties, the present analysis allows the element mass and bending stiffness properties to be represented by polynomials of up to third order, that is,

$$m = m_0 + m_1\xi + m_2\xi^2 + m_3\xi^3 \quad (A10)$$

$$EI = (EI)_0 + (EI)_1\xi + (EI)_2\xi^2 + (EI)_3\xi^3 \quad (A11)$$

Substituting equations (A2) and (A10) into equation (A9) and equations (A2) and (A11) into equation (A8) and carrying out the indicated integrations over the element length yields the element mass and elastic stiffness matrices given in equations (B1) and (B2), respectively, of appendix B. Note that in addition to the distributed mass represented by equation (A9), the present analysis also allows concentrated masses to be placed at node points. These point masses are added to the appropriate element mass matrix diagonal location.

For a beam of length R rotating about a fixed axis with angular velocity Ω there is an increase in the beam's stiffness as a result of the centrifugal forces generated. The element strain energy due to this "centrifugal stiffness" is given by

$$\mathcal{U}_c = \frac{1}{2} \int_r^{r+\ell} T(x) \left(\frac{\partial w}{\partial x} \right)^2 dx \quad (A12)$$

where $T(x)$, the tension in the beam element of length ℓ at a distance r from the axis of rotation, is

$$T(x) = \int_r^{r+\ell} M\Omega^2 x dx + T_0 \quad (A13)$$

and where

$$T_0 = \int_{r+\ell}^R m\Omega^2 x dx \quad (A14)$$

is the tension due to mass radially outboard of the element of interest. Substituting equation (A1) into equation (A12) yields

$$\mathcal{U}_c = \frac{1}{2} \{q\}^T [k_c] \{q\} \quad (A15)$$

where the element centrifugal stiffness matrix $[k_c]$ can be calculated from

$$[k_c] = \int_r^{r+\ell} T(x) [a']^T [a'] dx \quad (A16)$$

Equation (A16) can be evaluated using equations (A2), (A10), and (A13) to obtain the centrifugal stiffness matrix given in equation (B3) of appendix B for an element with a cubic polynomial mass distribution.

The aerodynamic loads on the rotor blades of the present coupled rotor-fuselage system in hover are obtained from simplified quasi-steady strip theory. The blade lift per unit span is given by

$$L = -\frac{1}{2} \rho_\infty a c (\Omega r) (\dot{w}) \quad (A17)$$

For an element of the blade the virtual work of this applied aerodynamic load is

$$\delta \mathcal{W} = -\frac{1}{2} \rho_\infty a \Omega \int_0^\ell c(r+x) \dot{w} \delta w dx \quad (A18)$$

Then substituting equation (A1) into equation (A18) yields

$$\delta \mathcal{W} = -\{\dot{q}\}^T [c] \{\delta q\} \quad (A19)$$

where

$$[c] = \frac{1}{2} \rho_\infty a \Omega \int_0^\ell c(r+x) [a]^T [a] dx \quad (A20)$$

is the element aerodynamic damping matrix which is presented in equation (B4) of appendix B.

The virtual work of an applied harmonic load $p e^{i\omega t}$ is

$$\delta \mathcal{W}_p = \int_0^\ell p e^{i\omega t} \delta w dx \quad (A21)$$

Substituting equation (A1) into equation (A21) one obtains

$$\delta \mathcal{W}_p = [p] \{\delta q\} \quad (A22)$$

where the element load matrix $[p]$ is given by

$$[p] = \int_0^\ell p[a] dx e^{i\omega t} \quad (A23)$$

Equation (A23) is evaluated for a uniform sinusoidal load distribution ($p = p_0 = \text{constant}$) in equation (B5) of appendix B.

APPENDIX B

ELEMENT MATRICES

The element mass matrix is

$$[m] = \begin{bmatrix} m_{11} & & & \\ m_{21} & m_{22} & & \\ m_{31} & m_{32} & m_{33} & \\ m_{41} & m_{42} & m_{43} & m_{44} \end{bmatrix} \quad \text{symmetric} \quad (B1)$$

where

$$m_{11} = \frac{13}{35} m_0 + \frac{3}{35} m_1 + \frac{19}{630} m_2 + \frac{11}{840} m_3$$

$$m_{21} = \left(\frac{11}{210} m_0 + \frac{1}{60} m_1 + \frac{17}{2520} m_2 + \frac{1}{315} m_3 \right) \ell$$

$$m_{31} = \frac{9}{70} m_0 + \frac{9}{140} m_1 + \frac{23}{630} m_2 + \frac{19}{840} m_3$$

$$m_{41} = -\left(\frac{13}{420} m_0 + \frac{1}{70} m_1 + \frac{19}{2520} m_2 + \frac{11}{2520} m_3 \right) \ell$$

$$m_{22} = \left(\frac{1}{105} m_0 + \frac{1}{180} m_1 + \frac{1}{630} m_2 + \frac{1}{1260} m_3 \right) \ell^2$$

$$m_{32} = \left(\frac{13}{420} m_0 + \frac{1}{160} m_1 + \frac{5}{504} m_2 + \frac{2}{315} m_3 \right) \ell$$

$$m_{42} = -\left(\frac{1}{420} m_0 + \frac{1}{280} m_1 + \frac{1}{504} m_2 + \frac{1}{840} m_3 \right) \ell^2$$

$$m_{33} = \frac{13}{35} m_0 + \frac{2}{7} m_1 + \frac{29}{126} m_2 + \frac{23}{120} m_3$$

$$m_{43} = -\left(\frac{11}{210} m_0 + \frac{1}{28} m_1 + \frac{13}{504} m_2 + \frac{7}{360} m_3 \right) \ell$$

$$m_{44} = \left(\frac{1}{105} m_0 + \frac{1}{168} m_1 + \frac{1}{252} m_2 + \frac{1}{360} m_3 \right) \ell^2$$

The element elastic stiffness matrix is

$$[k_E] = \begin{bmatrix} k_{11} & & & \\ k_{21} & k_{22} & & \\ k_{31} & k_{32} & k_{33} & \\ k_{41} & k_{42} & k_{43} & k_{44} \end{bmatrix} \quad \text{symmetric} \quad (B2)$$

where

$$k_{11} = [12(EI)_0 + 6(EI)_1 + 4.8(EI)_2 + 4.2(EI)_3]/\ell^3$$

$$k_{21} = [6(EI)_0 + 2(EI)_1 + 1.4(EI)_2 + 1.2(EI)_3]/\ell^2$$

$$k_{31} = -k_{11}$$

$$k_{41} = [6(EI)_0 + 4(EI)_1 + 3.4(EI)_2 + 3(EI)_3]/\ell^2$$

$$k_{22} = [4(EI)_0 + (EI)_1 + (8/15)(EI)_2 + 4(EI)_3]/\ell$$

$$k_{32} = -k_{21}$$

$$k_{42} = [2(EI)_0 + (EI)_1 + (13/15)(EI)_2 + 8(EI)_3]/\ell$$

$$k_{33} = k_{11}$$

$$k_{43} = -k_{41}$$

$$k_{44} = [4(EI)_0 + 3(EI)_1 + (38/15)(EI)_2 + 2.2(EI)_3]/\ell$$

The element centrifugal stiffness matrix is

$$\begin{aligned} [k_C] = & \left\{ \frac{T_O}{\ell} + \ell\Omega^2 \left(\frac{1}{2} m_0 + \frac{1}{3} m_1 + \frac{1}{4} m_2 + \frac{1}{5} m_3 \right) + r\Omega^2 \left(m_0 + \frac{1}{2} m_1 + \frac{1}{3} m_2 + \frac{1}{4} m_3 \right) \right\} [k_{C_1}] \\ & - m_0 r \Omega^2 [k_{C_2}] - \frac{1}{2} (m_0 \ell + m_1 r) \Omega^2 [k_{C_3}] - \frac{1}{3} (m_1 \ell + m_2 r) \Omega^2 [k_{C_4}] \\ & - \frac{1}{4} (m_2 \ell + m_3 r) \Omega^2 [k_{C_5}] - \frac{1}{5} (m_3 \ell) \Omega^2 [k_{C_6}] \end{aligned} \quad (B3)$$

where

$$[k_{c_1}] = \begin{bmatrix} 6/5 & & & \\ \ell/10 & 2\ell^2/15 & & \text{symmetric} \\ -6/5 & -\ell/10 & 6/5 & \\ \ell/10 & -\ell^2/30 & -\ell/10 & 2\ell^2/15 \end{bmatrix}$$

$$[k_{c_2}] = \begin{bmatrix} 3/5 & & & \\ \ell/10 & \ell^2/30 & & \text{symmetric} \\ -3/5 & -\ell/10 & 3/5 & \\ 0 & -\ell^2/60 & 0 & \ell^2/10 \end{bmatrix}$$

$$[k_{c_3}] = \begin{bmatrix} 12/35 & & & \\ \ell/14 & 2\ell^2/105 & & \text{symmetric} \\ -12/35 & -\ell/14 & 12/35 & \\ -\ell/35 & -\ell^2/70 & \ell/35 & 3\ell^2/35 \end{bmatrix}$$

$$[k_{c_4}] = \begin{bmatrix} 3/14 & & & \\ \ell/20 & 11\ell^2/840 & & \text{symmetric} \\ -3/14 & -\ell/20 & 3/14 & \\ -\ell/28 & -11\ell^2/840 & \ell/28 & 13\ell^2/168 \end{bmatrix}$$

$$[k_{c_5}] = \begin{bmatrix} 1/7 & & & \\ \ell/28 & \ell^2/105 & & \text{symmetric} \\ -1/7 & -\ell/28 & 1/7 & \\ -\ell/28 & -\ell^2/84 & \ell/28 & \ell^2/14 \end{bmatrix}$$

$$[k_{c_6}] = \begin{bmatrix} 1/10 & & & \\ 11\ell/420 & \ell^2/140 & & \text{symmetric} \\ -1/10 & -11\ell/420 & 1/10 & \\ -\ell/30 & -3\ell^2/280 & \ell/30 & \ell^2/15 \end{bmatrix}$$

$$T_o = \Omega^2 \left\{ \frac{m_0}{2} [R^2 - (r + \ell)^2] + \frac{m_1}{3} \frac{1}{\ell} [R^3 - (r + \ell)^3] \right. \\ \left. + \frac{m_2}{4} \frac{1}{\ell^2} [R^4 - (r + \ell)^4] + \frac{m_3}{5} \frac{1}{\ell^3} [R^5 - (r + \ell)^5] \right\}$$

The element aerodynamic damping matrix is

$$[c] = \frac{1}{2} \rho_{\infty} a c \Omega \ell^2 \begin{bmatrix} \frac{13}{35} \frac{r}{\ell} + \frac{3}{35} & & & & \\ & \left(\frac{11}{210} \frac{r}{\ell} + \frac{1}{60} \right) \ell & \left(\frac{1}{105} \frac{r}{\ell} + \frac{1}{280} \right) \ell^2 & & \\ & & & \text{symmetric} & \\ & \frac{9}{70} \frac{r}{\ell} + \frac{9}{140} & \left(\frac{13}{420} \frac{r}{\ell} + \frac{1}{60} \right) \ell & \frac{13}{35} \frac{r}{\ell} + \frac{2}{7} & \\ - \left(\frac{13}{420} \frac{r}{\ell} + \frac{1}{70} \right) \ell & - \left(\frac{1}{140} \frac{r}{\ell} + \frac{1}{280} \right) \ell^2 & - \left(\frac{11}{210} \frac{r}{\ell} + \frac{1}{28} \right) \ell & \left(\frac{1}{105} \frac{r}{\ell} + \frac{1}{168} \right) \ell^2 & \end{bmatrix} \quad (B4)$$

The element load matrix [p] for a uniform harmonic load is given by

$$[p]^T = p_o \begin{Bmatrix} \ell/2 \\ \ell^2/12 \\ \ell/2 \\ -\ell^2/12 \end{Bmatrix} e^{i\omega t} \quad (B5)$$

APPENDIX C

EQUATIONS OF MOTION

The equations of motion for an element of a rotating beam can be derived from Hamilton's equation,

$$\delta \int_{t_1}^{t_2} (\mathcal{U} - \mathcal{F}) dt - \int_{t_1}^{t_2} \delta \mathcal{W} dt = 0 \quad (C1)$$

Substituting equations (A7), (A15), (A19), and (A22) of appendix A into equation (C1) and carrying out the indicated variations yield the element equations of motion,

$$[m]\{\ddot{q}\} + [c]\{\dot{q}\} + ([k_E] + [k_C])\{q\} = \{p\} \quad (C2)$$

For a system made up of more than one finite element, the element mass, damping, and stiffness matrices $[m]$, $[c]$, and $([k_E] + [k_C])$ and element load vector $\{p\}$ can be assembled into the corresponding global matrices $[M]$, $[C]$, and $([K_E] + [K_C])$, and global vector $\{P\}$. Then equation (C2) may be rewritten as

$$[M]\{\ddot{q}\} + [C]\{\dot{q}\} + ([K_E] + [K_C])\{q\} = \{P\} \quad (C3)$$

This is the basic matrix equation of motion considered in the present analysis.

For the case of free harmonic vibration (*in vacuo*), the damping matrix $[C]$ and the load vector $\{P\}$ are set to zero in equation (C3) and we obtain the eigenvalue problem,

$$[\lambda] [M]\{q\} = ([K_E] + [K_C])\{q\} \quad (C4)$$

which has the real eigenvalues $\lambda = \omega_n^2$ and the matrix of real eigenvectors $[U]$.

In carrying out the complex eigenvalue analysis of equation (C3), it is useful to uncouple the equations of motion as outlined by Meirovitch (ref. 8). A coordinate transformation is first performed on equation (C3) by replacing

$$\{q\} = [U]\{\bar{q}\} \quad (C5)$$

where $[U]$ is the matrix of orthonormal modes associated with the real eigenvalue analysis of equation (C4). Then equation (C3) is premultiplied by $[U]^T$, yielding

$$[U]^T [M] [U] \{\ddot{\bar{q}}\} + [U]^T [C] [U] \{\dot{\bar{q}}\} + [U]^T ([K_E] + [K_C]) [U] \{\bar{q}\} = [U]^T \{P\} \quad (C6)$$

Since the normal modes $[U]$ from equation (C4) are such that

$$[U]^T [M] [U] = [I] \quad (C7)$$

and

$$[U]^T ([K_E] + [K_C]) [U] = [\omega_n^2] \quad (C8)$$

where $[I]$ is the identity matrix, equation (C6) becomes

$$[I]\{\ddot{\bar{q}}\} + [\bar{C}]\{\dot{\bar{q}}\} + [\omega_n^2]\{\bar{q}\} = \{\bar{P}\} \quad (C9)$$

where

$$[\bar{C}] = [U]^T[C][U] \quad (C10)$$

and

$$\{\bar{P}\} = [U]^T\{P\} \quad (C11)$$

The complex eigenvalues of equation (C9) can then be determined from

$$\begin{Bmatrix} \dot{\bar{q}} \\ \ddot{\bar{q}} \end{Bmatrix} = \begin{bmatrix} [0] & [I] \\ -[\omega_n^2] & -[\bar{C}] \end{bmatrix} \begin{Bmatrix} \bar{q} \\ \dot{\bar{q}} \end{Bmatrix} \quad (C12)$$

Alternatively, for harmonic excitations,

$$\{\bar{P}\} = \{\bar{P}_0\}e^{i\omega t} \quad (C13)$$

and

$$\{\bar{q}\} = \{\bar{q}_0\}e^{i\omega t} \quad (C14)$$

so that equation (C9) can be rewritten as

$$([\omega_n^2 - \omega^2] + i\omega[\bar{C}])\{\bar{q}_0\} = \{\bar{P}_0\} \quad (C15)$$

where

$$\{\bar{P}_0\} = [U]^T\{P_0\}$$

The responses obtained from equation (C15) are the modal responses as a function of forcing frequency ω for a given applied load vector $\{P_0\}$. The corresponding nodal responses $\{q_0\}$ can then be obtained from equation (C5).

In the frequency-response analysis, structural damping can be readily included by introducing the complex stiffness $k(1 + ig)$ in place of k where $g > 0$ is the structural damping factor (ref. 9). Then equation (C15) becomes

$$([\omega_n^2(1 + ig) - \omega^2] + i\omega[\bar{C}])\{\bar{q}_0\} = \{\bar{P}_0\} \quad (C16)$$

In the present finite element analysis, the total number of degrees of freedom is equal to twice the number of node points minus the number of rigid body constraints. In general, however, only a relatively small number of these modes are of interest. In this case, the formulation described above can be used to obtain approximate, but still very accurate results if a reduced set of only the lower frequency modes necessary to give sufficiently converged results is used in equation (C6). This approximation has the advantage that instead of solving the complete system of equations

presented in equation (C9) one can achieve nearly as accurate results for the lower-frequency modes of interest with a reduced system of equations. All of the results presented in this report, however, were obtained from analyses which include all of the collective rotor modes and symmetric fuselage-bending modes.

REFERENCES

1. Staley, J. A.; and Sciarra, J. J.: Coupled Rotor/Airframe Vibration Prediction Methods. NASA SP-352, 1974, pp. 81-90.
2. Hohenemser, K. H.; and Yin, S.-K.: The Role of Rotor Impedance in the Vibration Analysis of Rotorcraft. Vertica, vol. 3, nos. 3/4, 1979, pp. 189-204.
3. Hsu, T.-K.; and Peters, D. A.: Coupled Rotor/Airframe Vibration Analysis by a Combined Harmonic-Balance, Impedance-Matching Method. J. American Helicopter Soc., vol. 27, no. 1, Jan. 1982, pp. 25-34.
4. Kunz, D. L.: Effects of Rotor-Body Coupling in a Linear Rotorcraft Vibration Model. Paper no. 23, 36th Annual Forum of the American Helicopter Society, Washington, D.C., May 1980.
5. Przemieniecki, J. S.: Theory of Matrix Structural Analysis. McGraw-Hill Book Co., New York, 1968.
6. Hodges, D. H.; and Rutkowski, M. J.: Free Vibration Analysis of Rotating Beams by a Variable-Order Finite Element Method. AIAA J., vol. 19, no. 11, Nov. 1981, pp. 1459-1466.
7. Bartlett, F. D., Jr.; and Flannelly, W. G.: Application of Antiresonance Theory to Helicopters. NASA SP-352, 1974, pp. 101-106.
8. Meirovitch, L.: Analytical Methods in Vibrations. The Macmillan Company, New York, 1967.
9. Scanlan, R. H.; and Rosenbaum, R.: Introduction to the Study of Aircraft Vibration and Flutter. The Macmillan Company, New York, 1951.

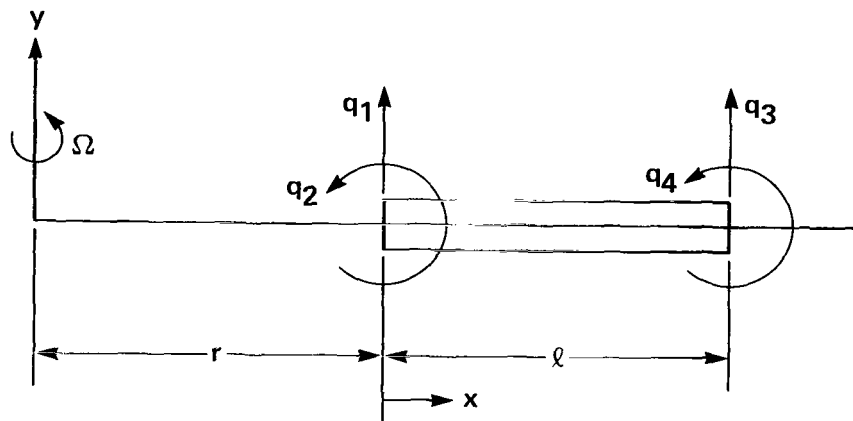


Figure 1.- Beam-element geometry.

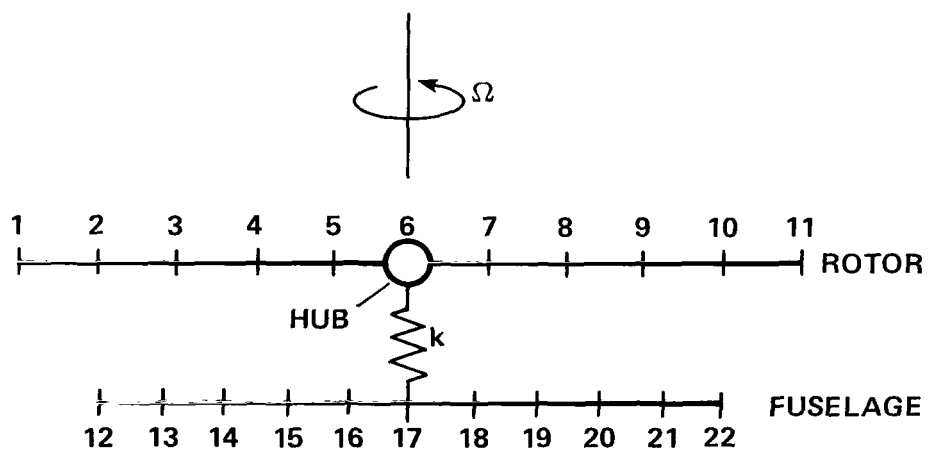


Figure 2.- Rotorcraft model.

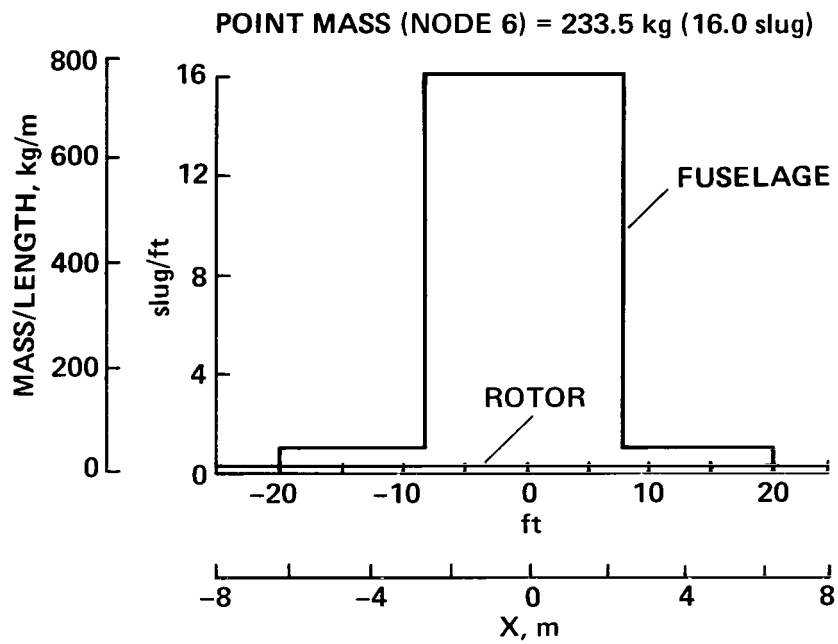


Figure 3.- Rotor and fuselage mass distributions.

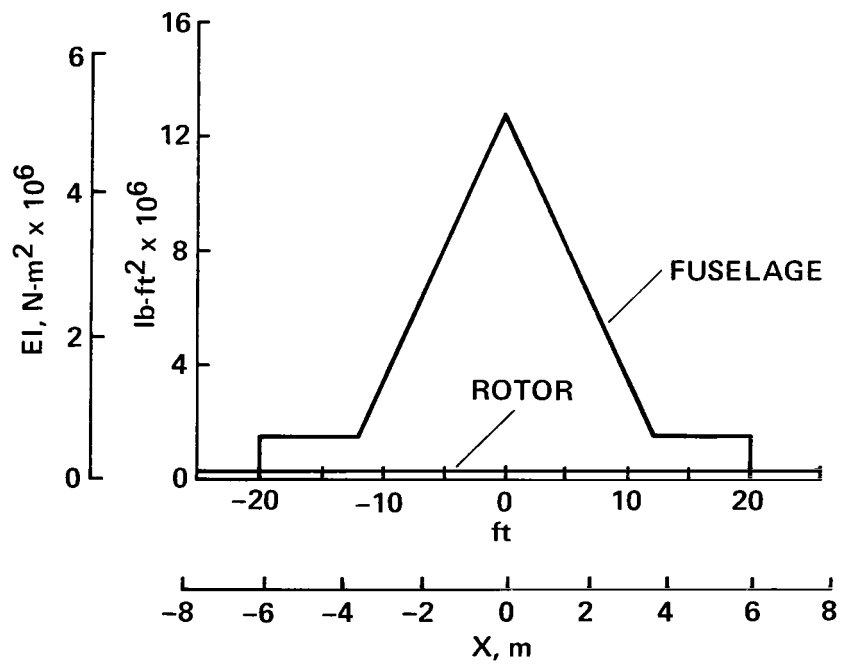
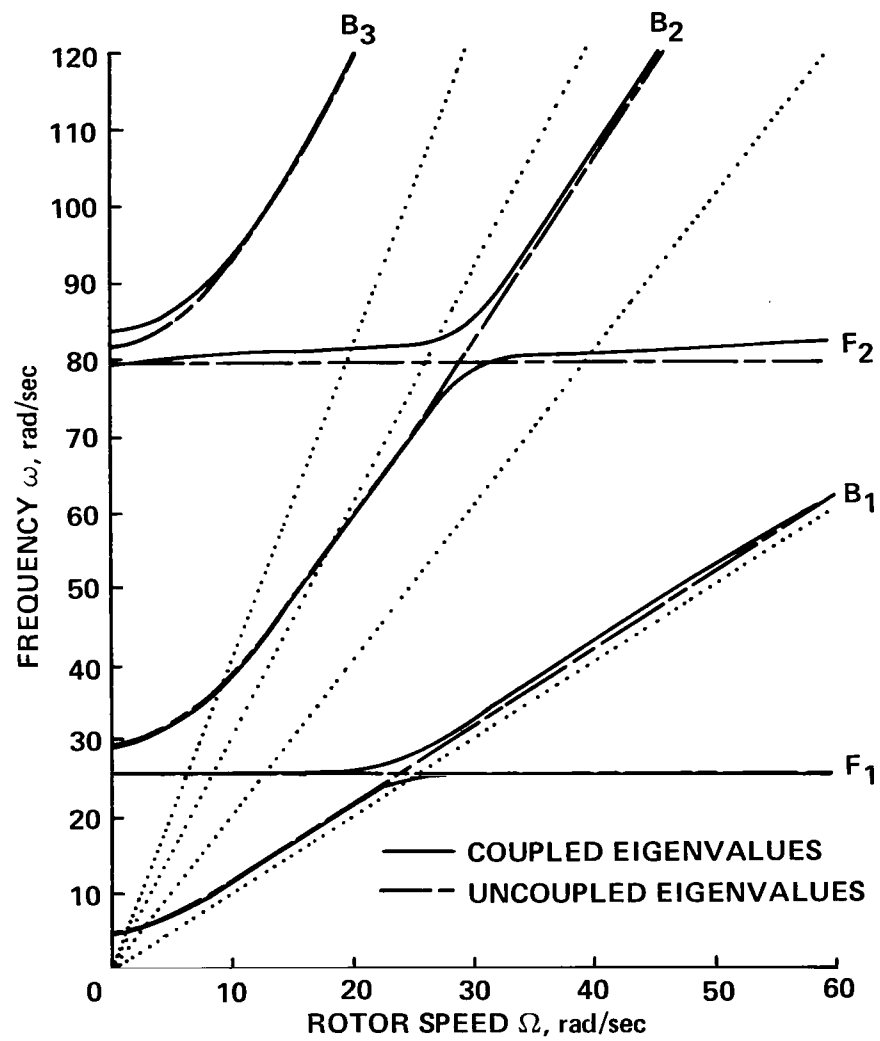
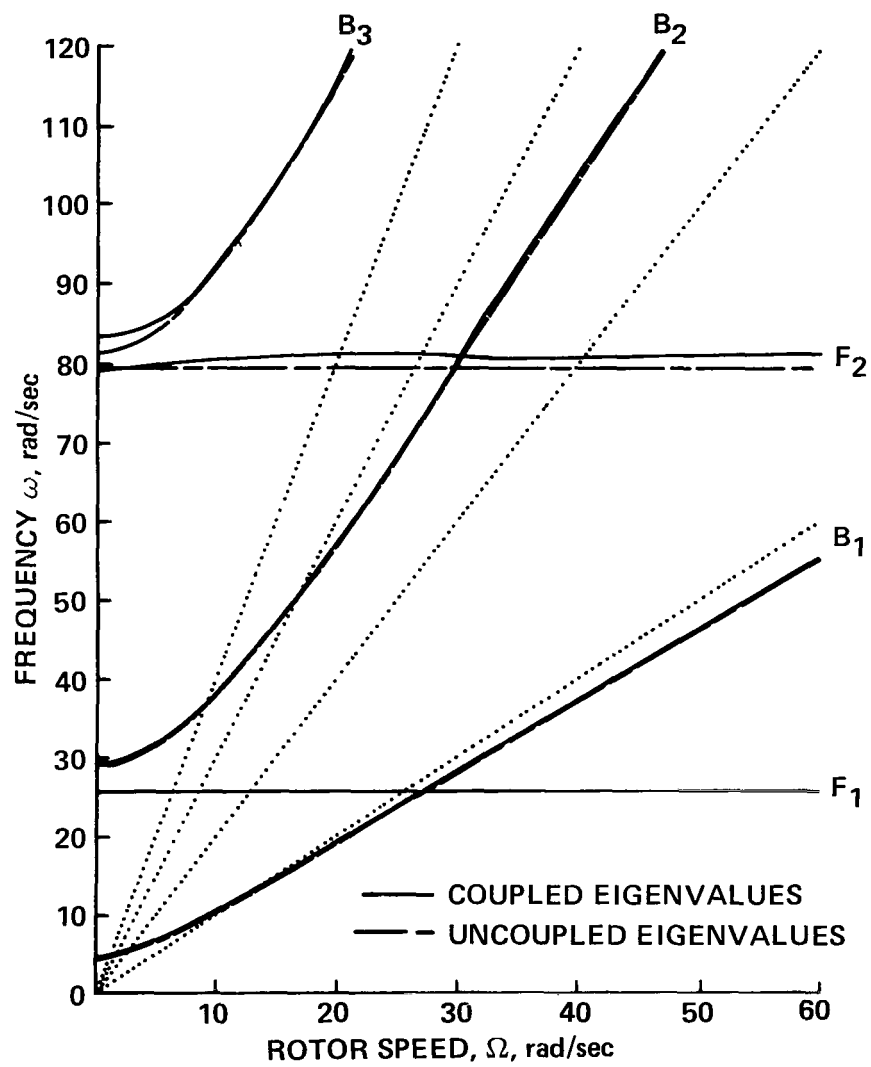


Figure 4.- Rotor and fuselage stiffness distributions.



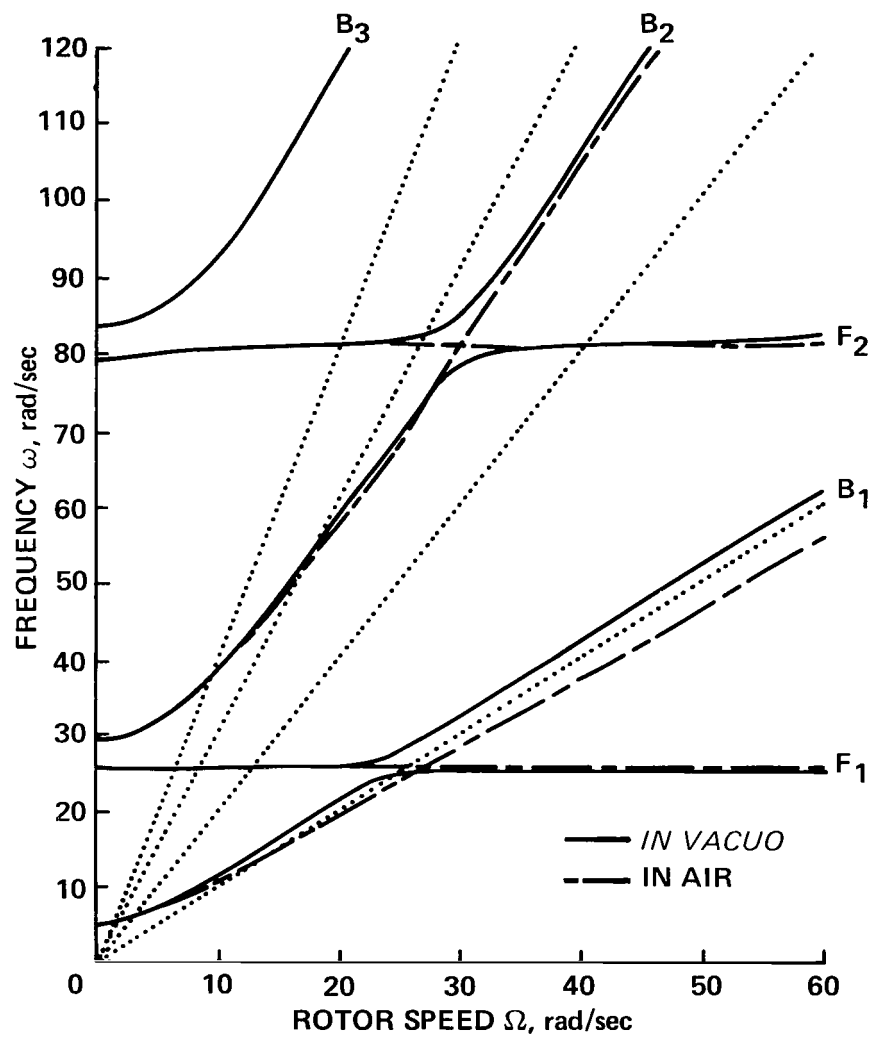
(a) *In vacuo.*

Figure 5.- Coupled and uncoupled rotor-fuselage eigenvalues.



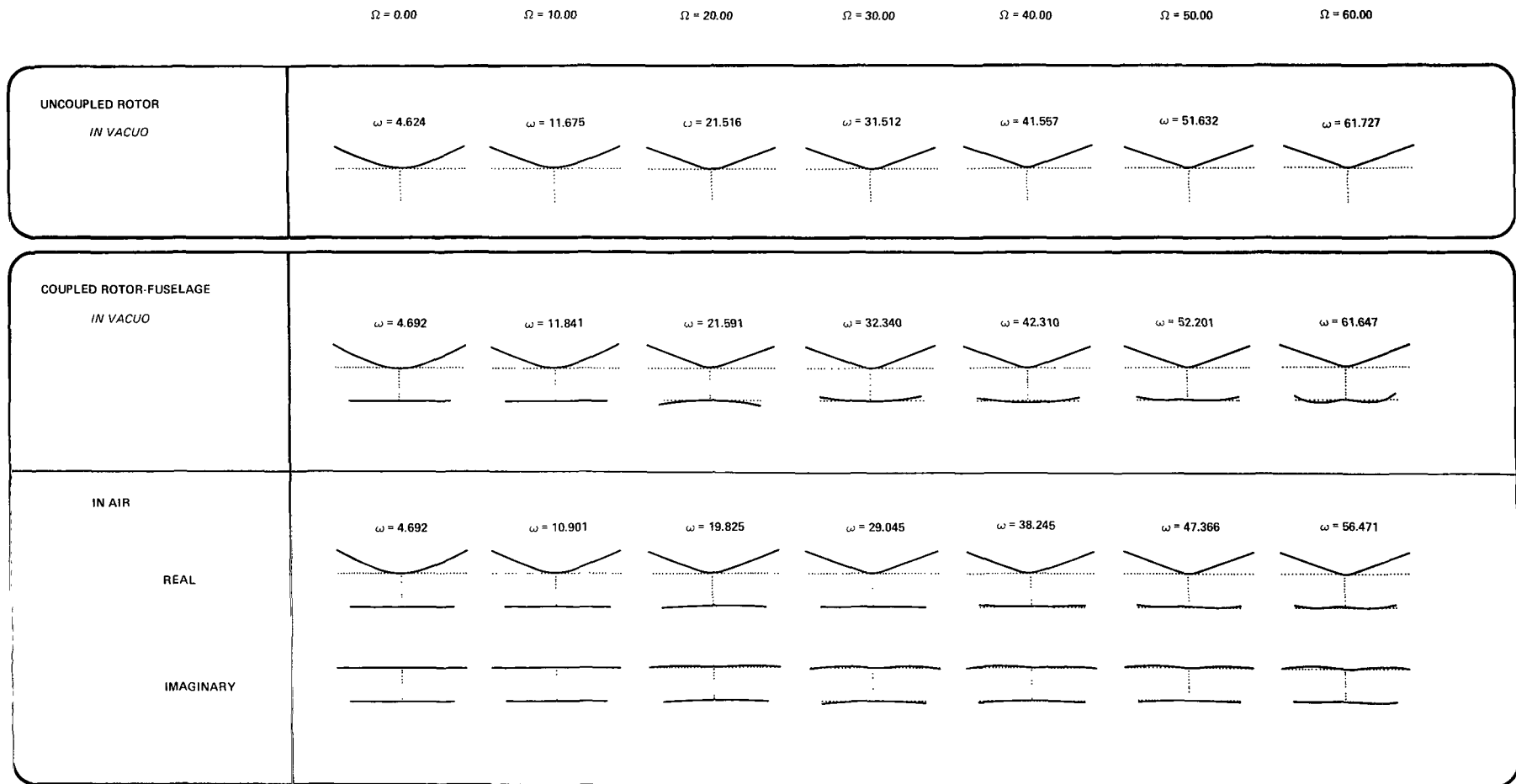
(b) In air.

Figure 5.- Continued.



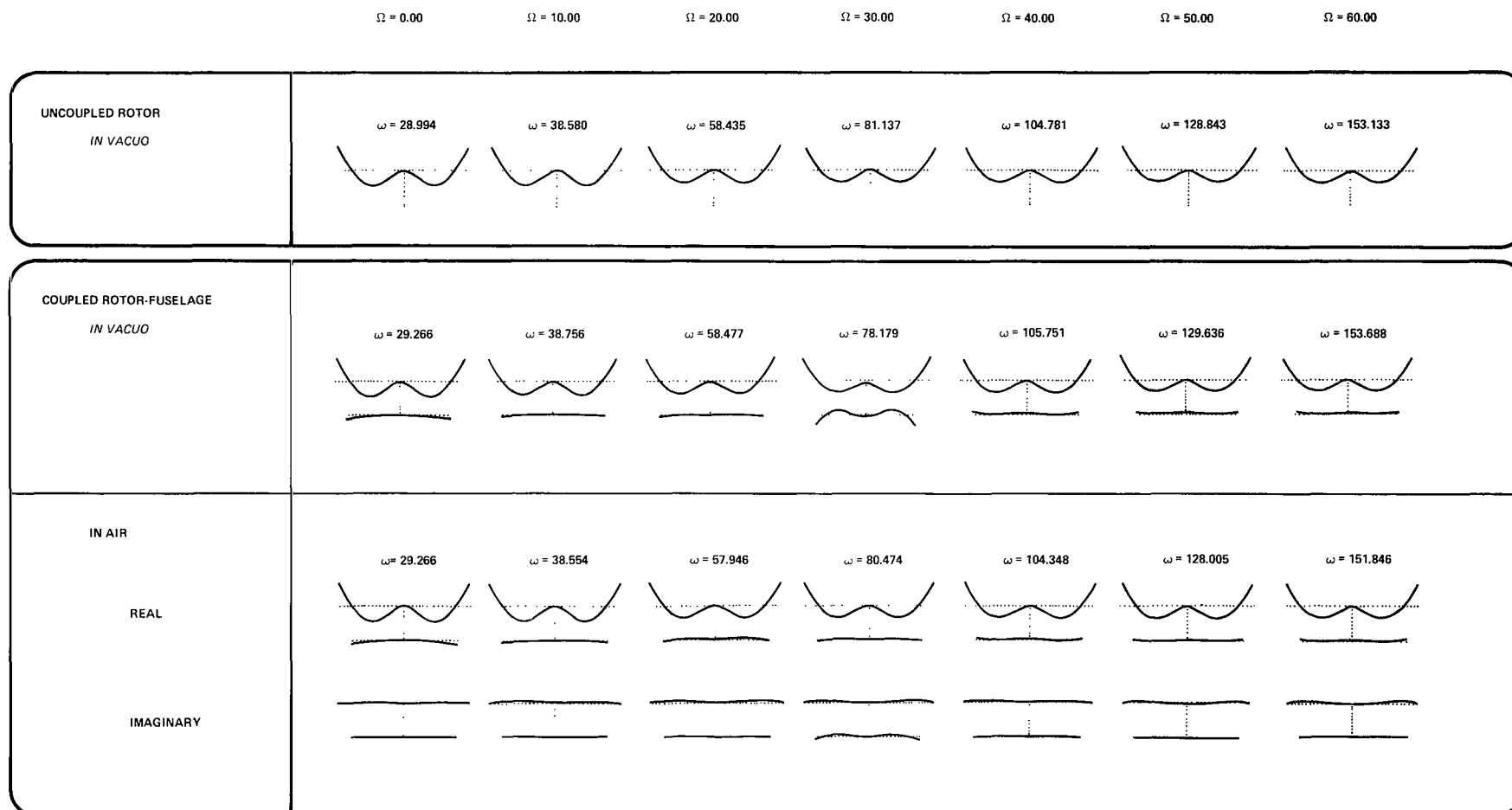
(c) Coupled modes *in vacuo* and in air.

Figure 5.- Concluded.



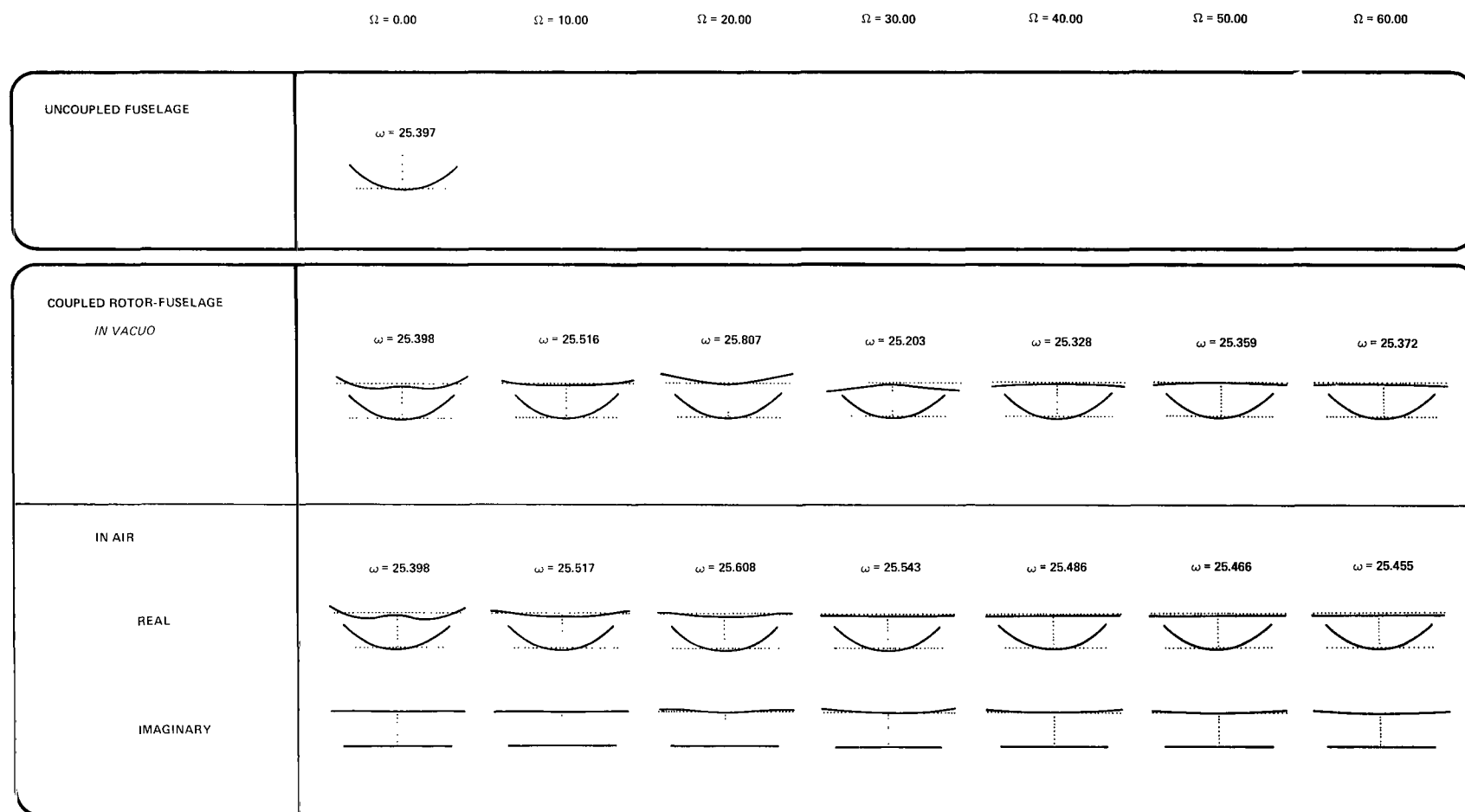
(a) First rotor-flap mode.

Figure 6.- Uncoupled and coupled rotor-fuselage mode shapes.



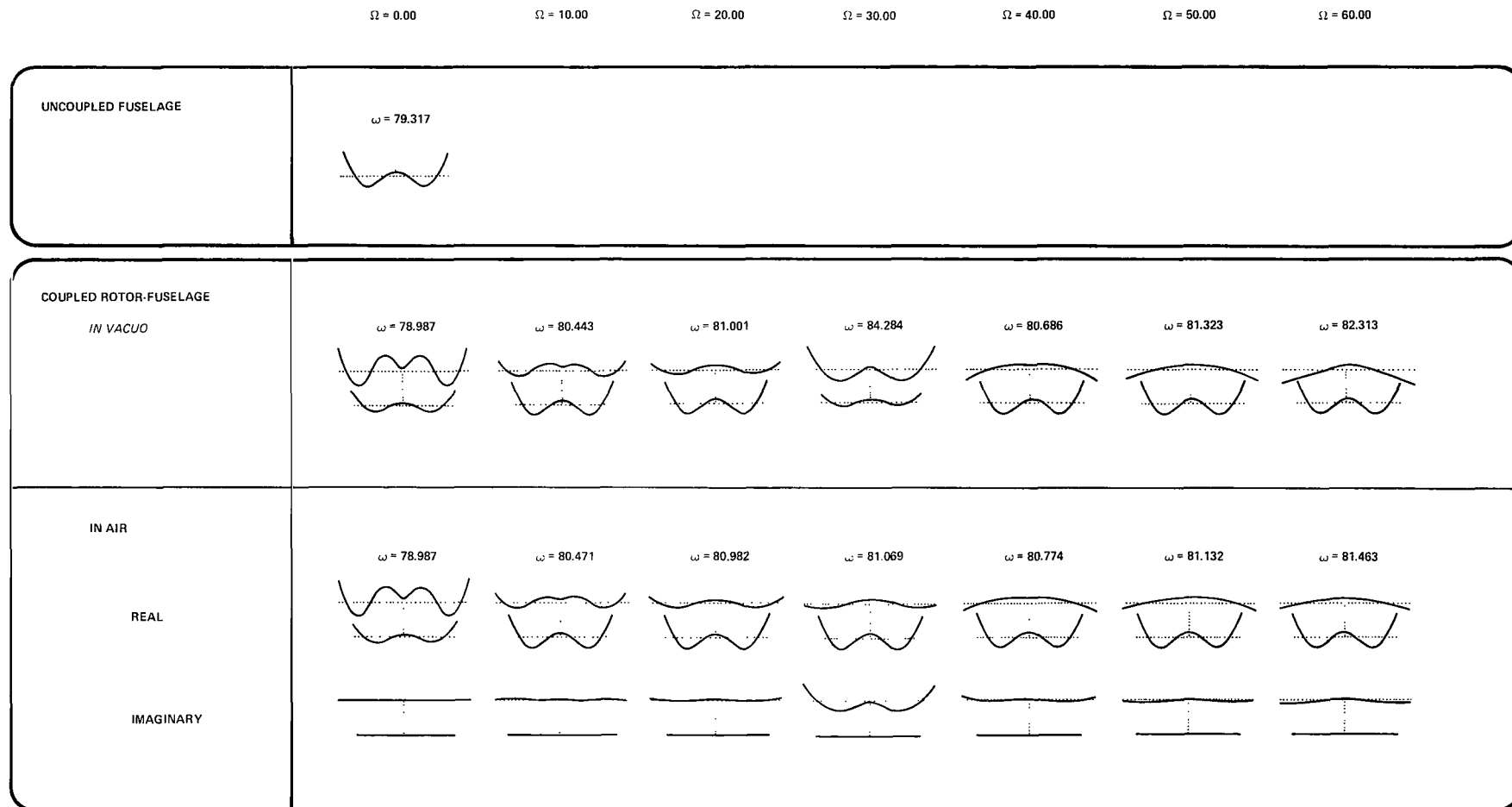
(b) Second rotor-flap mode.

Figure 6.- Continued.



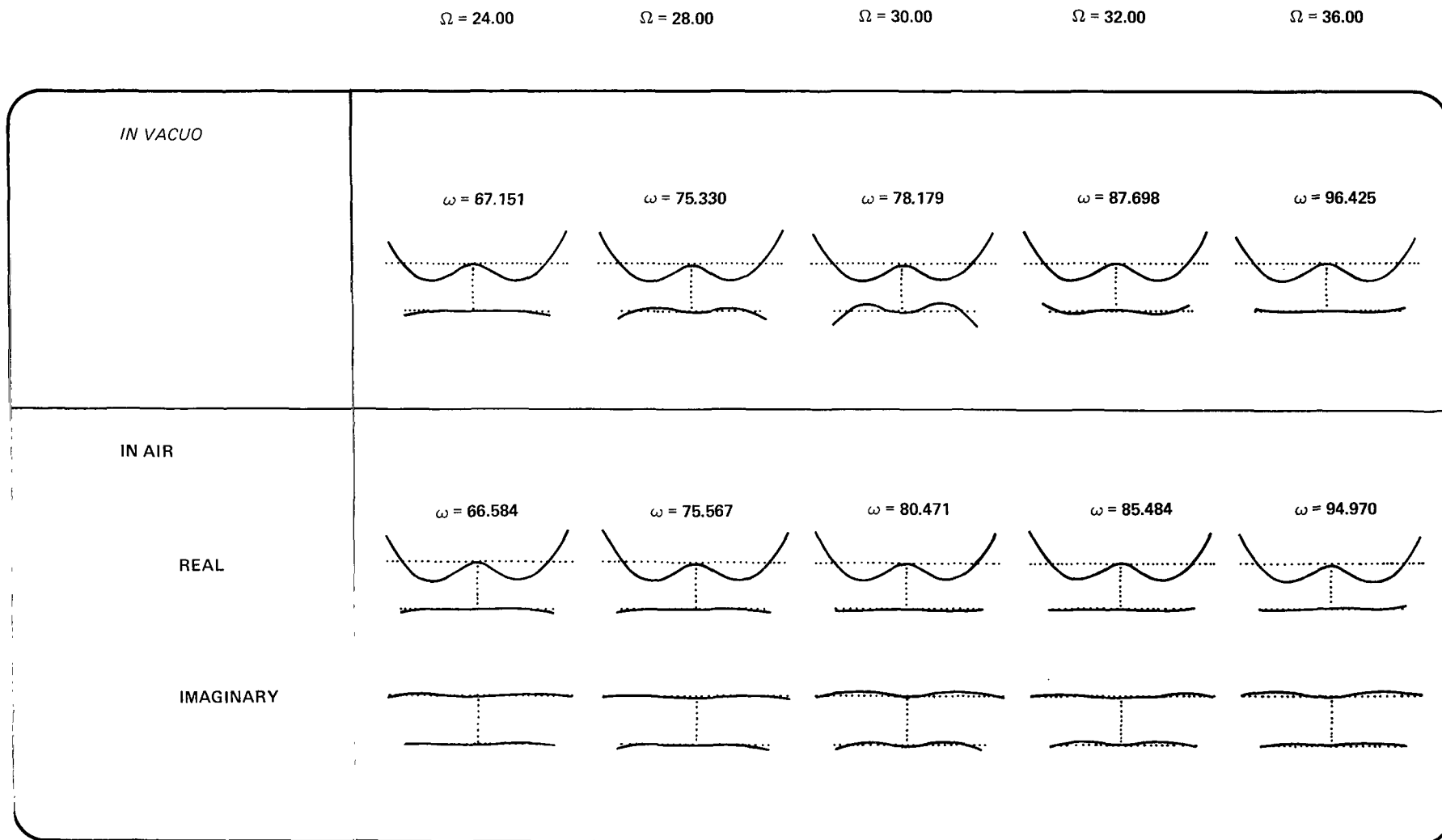
(c) First symmetric fuselage-bending mode.

Figure 6.- Continued.



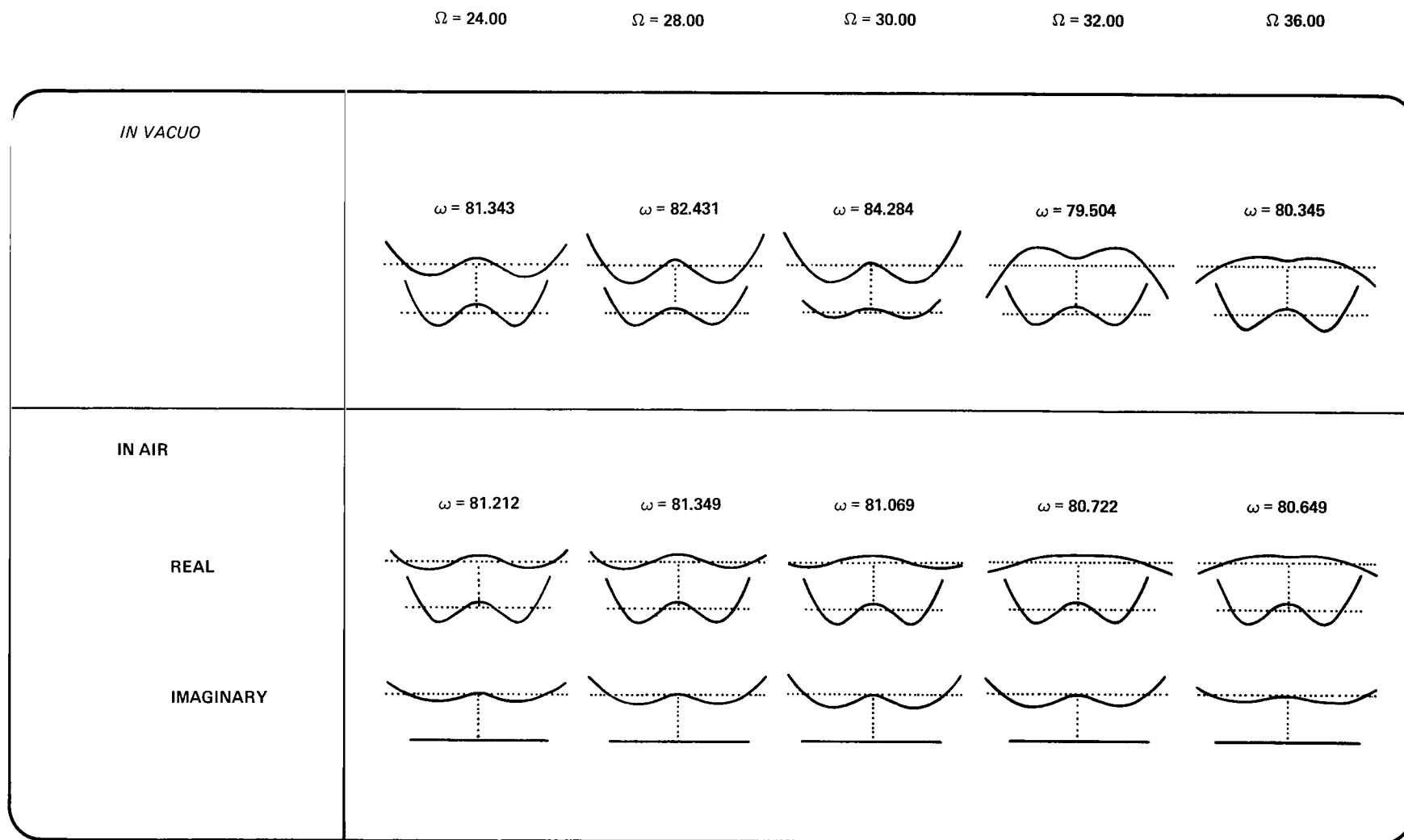
(d) Second symmetric fuselage-bending mode.

Figure 6.- Concluded.



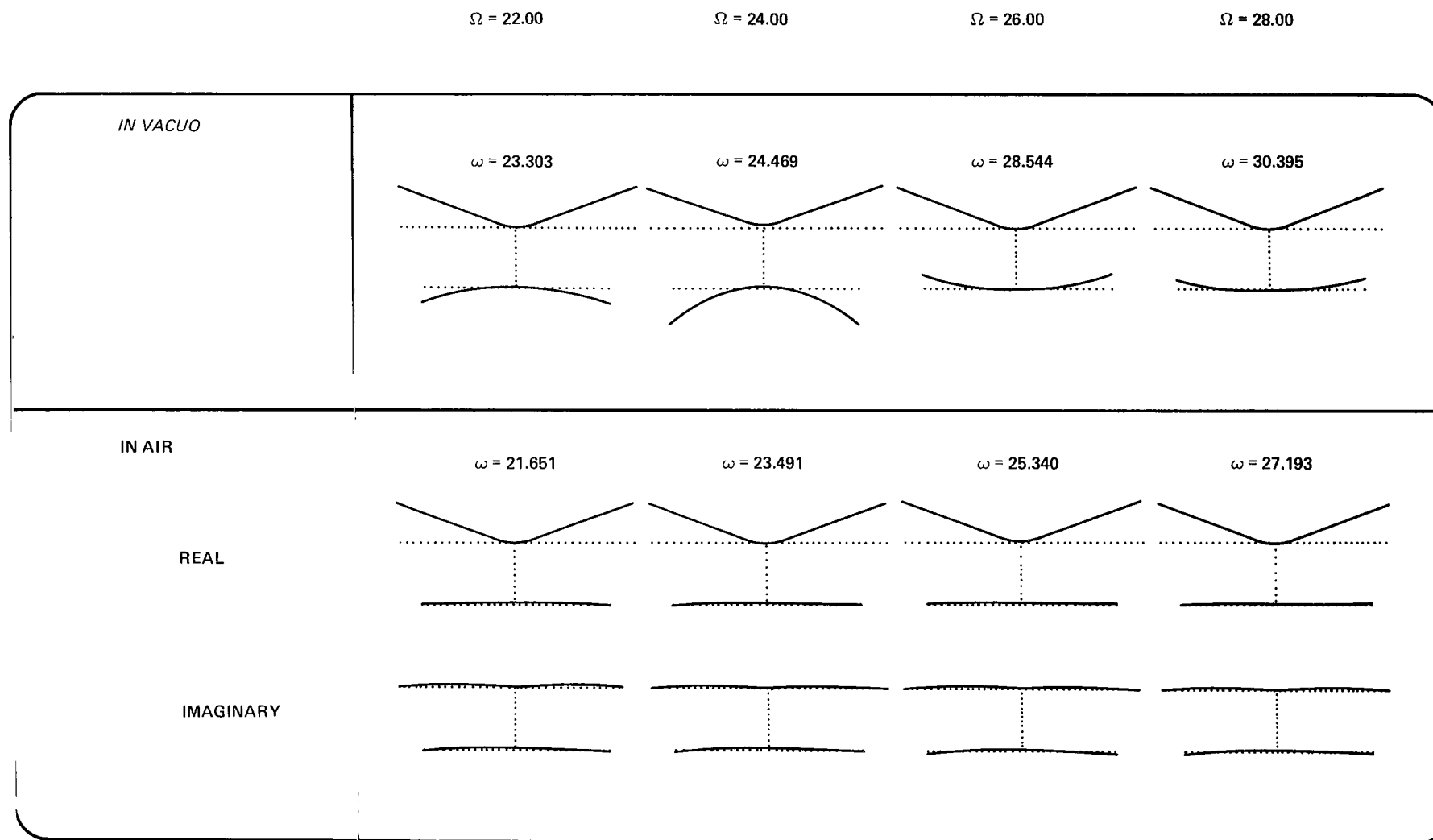
(a) Second rotor-flap mode, $\Omega = 24-36$ rad/sec.

Figure 7.- Coupled rotor-fuselage mode shapes near coalescences.



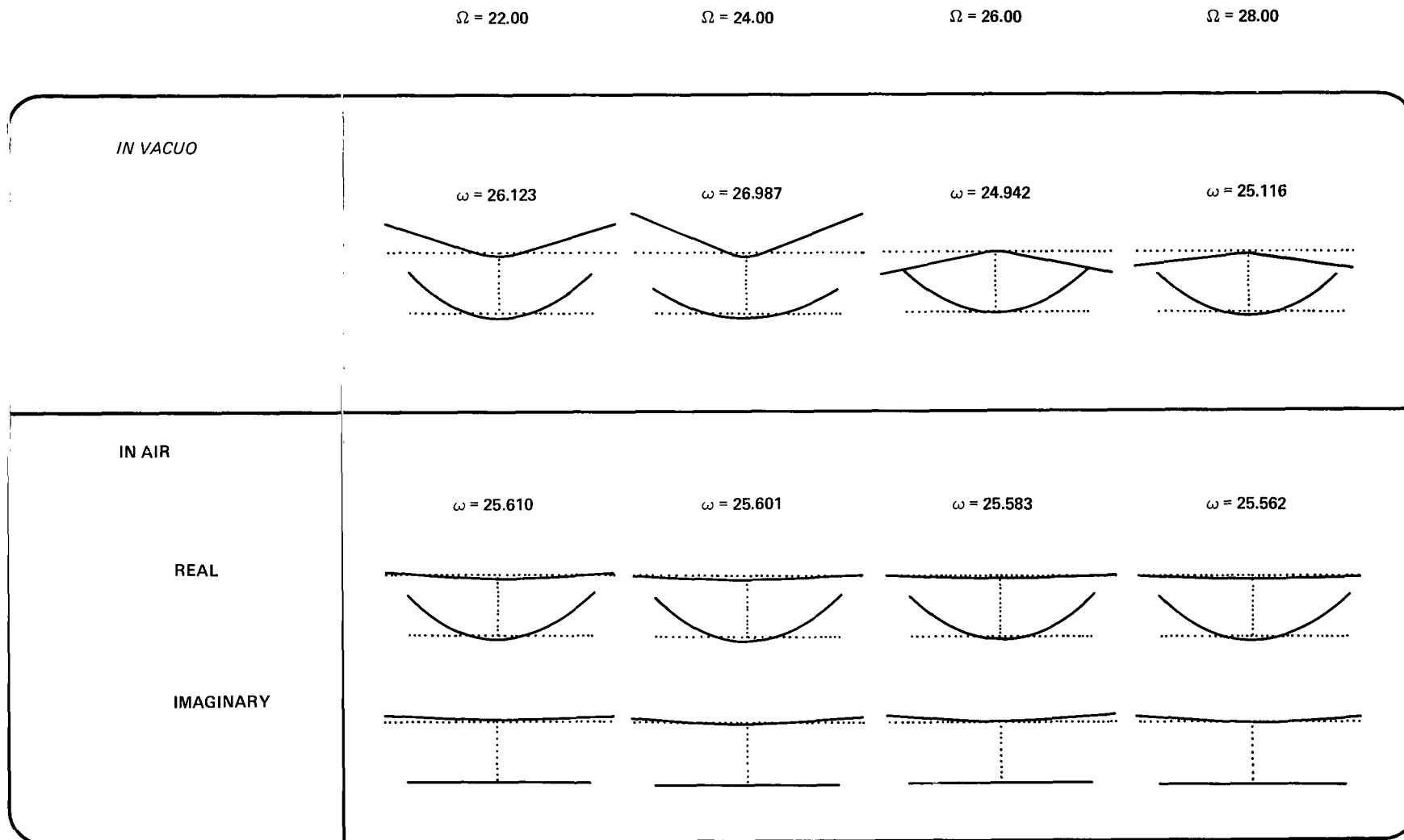
(b) Second symmetric fuselage-bending mode, $\Omega = 24-36$ rad/sec.

Figure 7.- Continued.



(c) First rotor-flap mode, $\Omega = 22-28$ rad/sec.

Figure 7.- Continued.



(d) First symmetric fuselage-bending mode, $\Omega = 22-28$ rad/sec.

Figure 7.- Concluded.

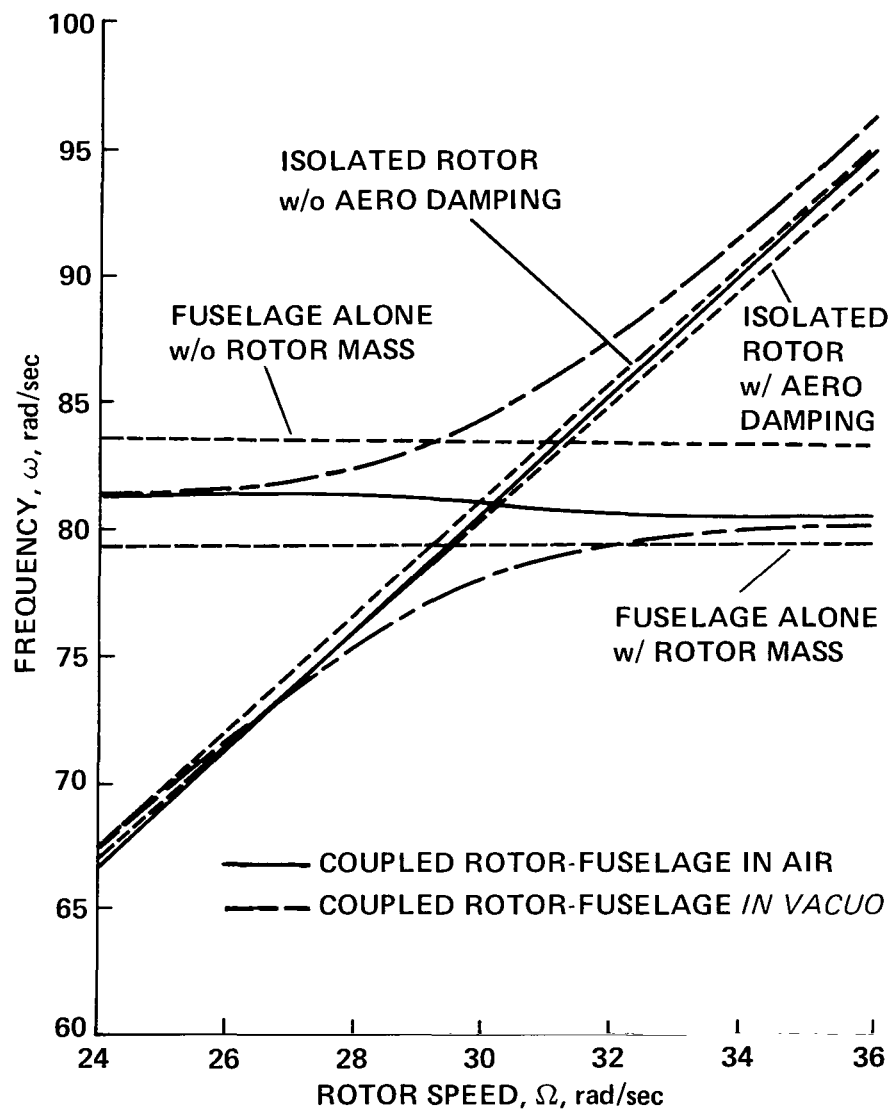


Figure 8.- Effect of dynamic coupling and aerodynamic damping on the coupled rotor-fuselage modal frequencies near a coalescence.

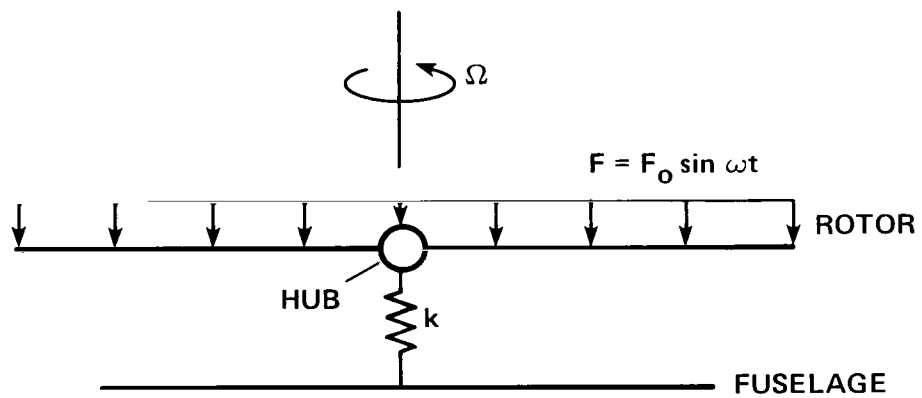
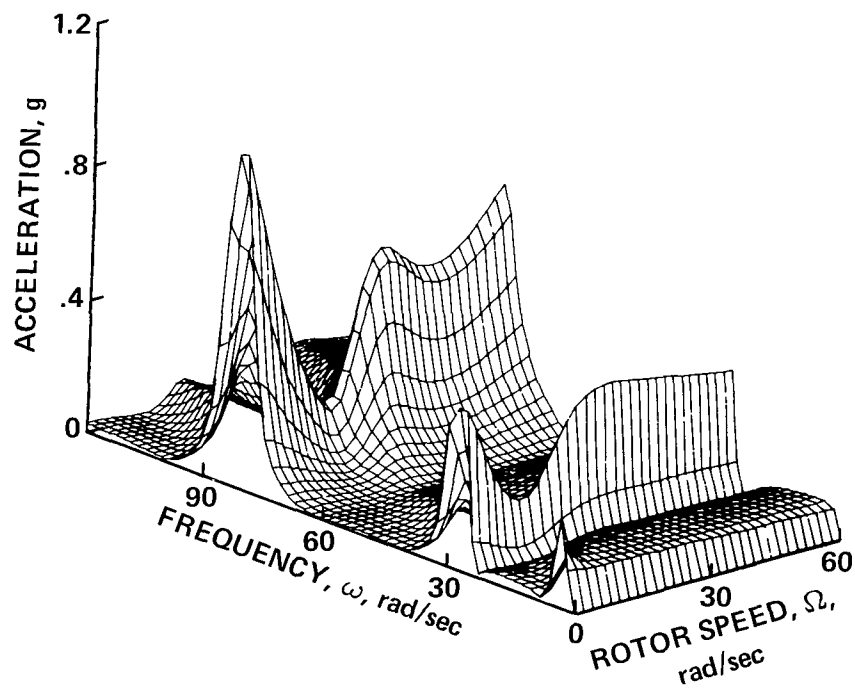
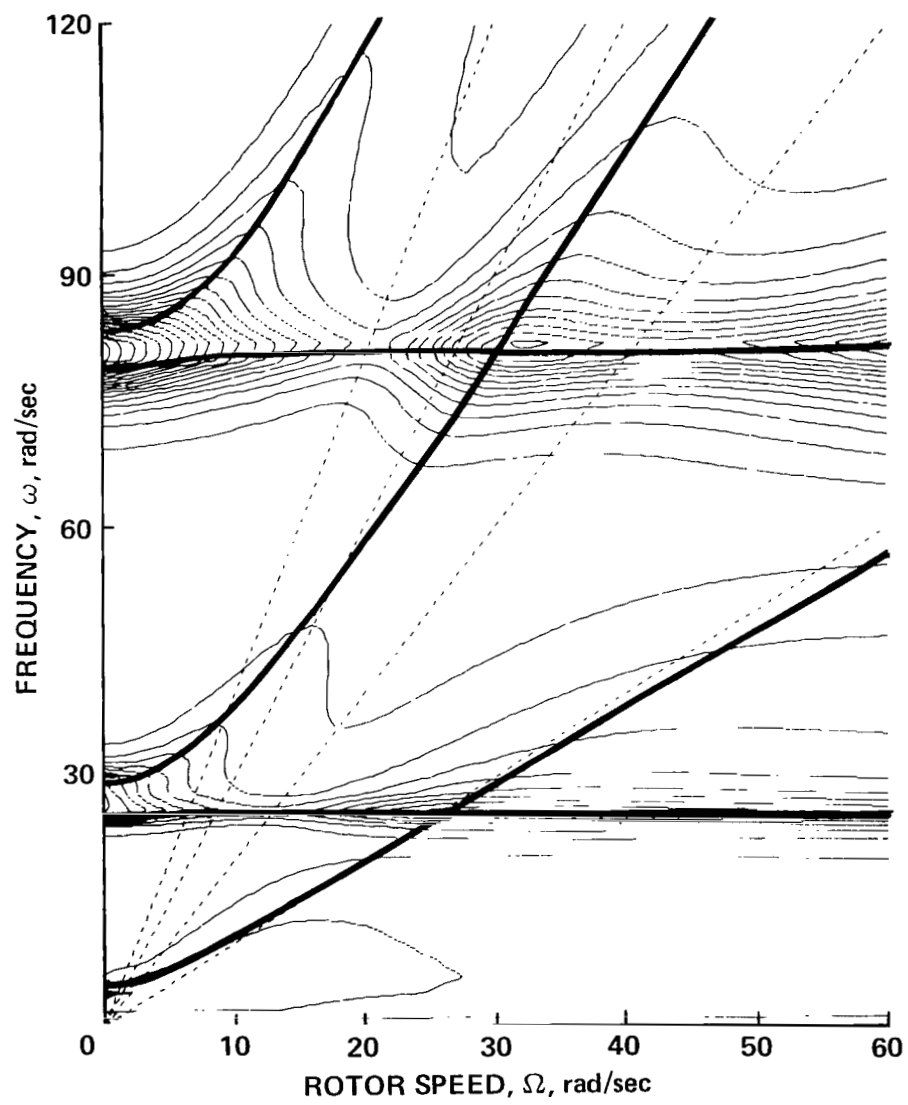


Figure 9.- Excitation for coupled rotor-fuselage model.



(a) 3-D plot.

Figure 10.- Coupled rotor-fuselage response at node 17.



(b) Contour plot.

Figure 10.- Concluded.

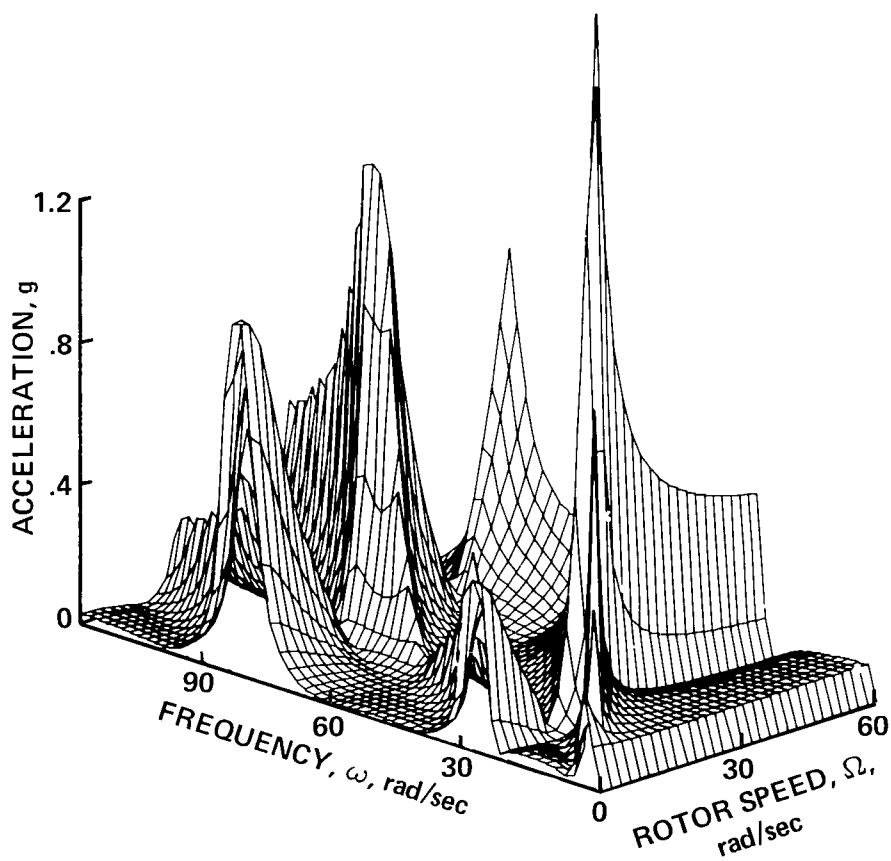


Figure 11.- Coupled rotor-fuselage response at node 17; without aerodynamic damping.

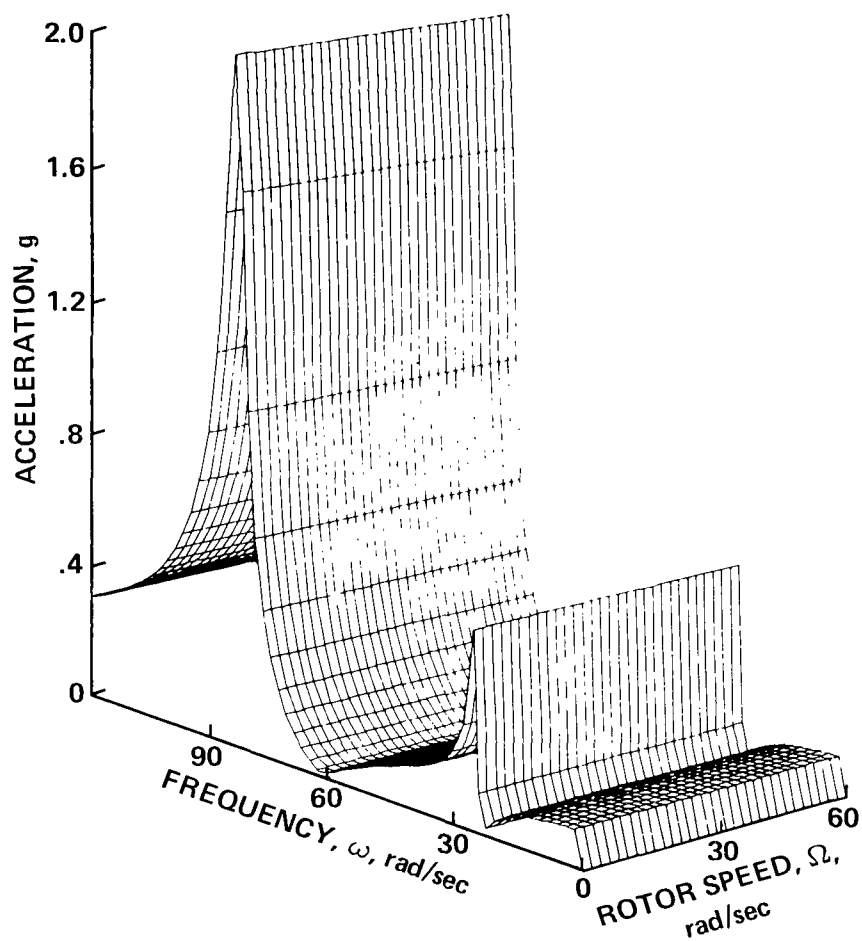


Figure 12.- Uncoupled fuselage response at node 17 to an oscillatory point-load at rotor hub location; acceleration versus forcing frequency and rotor speed.

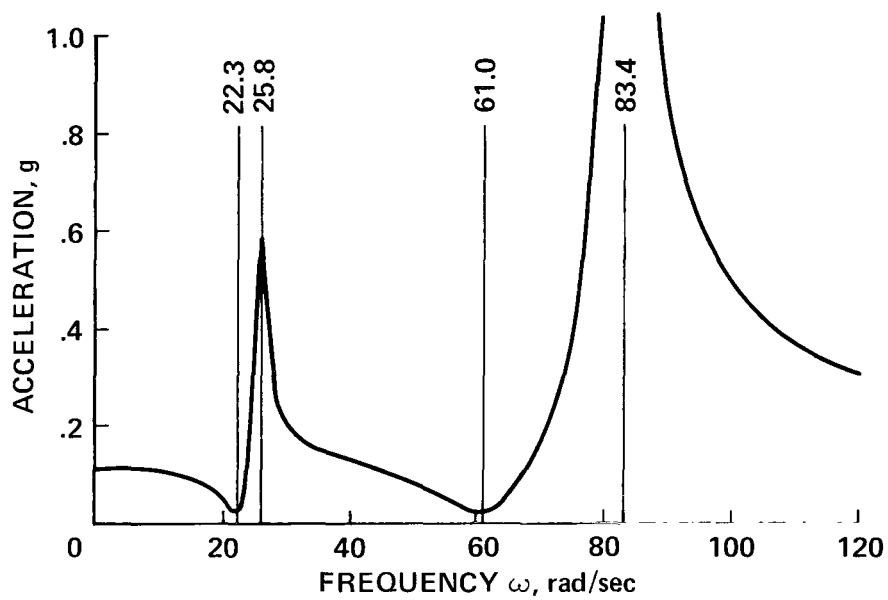


Figure 13.- Uncoupled fuselage response at node 17 to an oscillatory point-load at rotor hub location; acceleration versus forcing frequency.

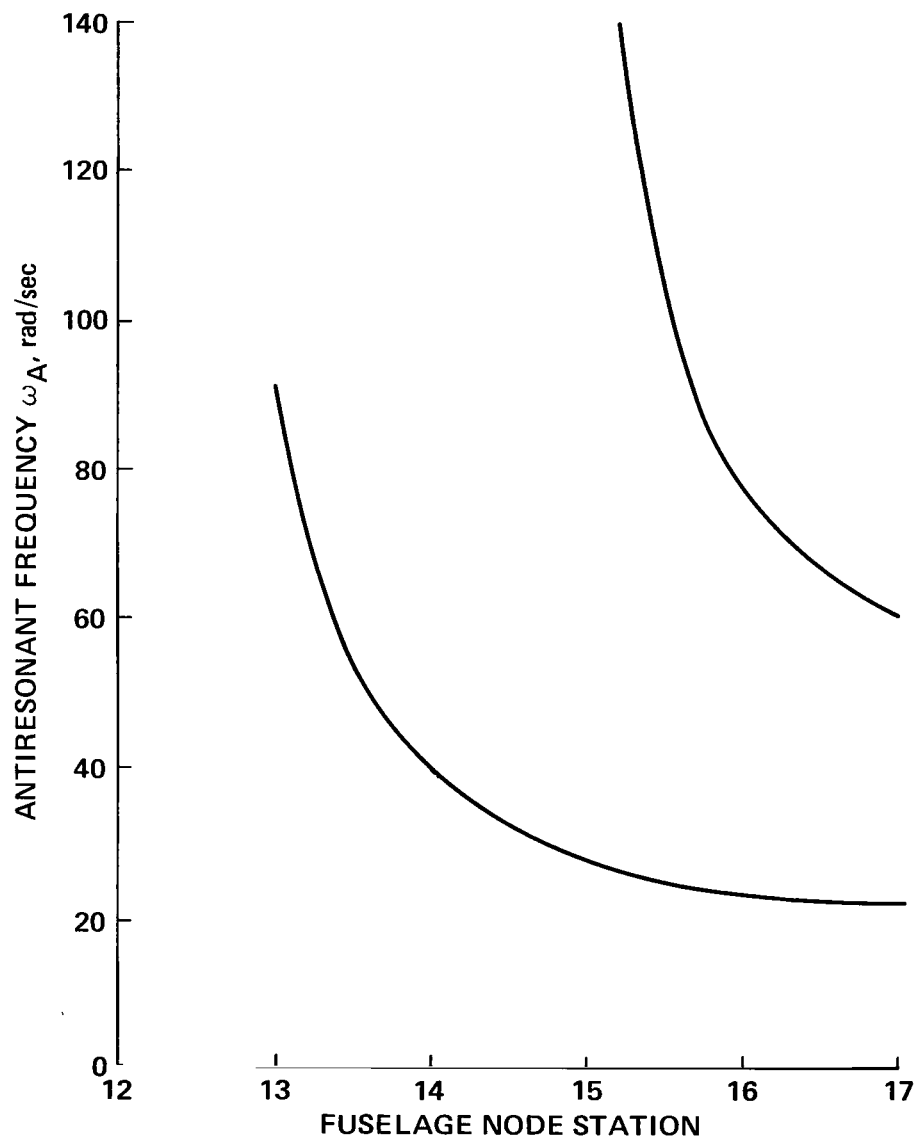
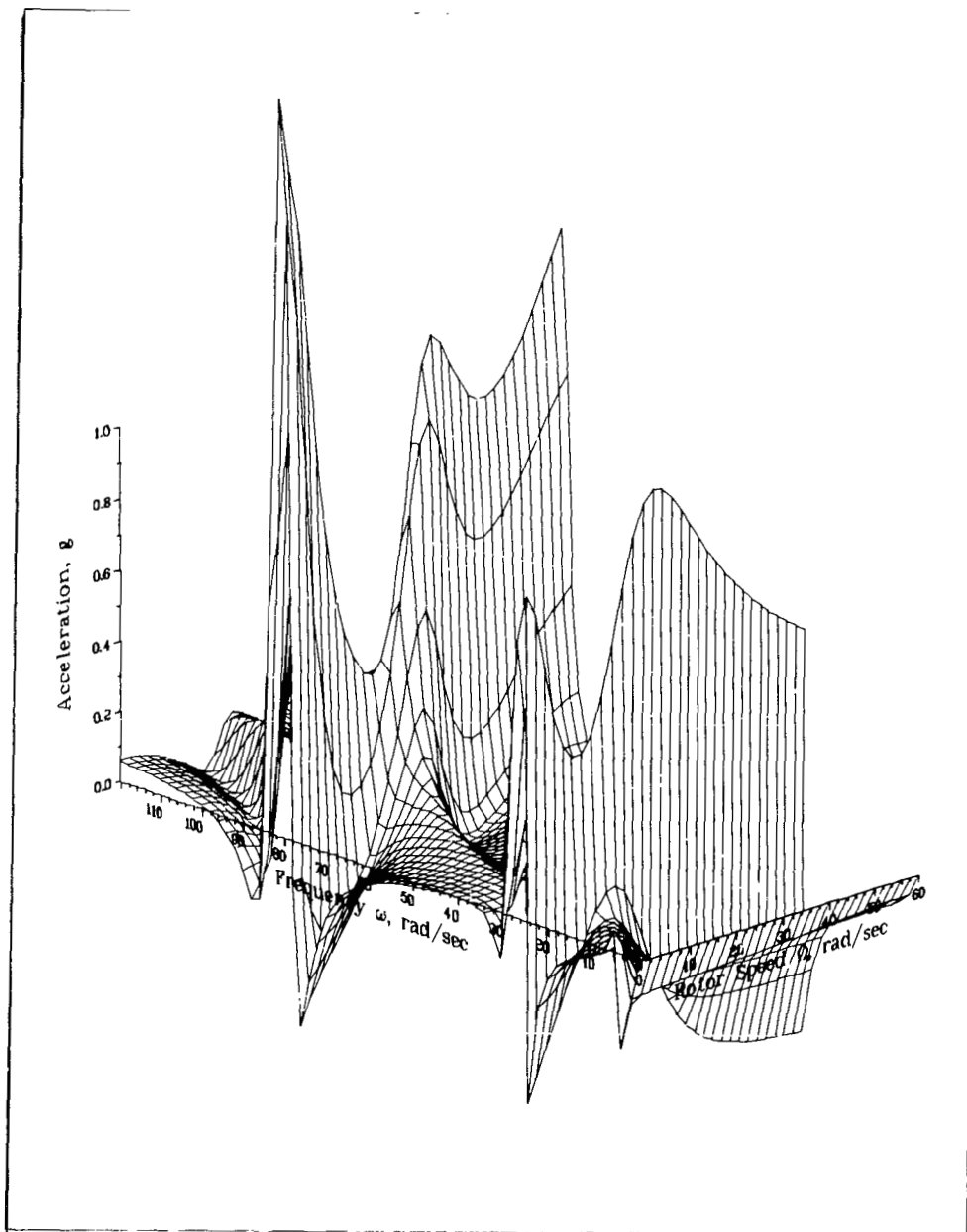
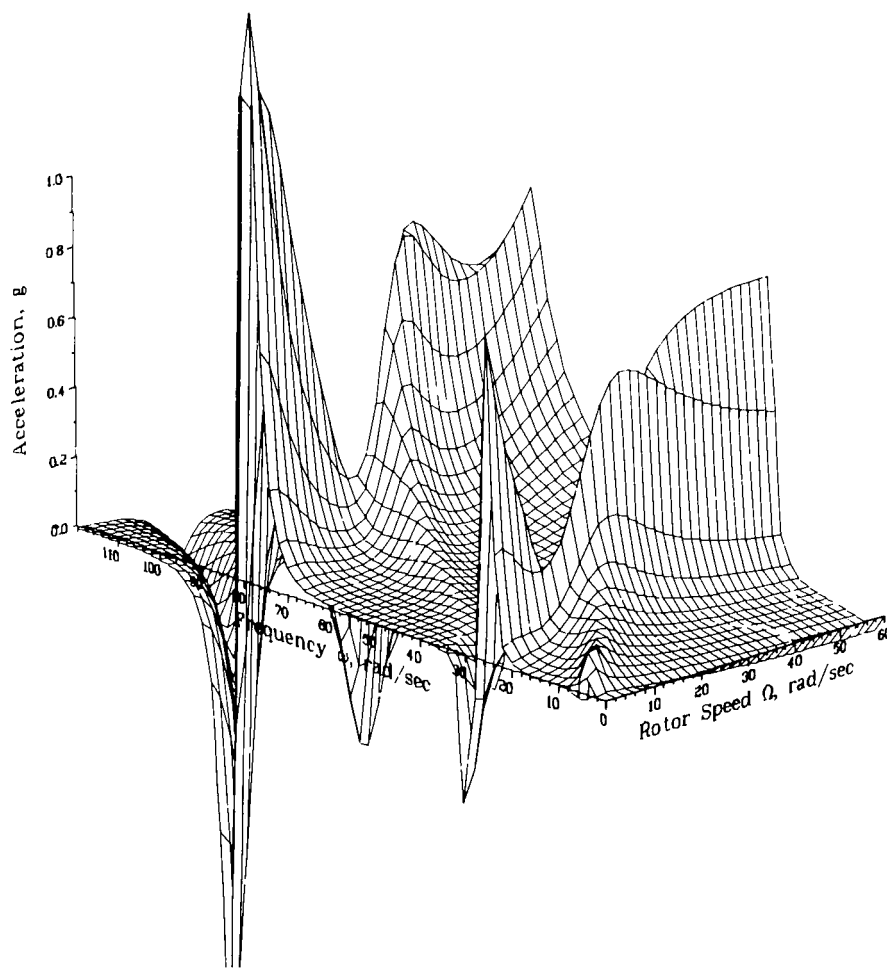


Figure 14.- Antiresonant frequency versus fuselage station for forcing at node 17.



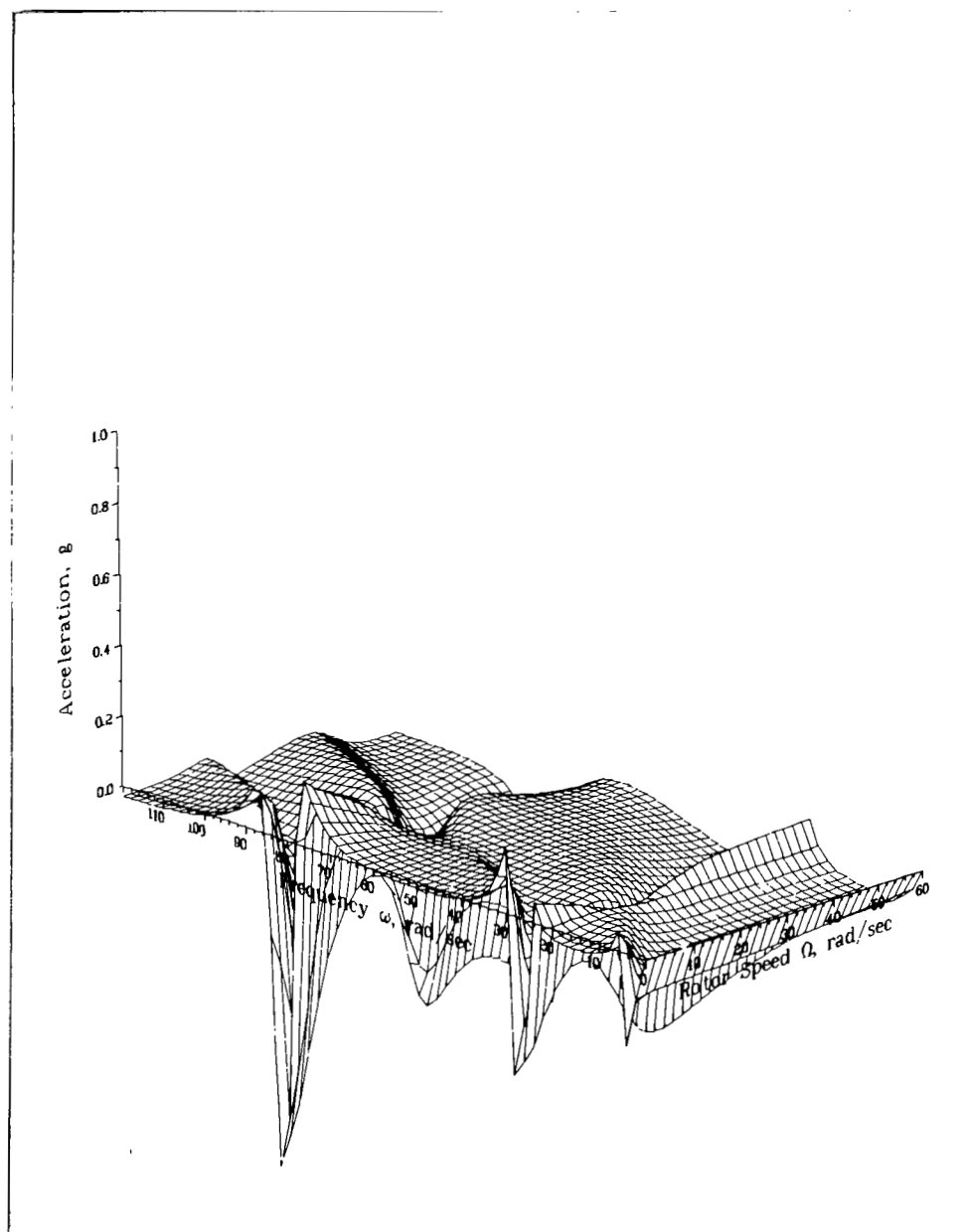
(a) Real component at node 14.

Figure 15.- Coupled rotor-fuselage complex response.



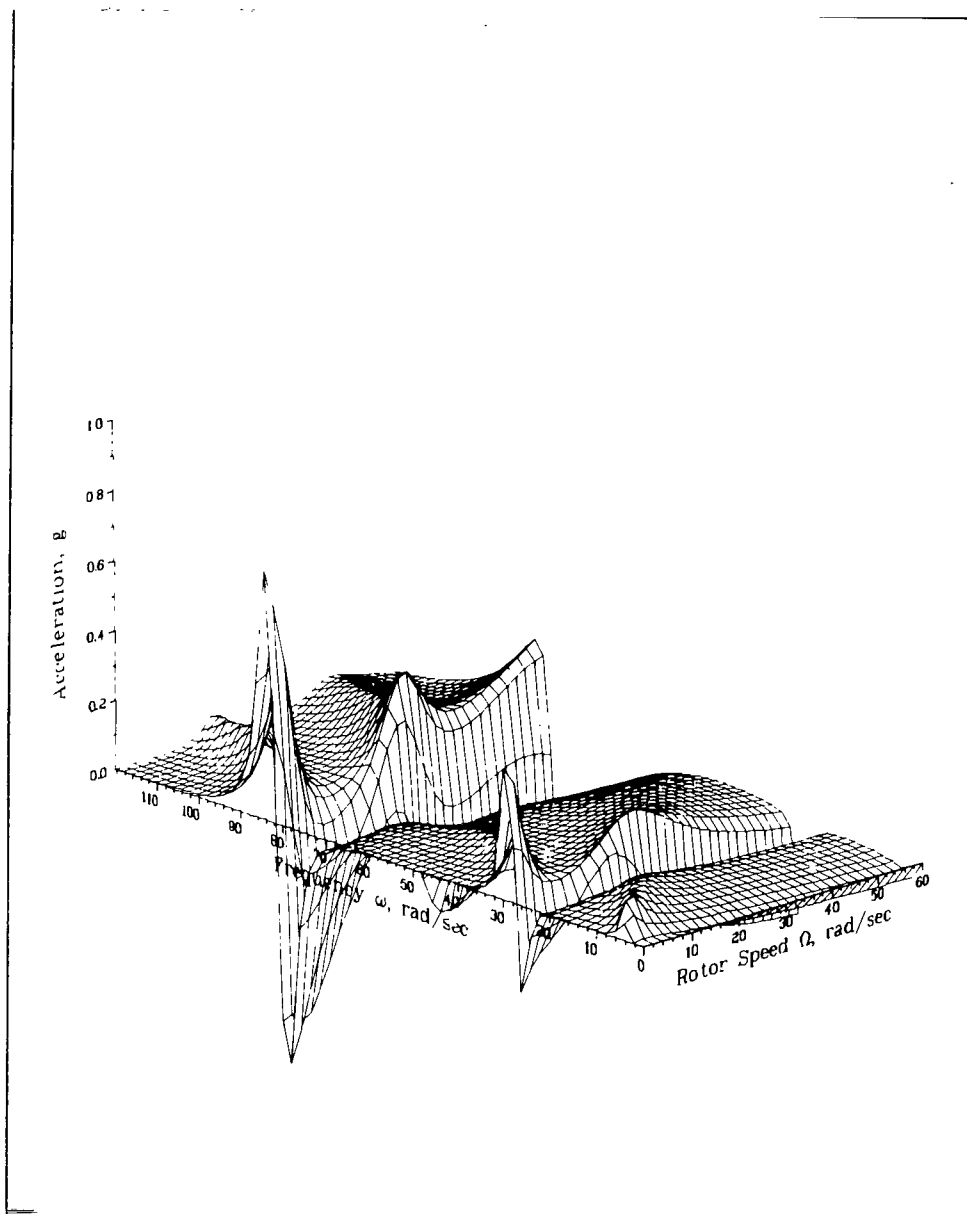
(b) Imaginary component at node 14.

Figure 15.- Continued.



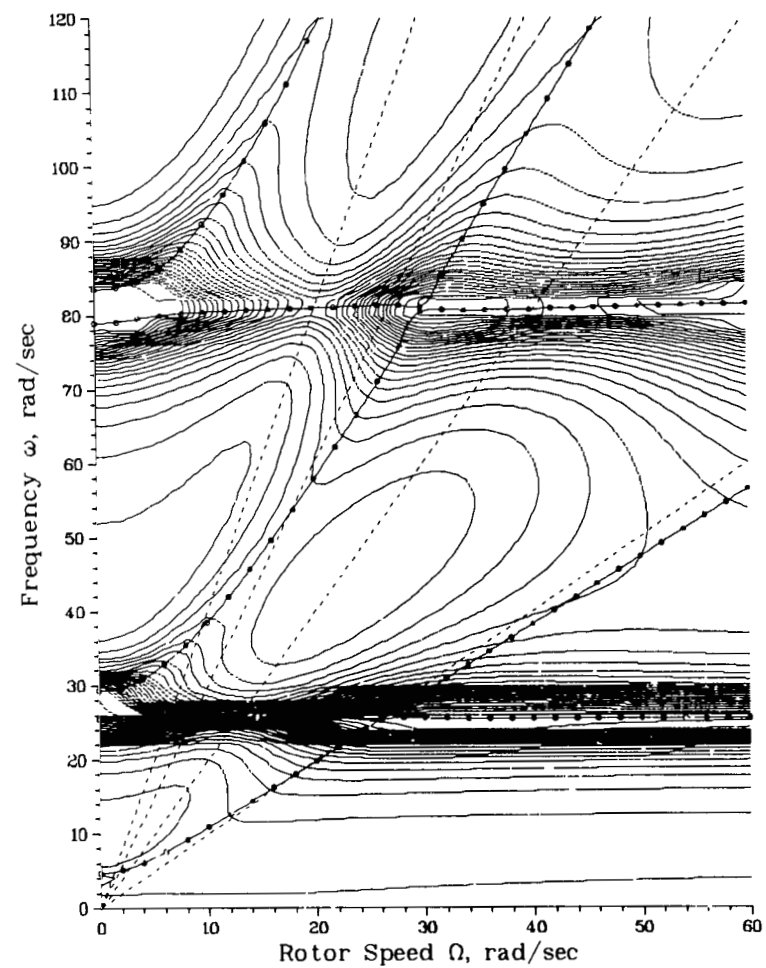
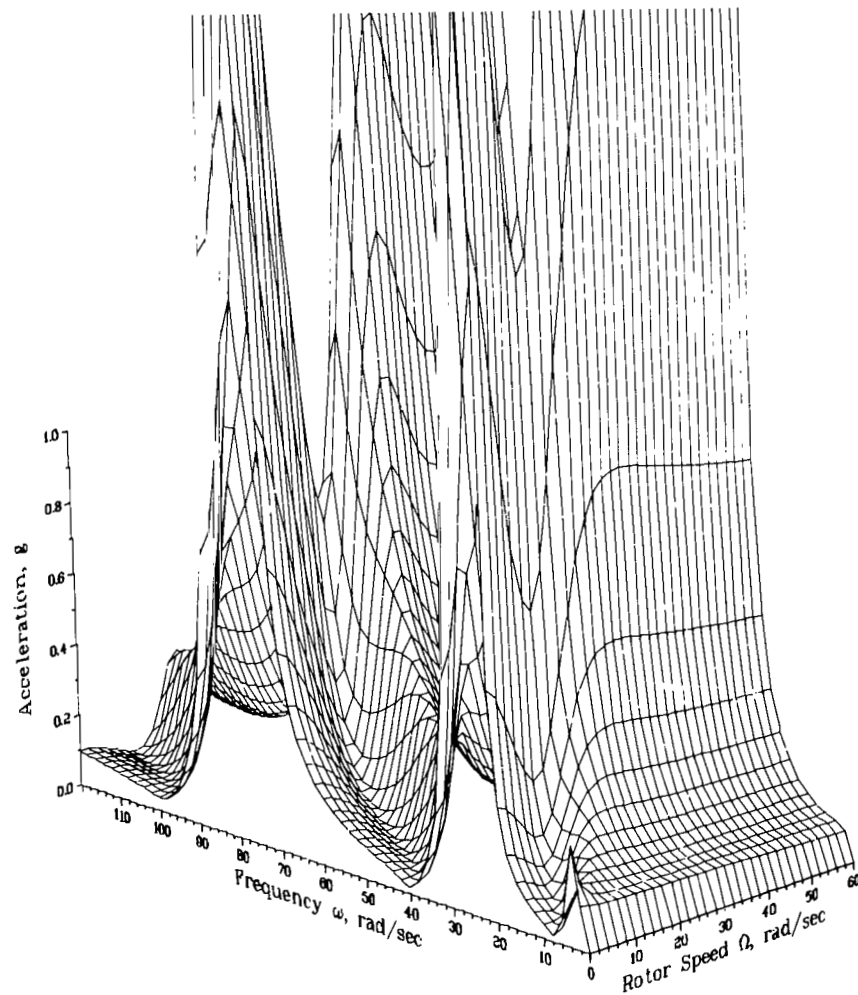
(c) Real component at node 17.

Figure 15.- Continued.



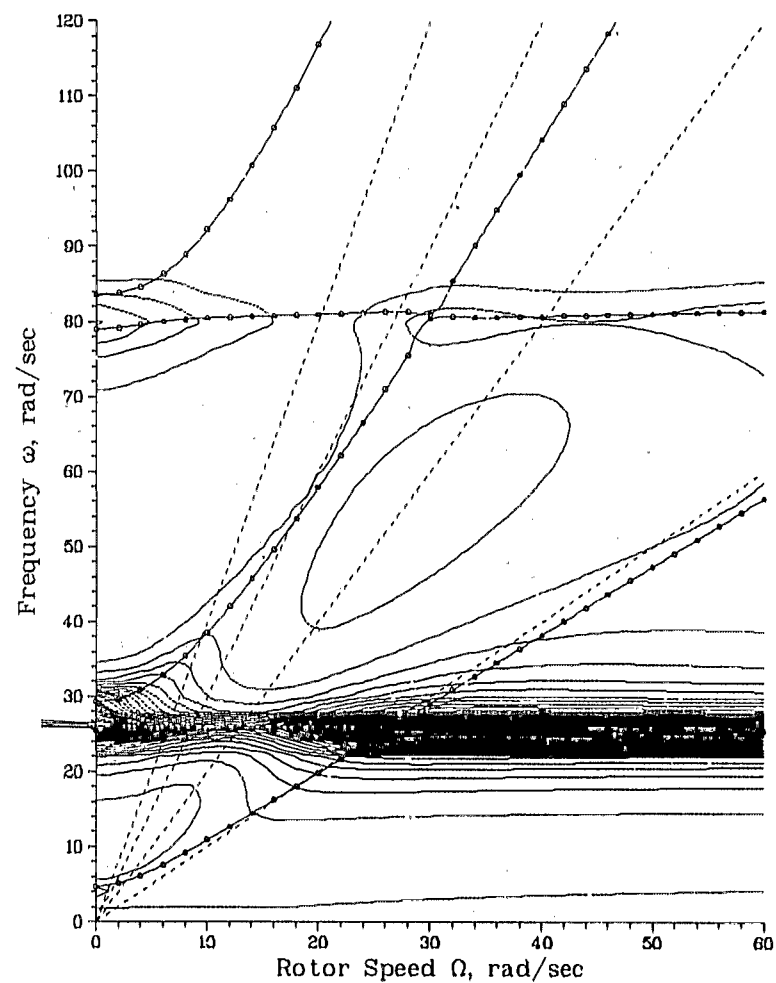
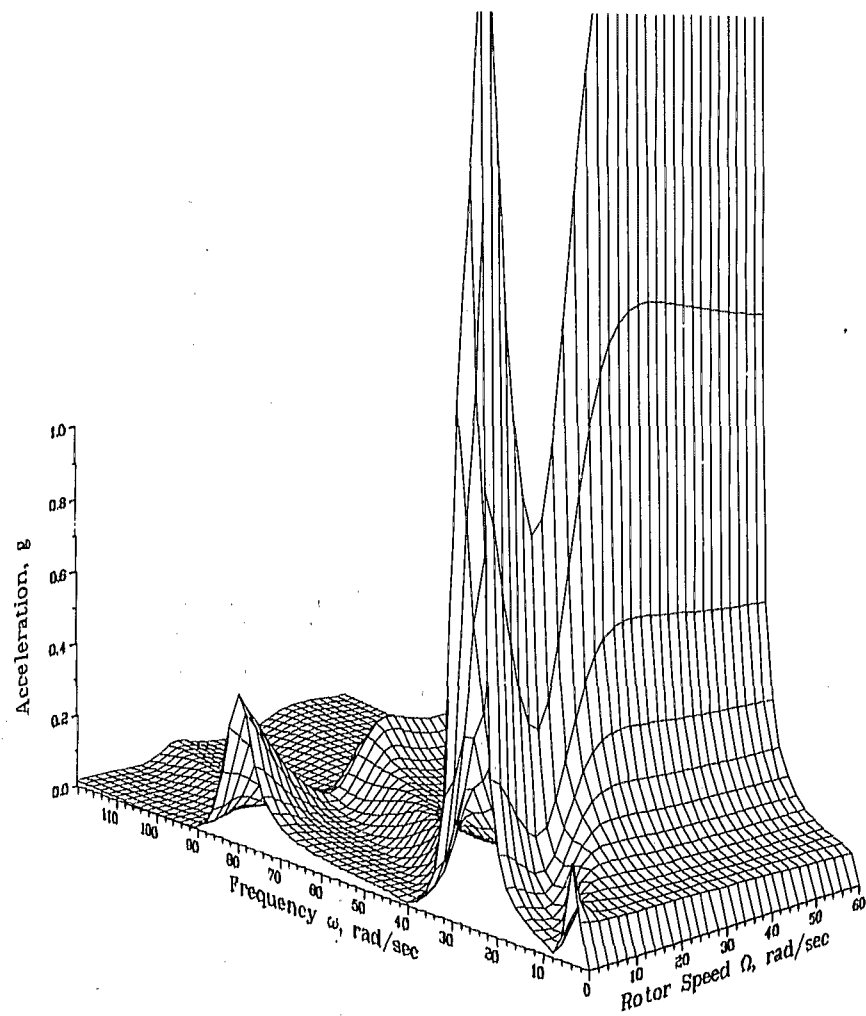
(d) Imaginary component at node 17.

Figure 15.- Concluded.



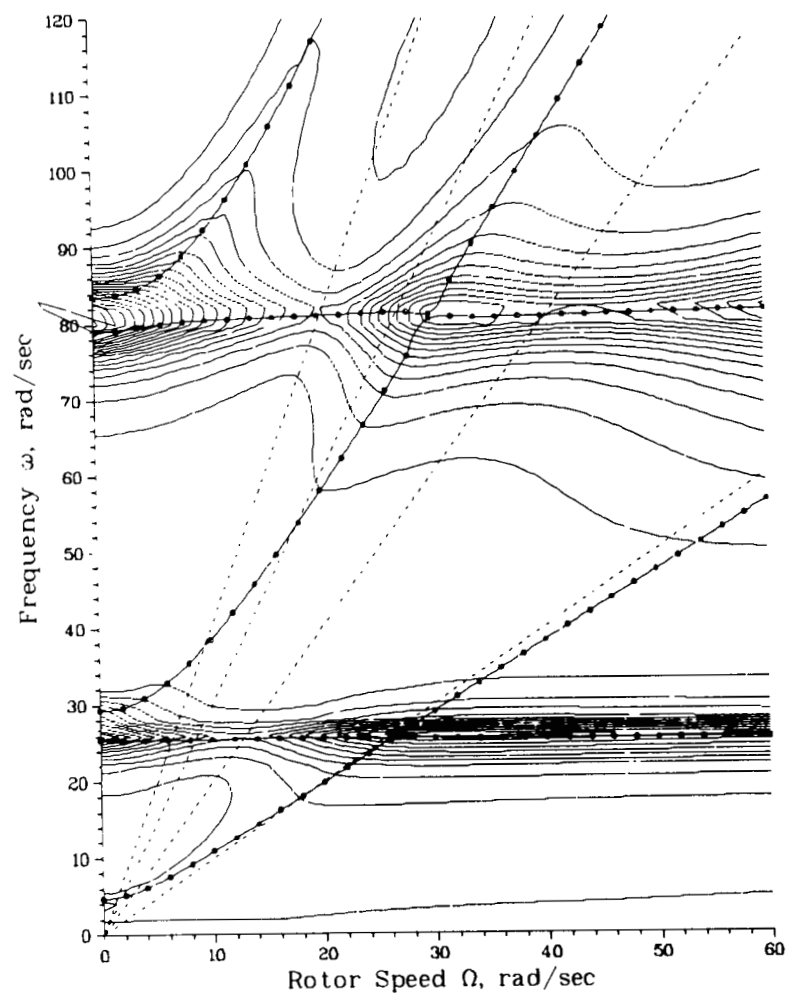
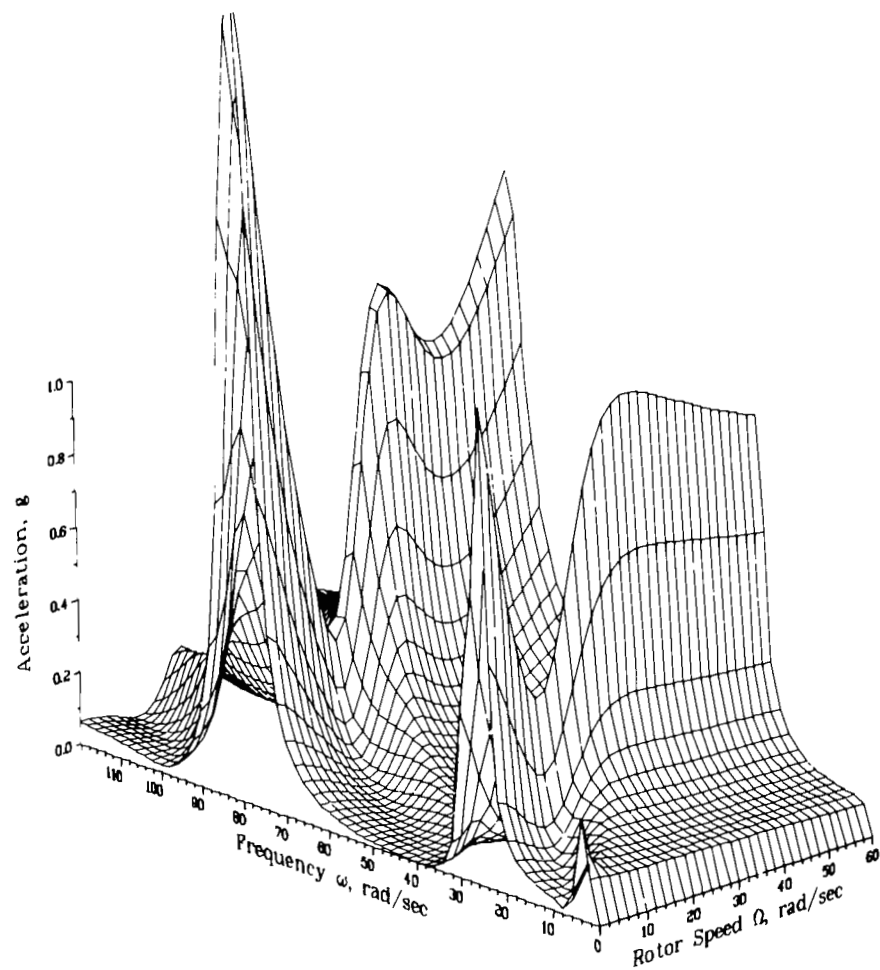
(a) Node 12 response.

Figure 16.- Coupled rotor-fuselage response at various fuselage node points.



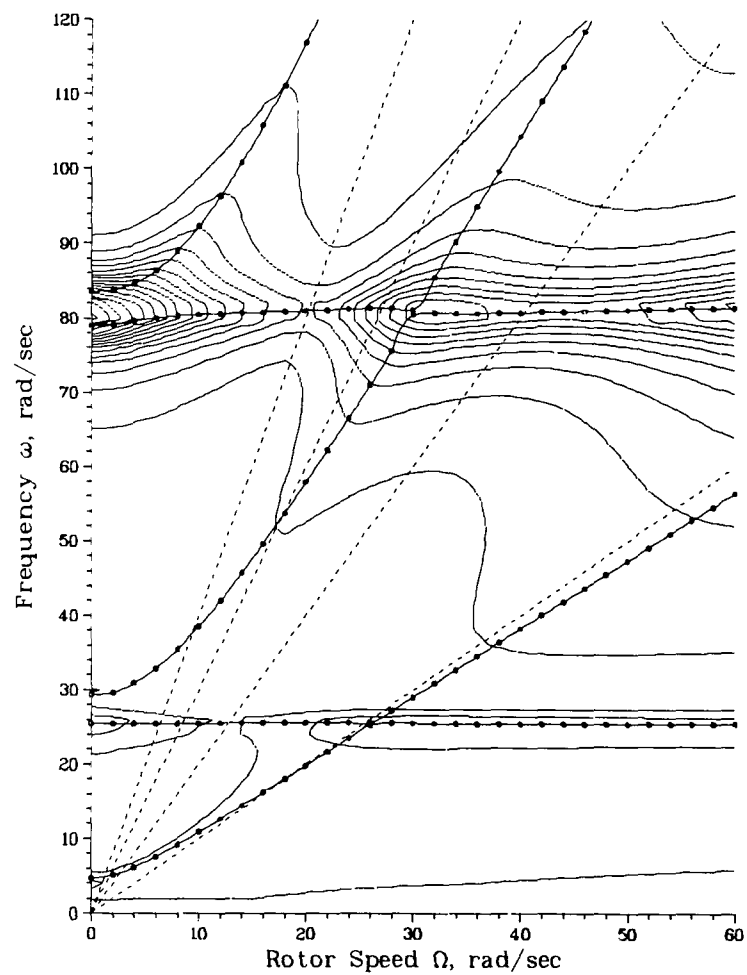
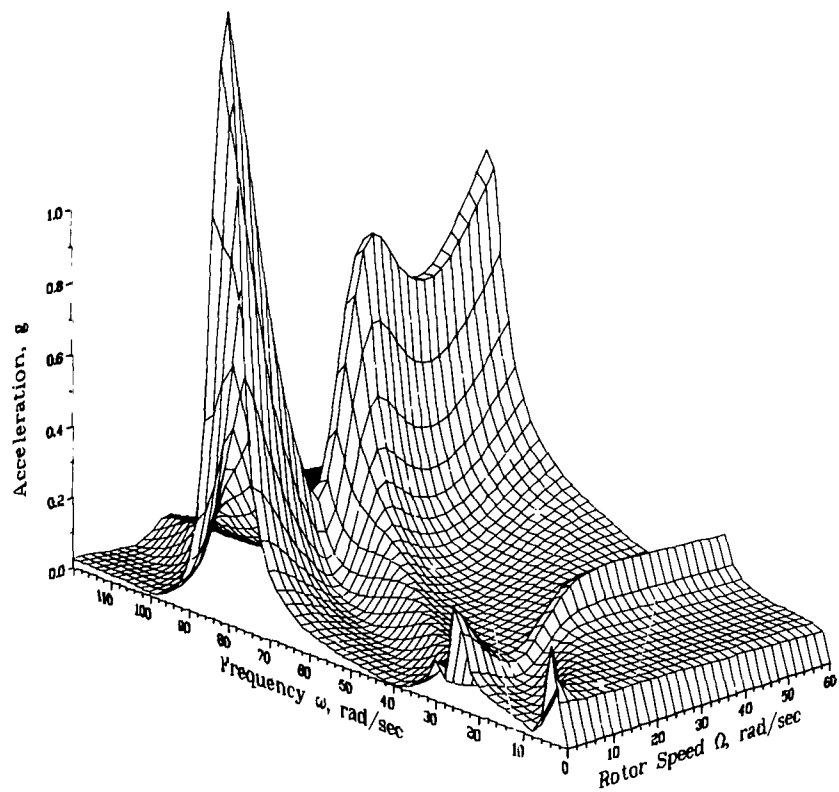
(b) Node 13 response.

Figure 16.- Continued.



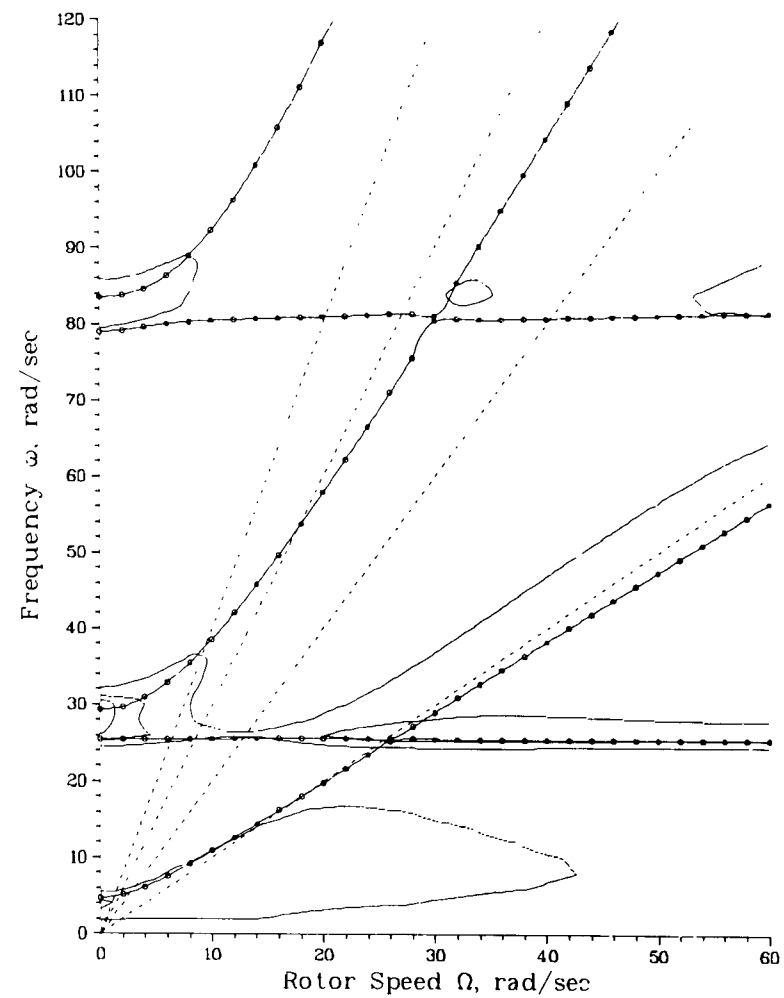
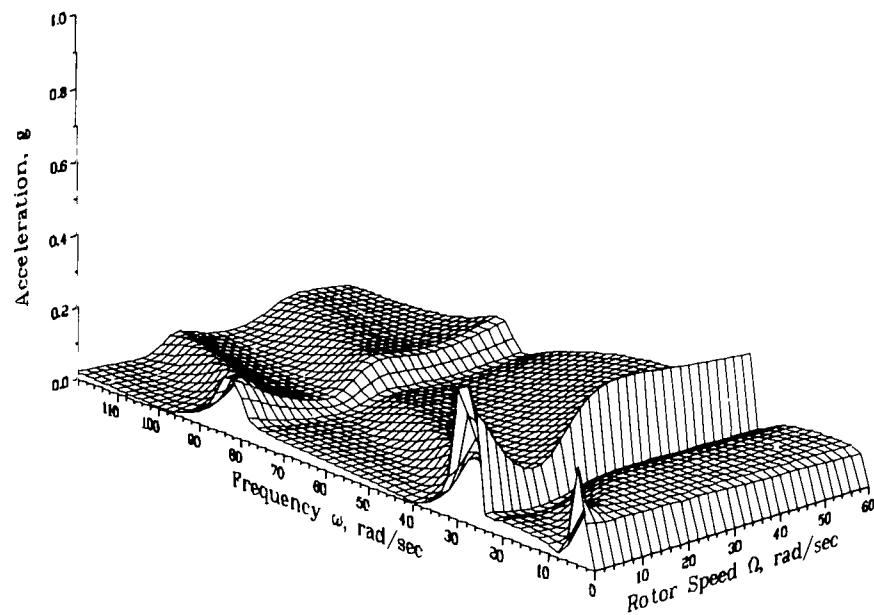
(c) Node 14 response.

Figure 16.- Continued.



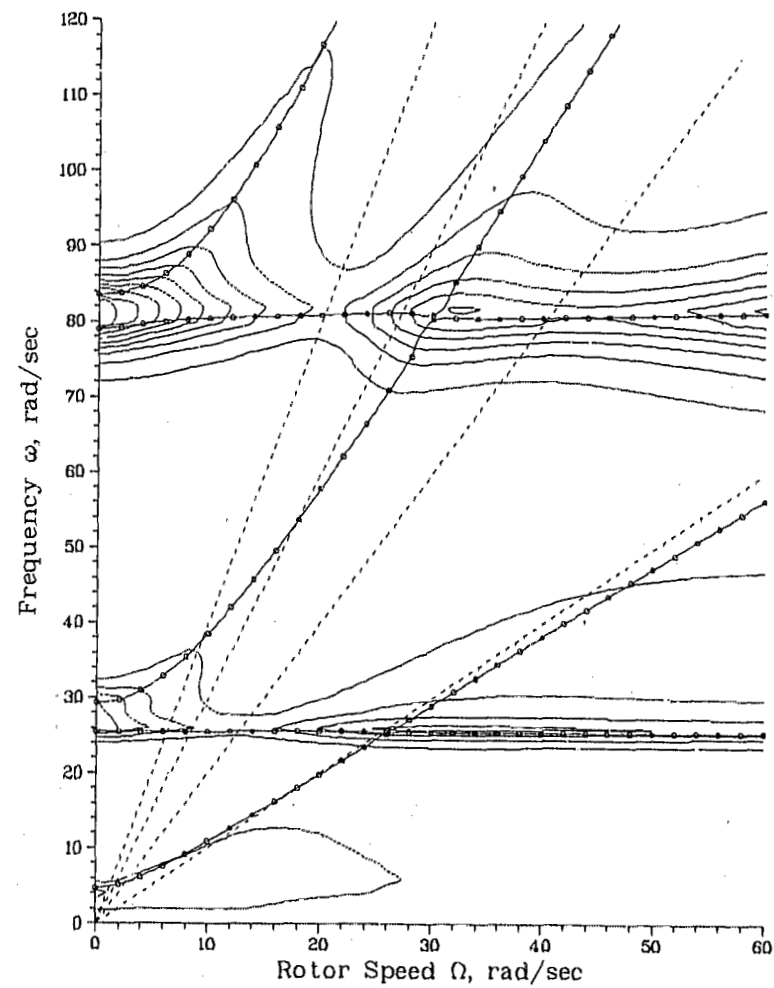
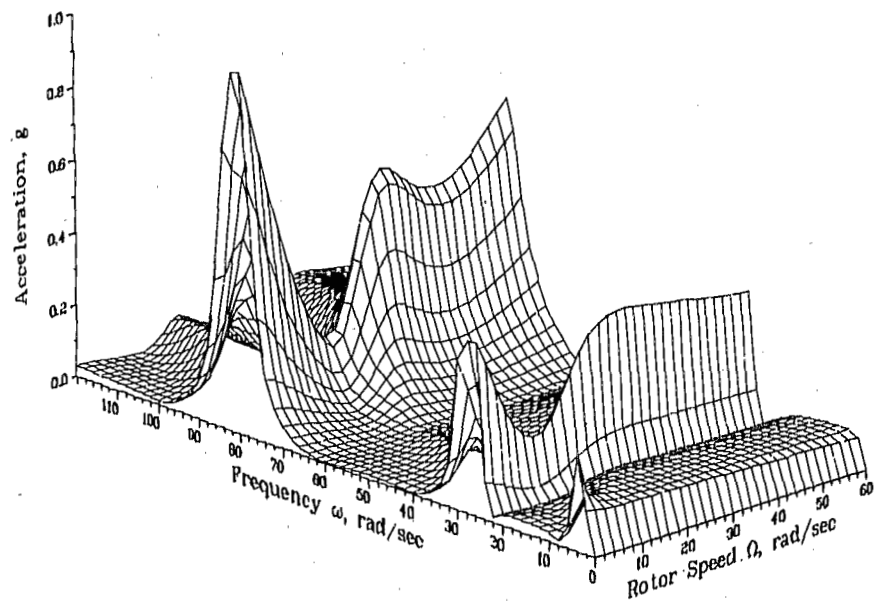
(d) Node 15 response.

Figure 16.- Continued.



(e) Node 16 response.

Figure 16.- Continued.



(f) Node 17 response.

Figure 16.- Concluded.

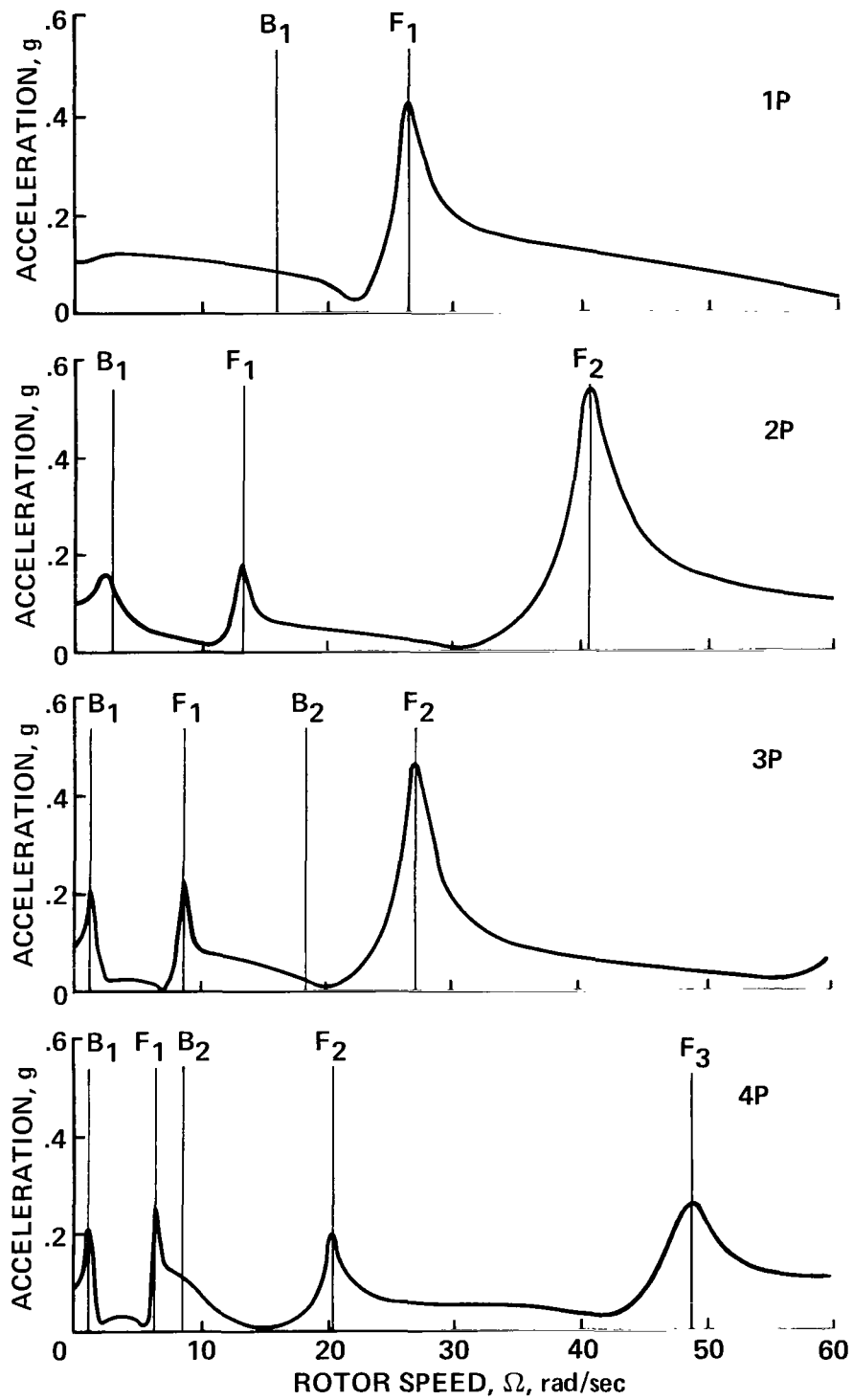


Figure 17.- Coupled rotor-fuselage nP response at node 17.

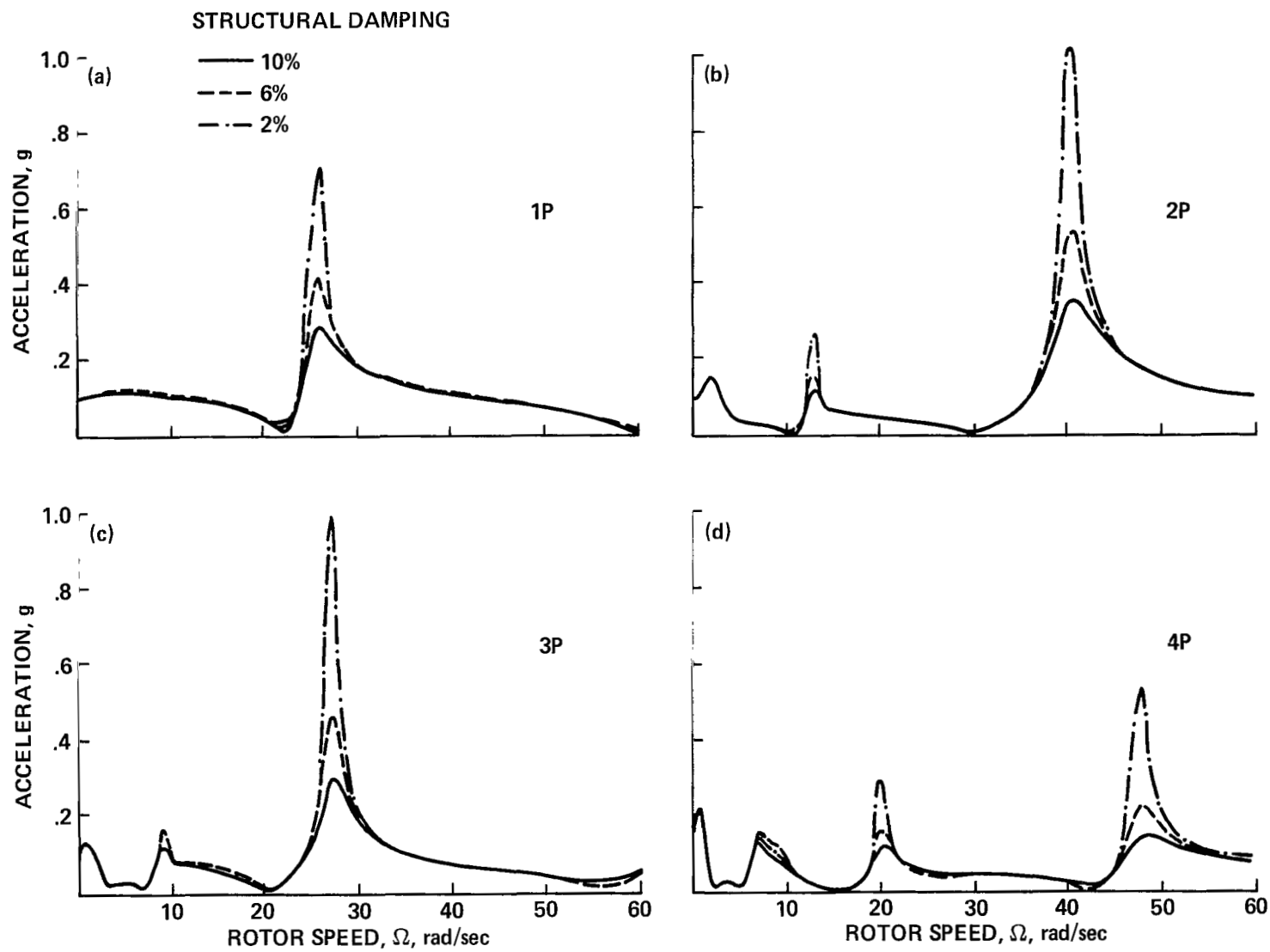
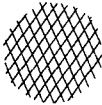




Figure 18.- Effect of structural damping on coupled n^{th} response at node 1/. (a) 1P response; (b) 2P response; (c) 3P response; (d) 4P response.

-  **LOW RESPONSE REGION:**
BETWEEN NATURAL FREQUENCIES OF
COMPANION COMPONENT
-  **HIGH RESPONSE REGION:**
BLADE MODE RESONANCE AT LOW Ω , NOT OF
PRACTICAL IMPORTANCE (EXCEPT AT STARTUP)
-  **VERY HIGH RESPONSE REGION: AT ROTOR-
FUSELAGE MODAL COALESCENCE**

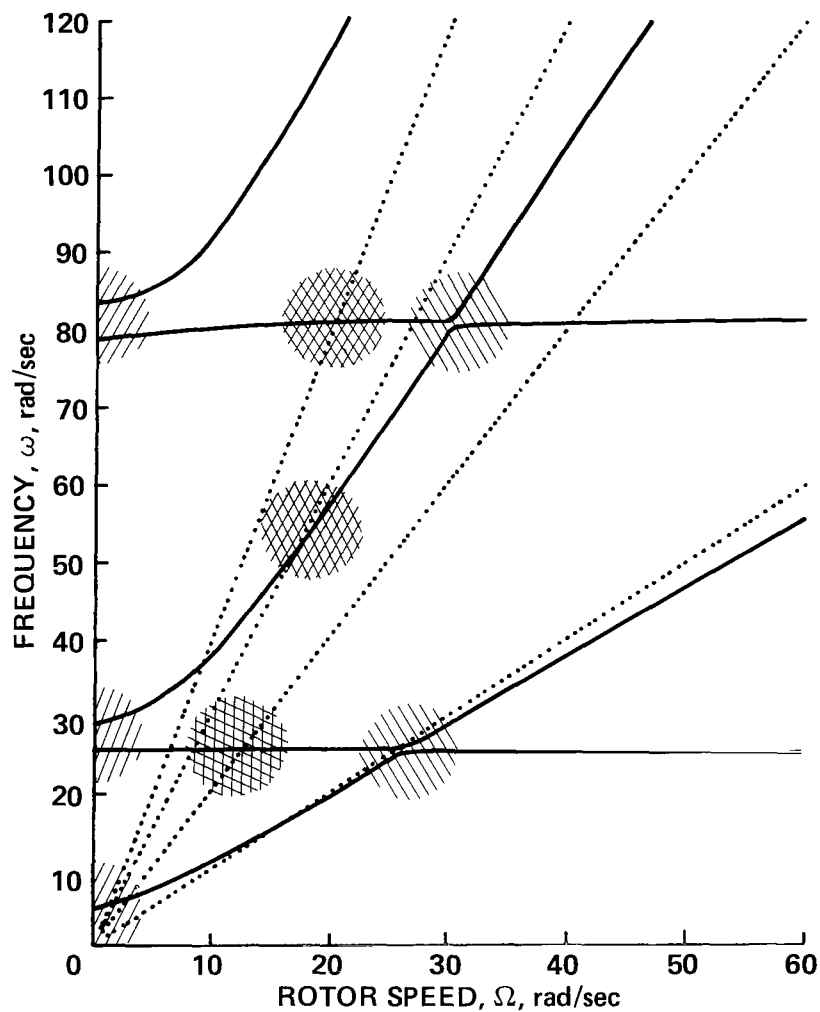


Figure 19.- Qualitative representation of coupled rotor-fuselage response at system natural frequencies at node 17.

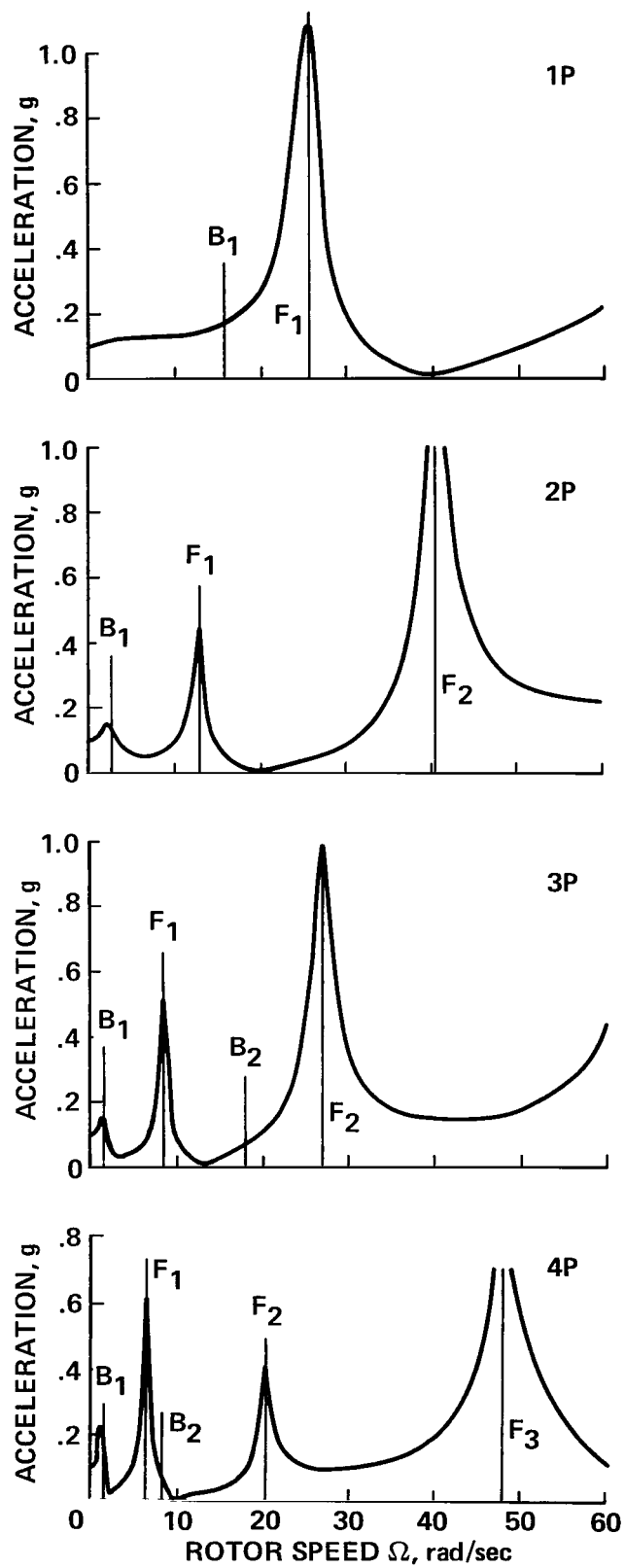
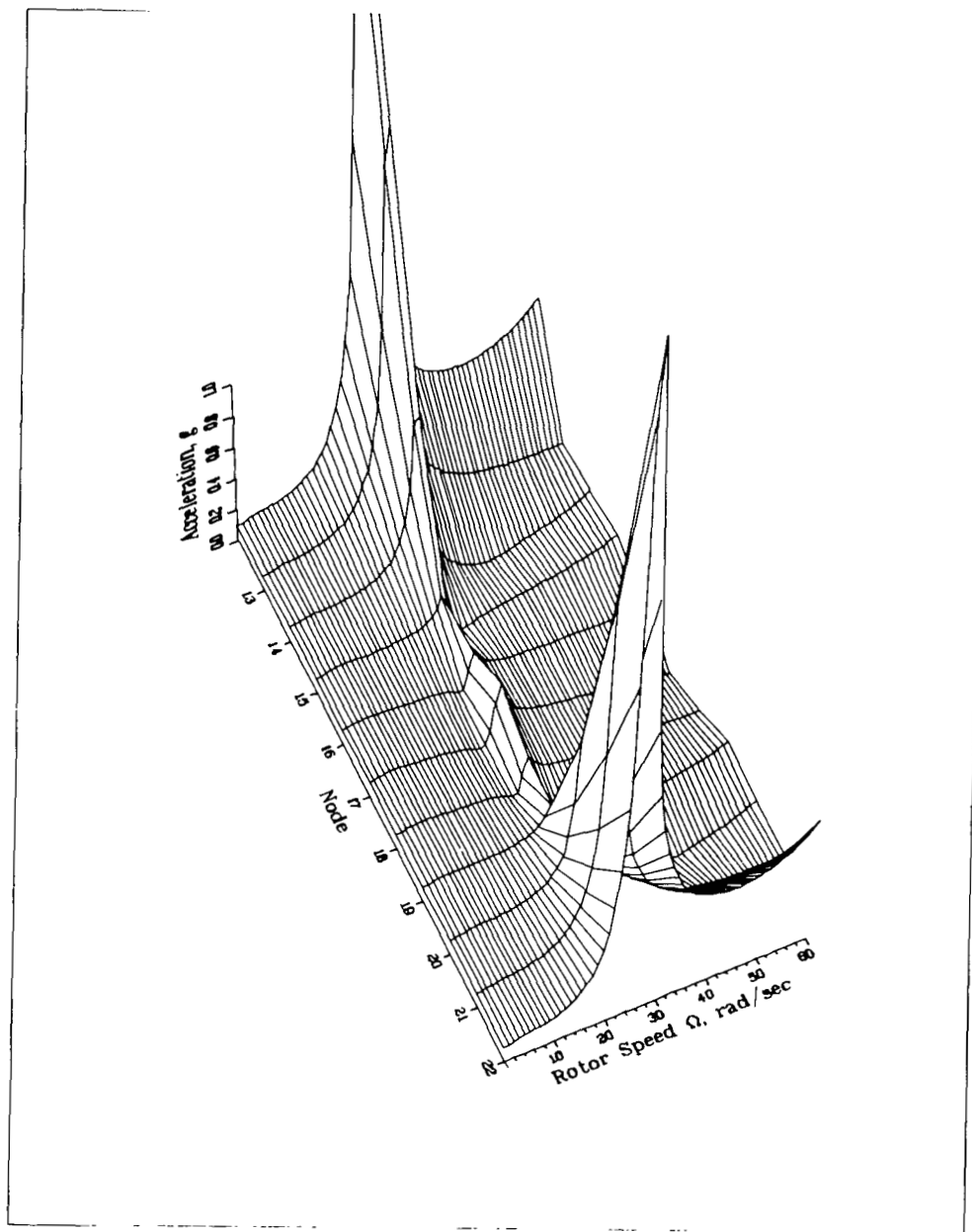
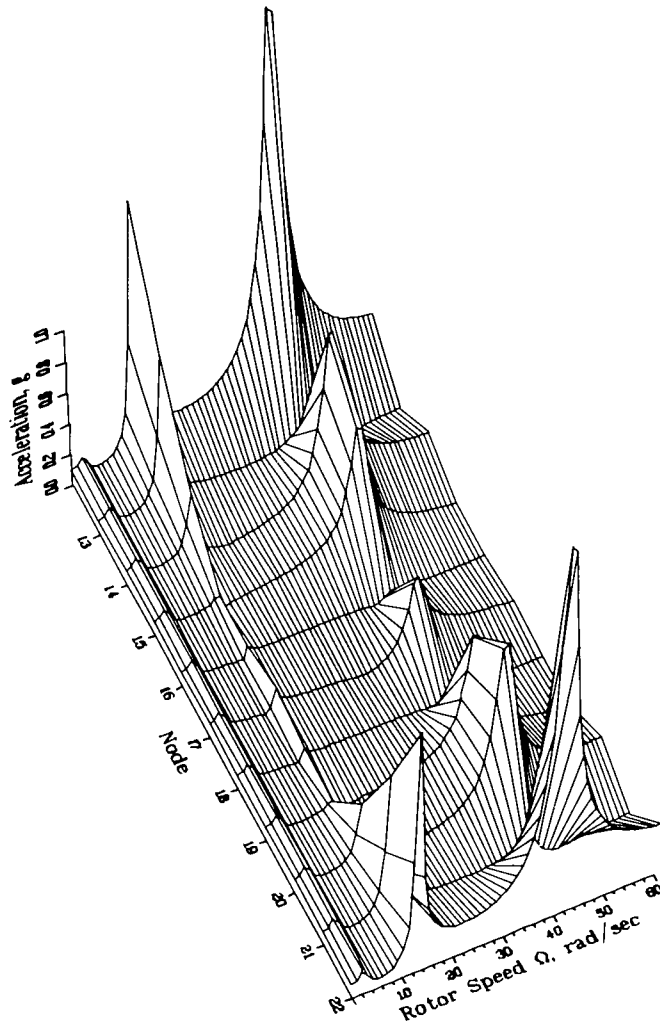


Figure 20.- Coupled rotor-fuselage nP response at node 14.



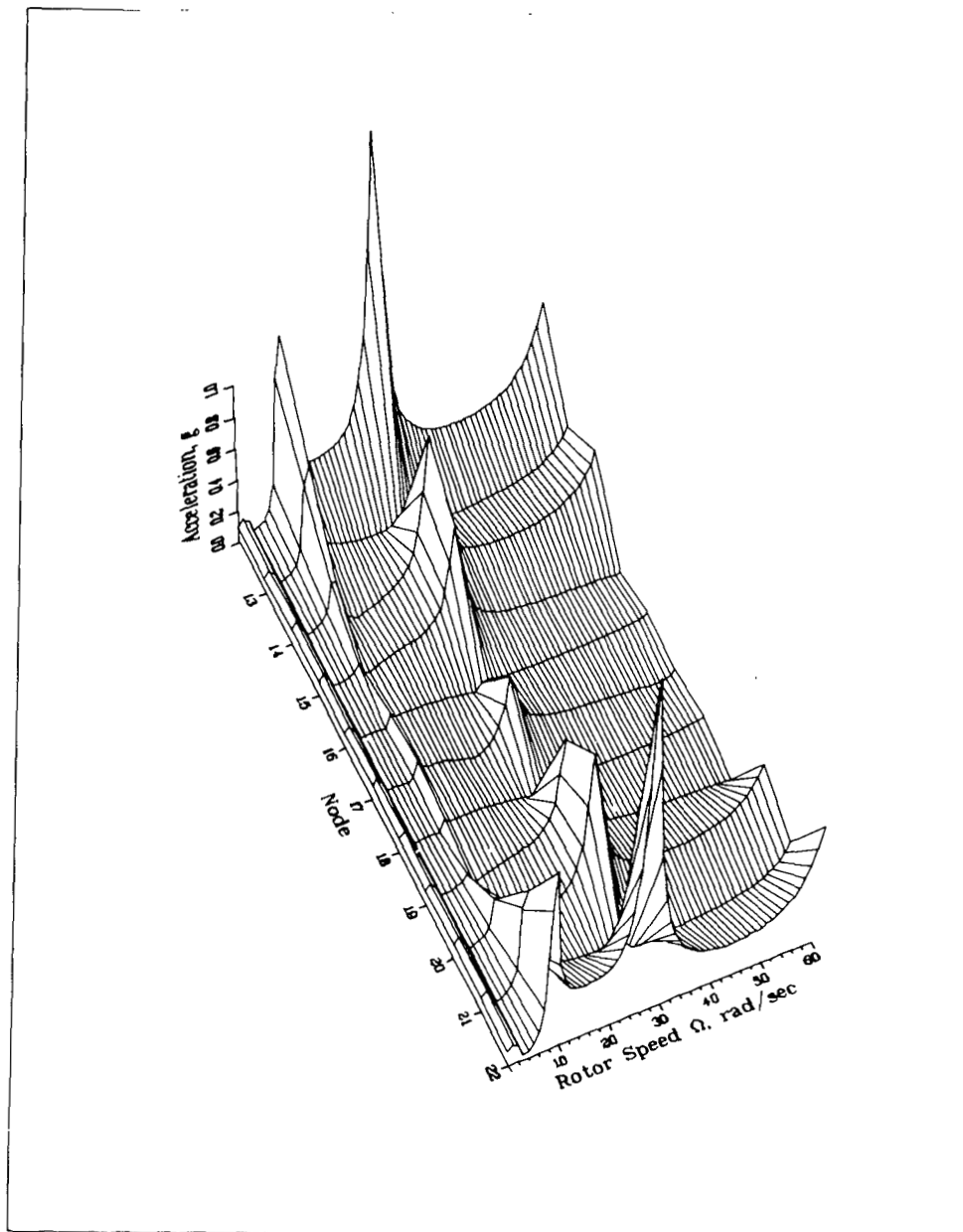
(a) 1P response.

Figure 21.- Variation of coupled rotor-fuselage nP response with fuselage station.



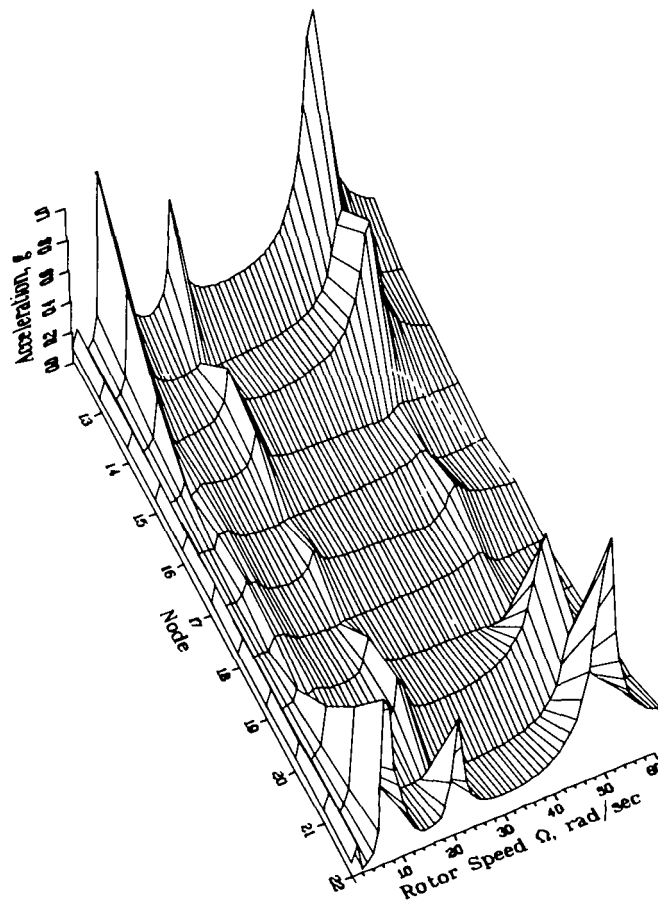
(b) 2P response.

Figure 21.- Continued



(c) 3P response.

Figure 21.- Continued.



(d) 4P response.

Figure 21.- Concluded.

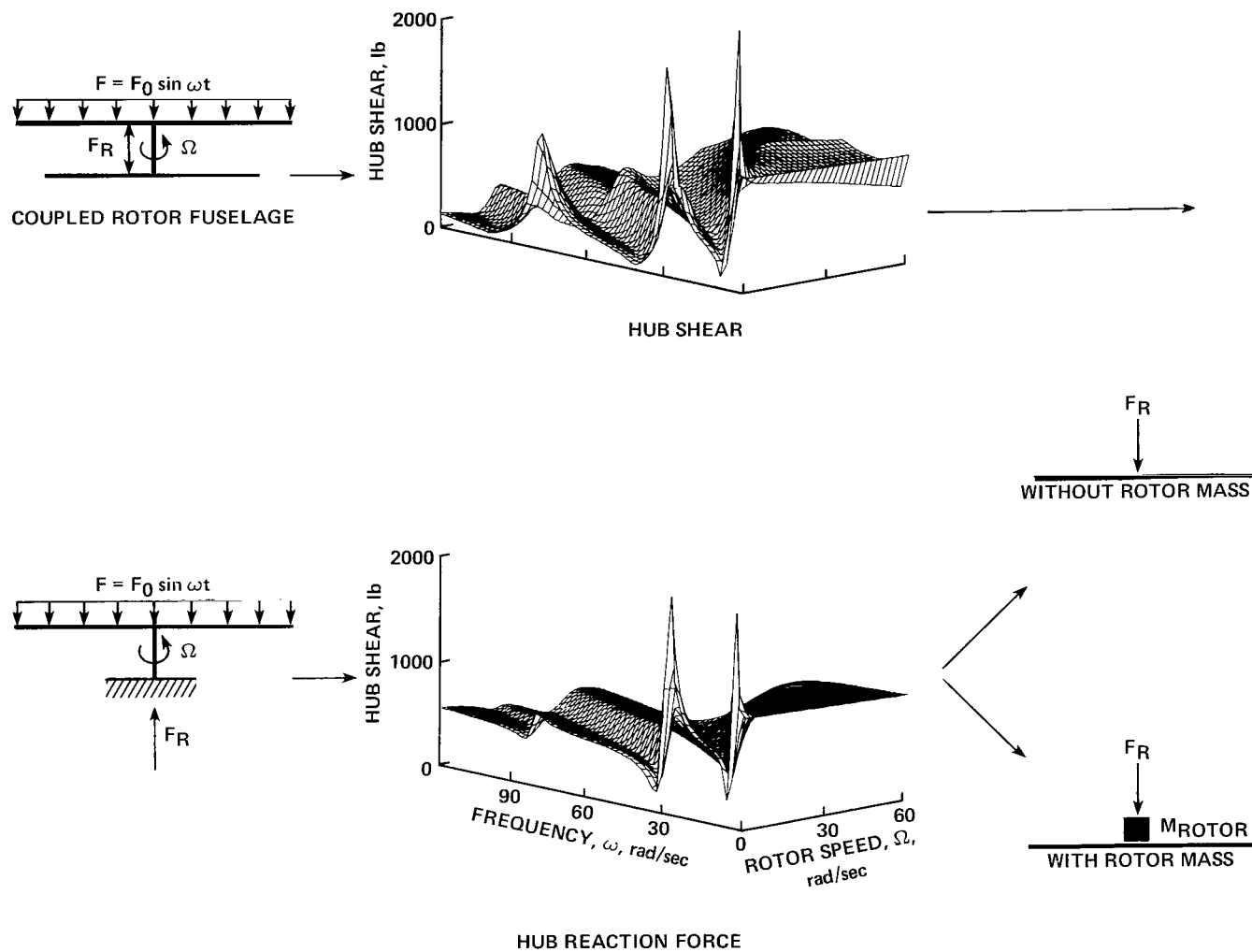


Figure 22.- Exact and approximate response calculations.

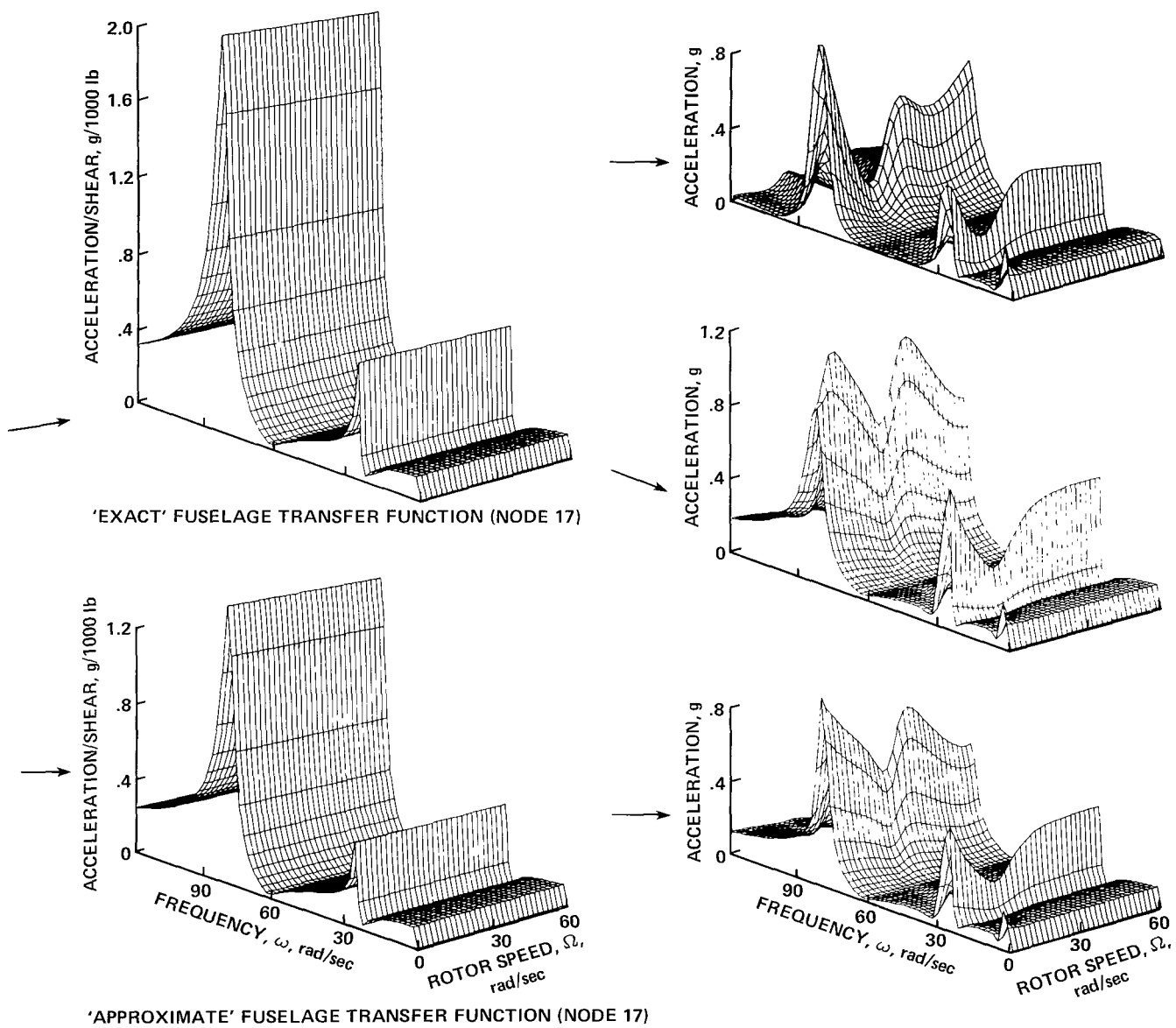


Figure 22.- Concluded.

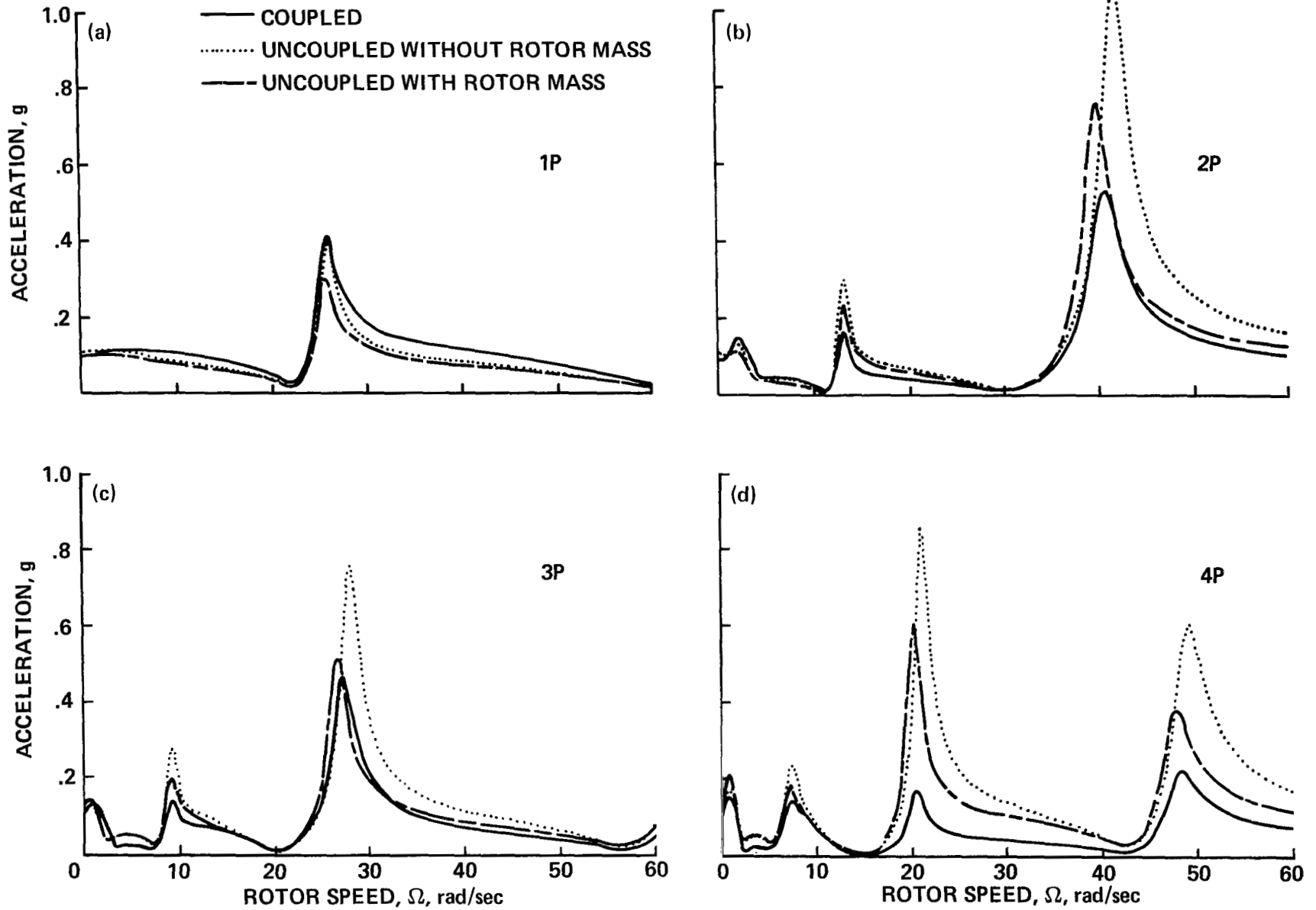


Figure 23.- Comparison of coupled and uncoupled nP response at node 17. (a) 1P response; (b) 2P response; (c) 3P response; (d) 4P response.

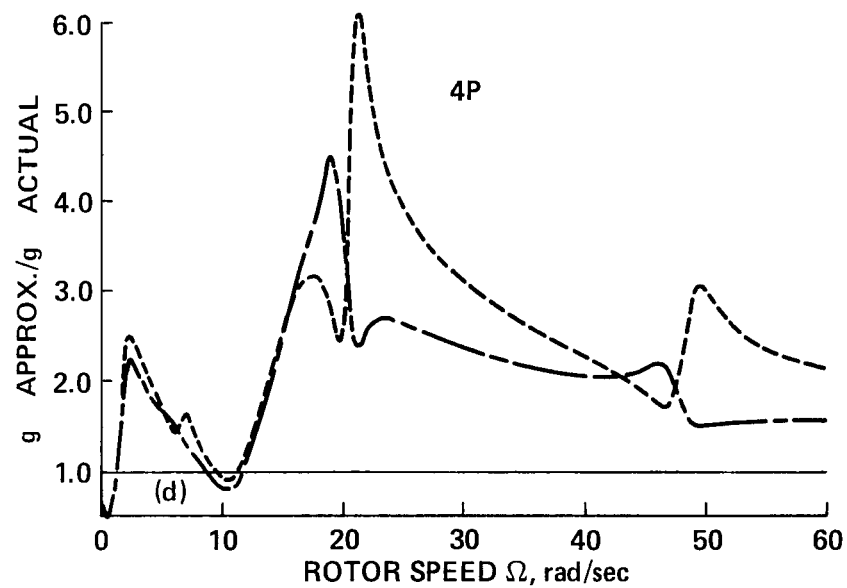
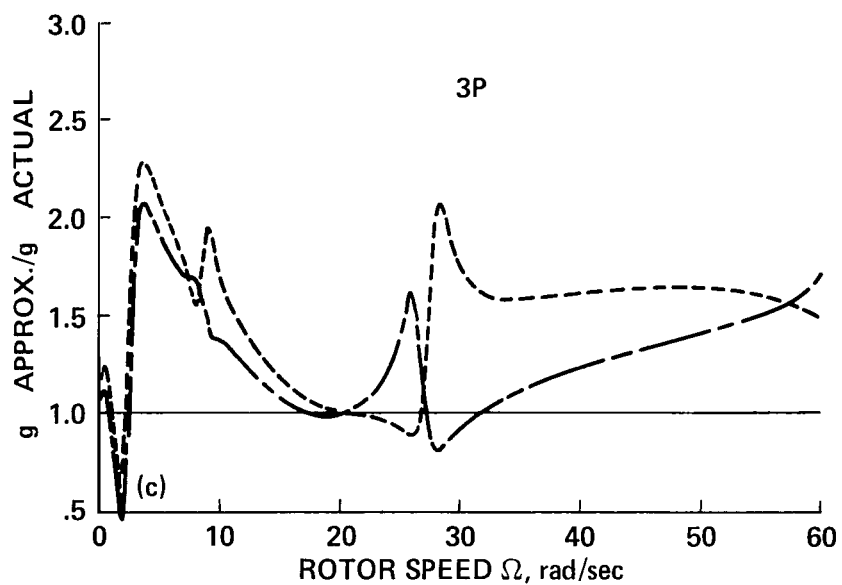
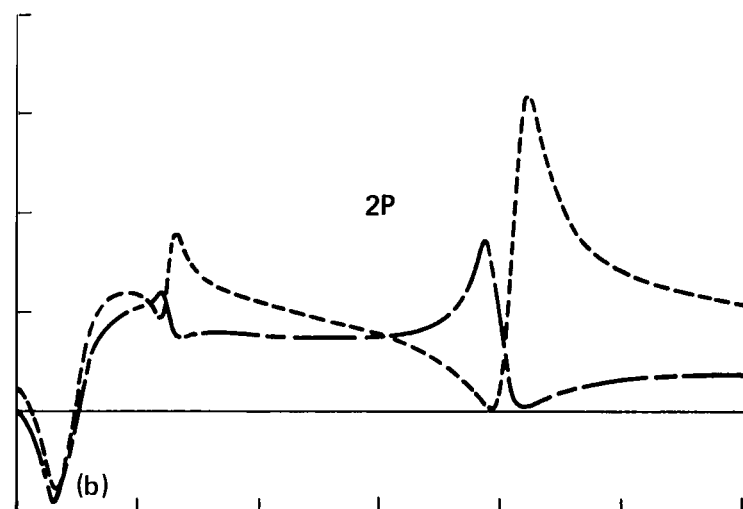
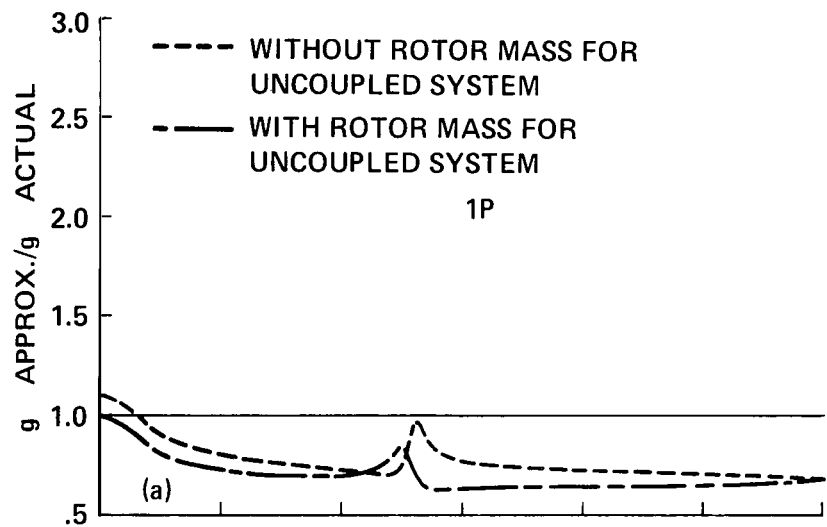


Figure 24.- Ratio of approximate, uncoupled nP response to exact coupled nP response.
 (a) 1P response; (b) 2P response; (c) 3P response; (d) 4P response.

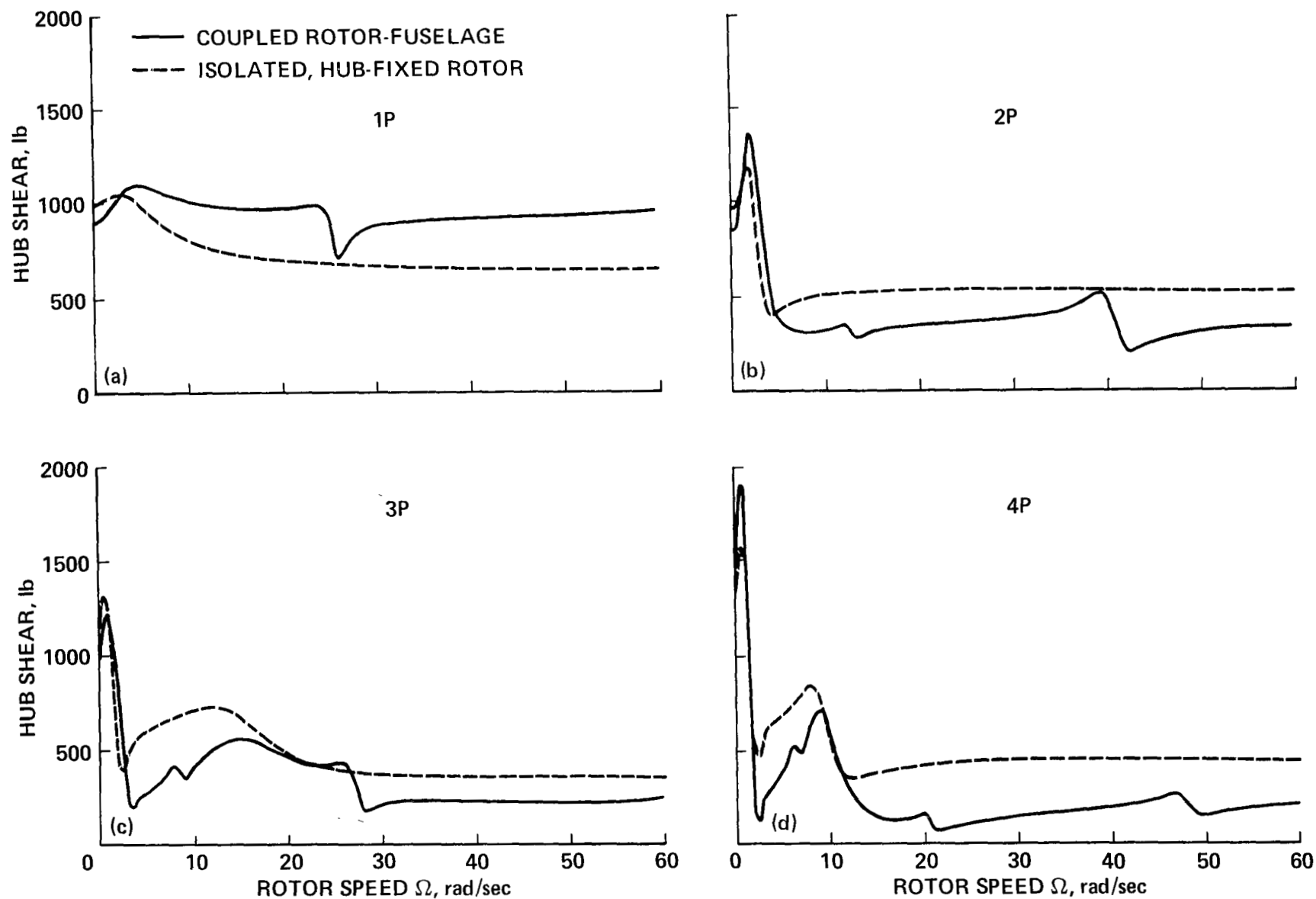


Figure 25.- Comparison of coupled rotor-fuselage nP hub shear and isolated, hub-fixed rotor nP hub reaction force. (a) 1P hub shear; (b) 2P hub shear; (c) 3P hub shear; (d) 4P hub shear.

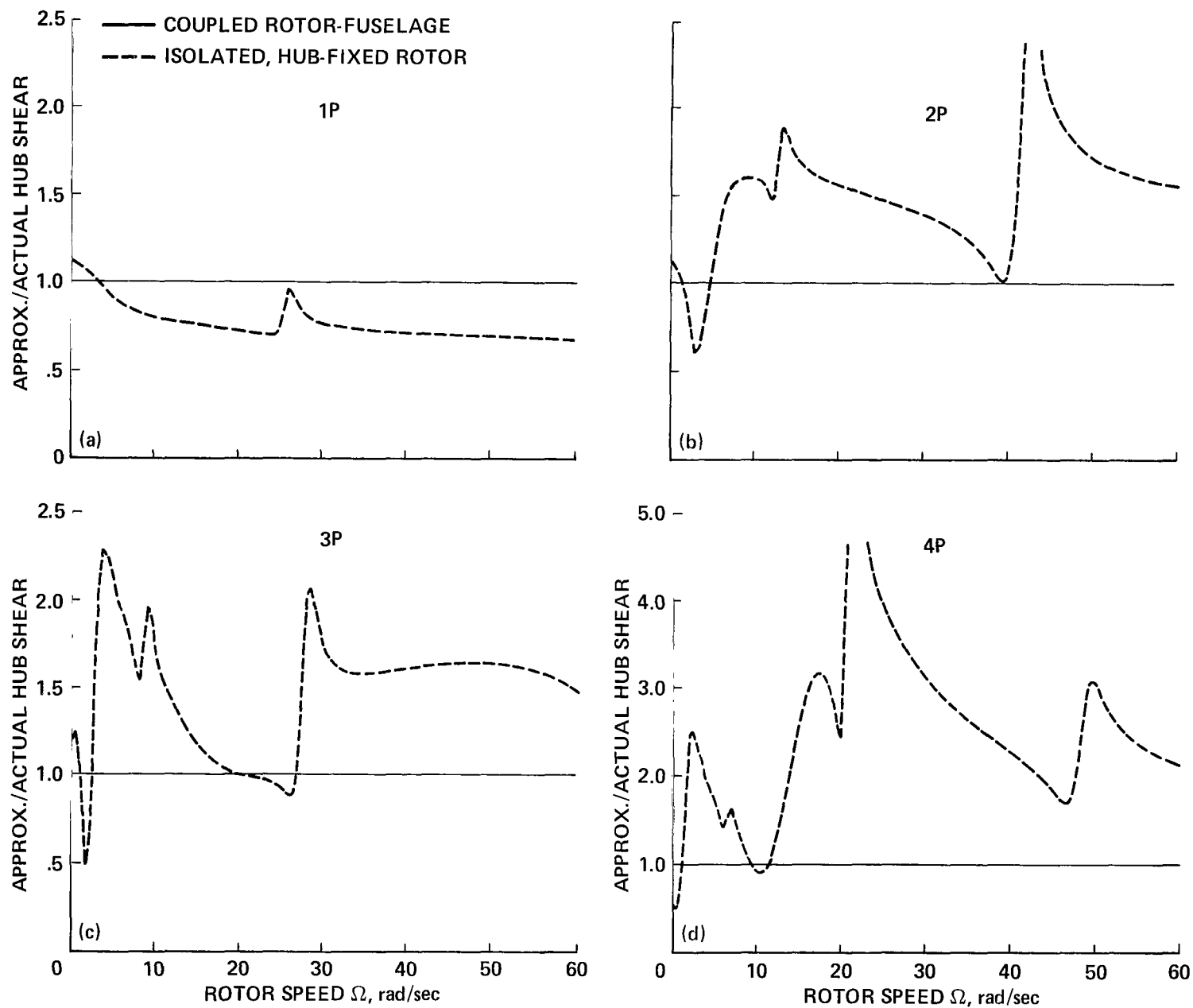


Figure 26.- Ratio of isolated, hub-fixed nP hub reaction force to coupled rotor-fuselage nP hub shear.
 (a) 1P hub shear; (b) 2P hub shear; (c) 3P hub shear; (d) 4P hub shear.

1. Report No. NASA TP-2118 AVRADCOM TR 82-A-15	2. Government Accession No.	3. Recipient's Catalog No.
4. Title and Subtitle THE VIBRATION CHARACTERISTICS OF A COUPLED HELICOPTER ROTOR-FUSELAGE BY A FINITE ELEMENT ANALYSIS	5. Report Date January 1983	6. Performing Organization Code
	8. Performing Organization Report No. A-9053	10. Work Unit No. K-1585
7. Author(s) Michael J. Rutkowski	11. Contract or Grant No.	13. Type of Report and Period Covered Technical Paper
9. Performing Organization Name and Address NASA Ames Research Center and AVRADCOM Research and Technology Laboratories Moffett Field, Calif. 94035	14. Sponsoring Agency Code 909-21-01	
12. Sponsoring Agency Name and Address National Aeronautics and Space Administration, Washington, D.C. 20546 and U.S. Army Aviation Research and Development Command, St. Louis, Mo. 63166		
15. Supplementary Notes Point of Contact: Michael Rutkowski, Ames Research Center, Mail Stop 215-1, Moffett Field, Calif. 94035 (415)965-5891 or FTS 448-5891.		
16. Abstract The dynamic coupling between the rotor system and the fuselage of a simplified helicopter model in hover is analytically investigated. Mass, aerodynamic damping, and elastic and centrifugal stiffness matrices are presented for the analytical model; the model is based on a beam finite element, with polynomial mass and stiffness distributions for both the rotor and fuselage representations. For this analytical model, only symmetric fuselage and collective blade degrees of freedom are treated. Real and complex eigenanalyses are carried out to obtain coupled rotor-fuselage natural modes and frequencies as a function of rotor speed. Vibration response results are obtained for the coupled system subjected to a radially uniform, harmonic blade loading. The coupled response results are compared with response results from an uncoupled analysis in which hub loads for an isolated rotor system subjected to the same sinusoidal blade loading as the coupled system are applied to a free-free fuselage. It is shown that although the fuselage response as a function of forcing frequency and rotor speed is similar in the two cases, the responses resulting from the approximate, uncoupled analysis are significantly greater than those resulting from the coupled analysis. Thus, it is necessary to carry out a coupled rotor-fuselage analysis in order to accurately predict the fuselage vibration response.		
17. Key Words (Suggested by Author(s)) Dynamic structural analysis Finite element method Helicopter design Rotary wing aircraft Structural vibration	18. Distribution Statement Unclassified - Unlimited Subject Category: 05	
19. Security Classif. (of this report) Unclassified	20. Security Classif. (of this page) Unclassified	21. No. of Pages 77
		22. Price* A05

*For sale by the National Technical Information Service, Springfield, Virginia 22161

National Aeronautics and
Space Administration

Washington, D.C.
20546

Official Business

Penalty for Private Use \$300

THIRD-CLASS BULK RATE

Postage and Fees Paid
National Aeronautics and
Space Administration
NASA-451



DEPT OF THE AIR FORCE
AF WEAPONS LABORATORY
ATTN: TECHNICAL LIBRARY (SUL)
KIRTLAND AFB NM 87117
830125 500903DS

S

NASA

POSTMASTER: If Undeliverable (Section 158
Postal Manual) Do Not Return